Università degli studi di Padova

Dipartimento di Fisica e Astronomia

Corso di Laurea Magistrale in Astronomia

NGC 300 2008OT-1:

Stellar Outburst or Electron Capture Supernova?

Relatrice:
Prof. Paola Marigo

Correlatore:
Dott. Andrea Pastorello

Laureando:
Giorgio Valerin

Abstract

Supernova explosions are among the most energetic and intriguing phenomena in the universe, reaching high luminosities (M $\sim$ -17) and leading towards the complete disruption of the star or to the formation of a compact remnant. On the other hand, classical novae are non terminal and possibly recurrent events which are far less bright (M $\sim$ -8). In the last two decades there have been several observations of transient showing luminosities between the supernovae and the classical novae. The nature of these "Gap Transients" appears to be heterogeneous both in the features observed and in their origin (Pastorello & Fraser 2019). Some of them mimic the explosion of a supernova without being terminal events, like the Luminous Blue Variables (Pastorello et al. 2010a), earning therefore the name of "supernova impostors". Other intermediate luminosity transients, however, may be genuine faint supernovae (Botticella et al. 2009), perhaps originating from an intermediate mass progenitor (between 8 $M_{\odot}$ and 12 $M_{\odot}$). Investigating such events may shed light on the fate of Super AGB stars, setting constraints on late stellar evolution in this peculiar range of masses. This thesis focuses on NGC300OT: thanks to its proximity (d $\sim$ 2 Mpc) this object has been studied extensively and it can be used as a template for recognizing similar transients. New photometry and spectra will be compared with data published in literature, and we discuss whether these are compatible with a non terminal eruption or with a faint supernova event.

Contents

1 Introduction

Supernovae (SNe) are the evolutionary endpoint of massive stars and more moderate mass stars in binary systems. SNe may compete in luminosity with their host galaxy, as they release $E_{rad} \sim 10^{49}$ erg as radiation and eject matter at a significant fraction of the speed of light. On the other hand, classical novae (CNe) are fainter stellar outburst caused by the accretion of matter on a white dwarf, radiating at most $\sim 10^{45}$ erg. Supernovae and classical novae are separated by a luminosity gap at peak of roughly 5 magnitudes, with the brightest novae reaching $M_V \sim$ -10 mag and the faintest core collapse supernovae having $M_V \sim$ -15 mag. During the last two decades, however, serendipitous discoveries and in-depth archival searches of weak transients have begun to populate this gap (Figure1) (Kasliwal 2012, Pastorello & Fraser 2019). The recent discovery of new classes of transients does not come as a surprise: development of new instruments as well as dedicated surveys paved the way to a new era for observations of the transient Universe. Early SNe surveys targeted large, nearby galaxies in order to have a higher chance of detecting an event. The Lick Observatory Supernovae Search (LOSS) is a classic example of this kind of study, with 15000 nearby galaxies observed with a limiting magnitude of $\sim$ 19 mag. This led to the discovery of $\sim$ 1000 SNe in over a decade of activity, allowing for crucial SNe rates analysis (Li et al. 2011b). These targeted searches have been quite successful in detecting new SNe, but they have the obvious downside of introducing a host galaxy bias. To overcome the observational bias, wide field telescopes are used to perform blind searches, aiming to cover the whole sky instead of just the target galaxies. Wide field surveys like the Palomar Transient Factory (Law et al. 2009), Pan-STARRS1 (Kaiser et al. 2010) or SkyMapper (Keller et al. 2007) are able to cover up to 6000 square degrees per night, reaching a limiting magnitude of 21 mag with expositions of 60s (Smartt et al. 2015). The ongoing project "All-Sky Automated Survey for Supernovae" (ASAS-SN) (Shappee et al. 2014) exploits 24 small telescopes distributed around the globe to cover the whole extragalactic sky in less than 3 days, to a limiting magnitude of V $\sim$ 17 mag. Spectroscopic and multicolor imaging follow-up is often performed through larger telescopes (Rau et al. 2009, Botticella et al. 2010): a fundamental role in this context is played by the Public European Southern Observatory Spectroscopic Survey of Transient Objects (PESSTO) (Smartt et al. 2015).

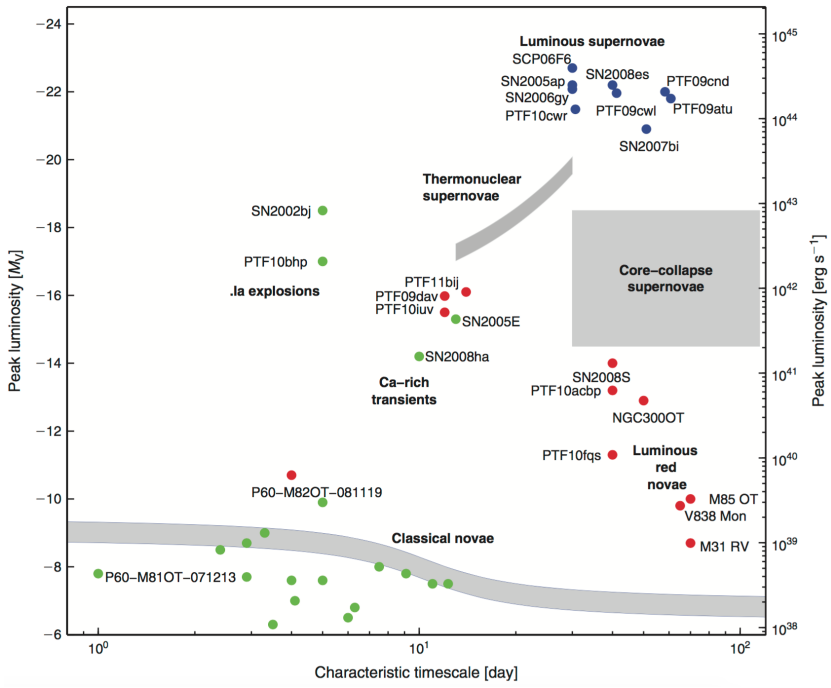

Figure 1: Peak luminosity - Decline timescale diagram. Grey shaded areas show the location of thousands of "standard" objects. After 2005 several transients started filling previously empty regions on the graph. Here the term "Luminous red novae" is associated with NGC300OT and SN2008S, but later studies classify them as Intermediate Luminosity Red Transients. (Figure from Kasliwal 2012).

Another key point for the discovery of new transients is the observational cadence: being able to detect and follow-up objects with short timescales is crucial to populate new regions in the transient phase space, discovering new forms of variability and accurately characterizing the known ones. The Zwicky Transient Facility (ZTF) employs the Palomar Schmidt telescope to survey the observable northern sky with a limiting magnitude of *sim* 19 mag with a cadence ranging from minutes to days (Graham et al. 2019). Thanks to the analysis of differential images, alerts can be produced within 20 minutes after the raw image was taken, allowing for an early study of the transient. Along with ZTF, other surveys such as the "Asteroid Terrestrial-impact Last Alert System" (ATLAS) (Tonry et al. 2018) can contribute to the serendipitous discovery of SNe candidates. In particular, ATLAS monitors the whole sky with a cadence of two days, leading to the discovery of 311 spectroscopically classified transient objects between January 2016 and March 2018, even more than the 307 discovered by ASAS-SN during the same

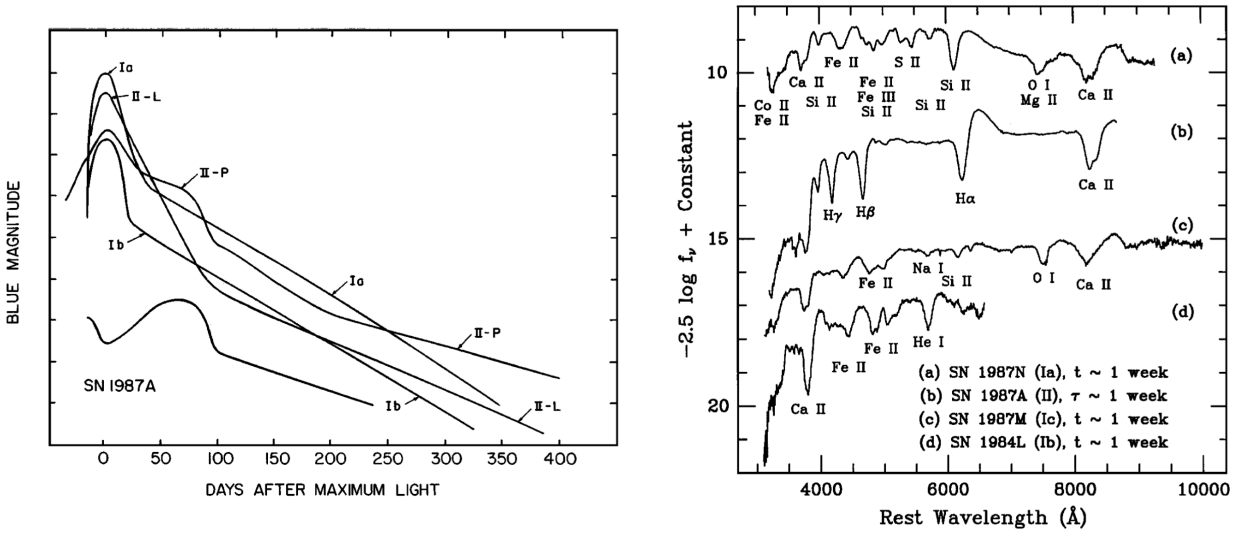

Figure 2: On the left, schematic light curves for SNIa, SNII-P, SNII-L and SNIb. The light curve for SNIb is averaged to include SNIc as well. The light curve of SN 1987A is showed as a comparison, since it is the most studied supernova event thanks to its proximity. In the right panel are shown early optical spectra for 4 standard supernovae events, each displaying characteristic features (Figure from Filippenko 1997).

time. Last but not least, thanks to telescopes like Swift and Spitzer, follow-up observations can be performed in domains outside the optical spectrum: X-ray and mid-infrared images can give insight on different processes, such as interaction between ejecta and circumstellar medium or dust formation (Rivera Sandoval et al. 2018, Szalai et al. 2019). All these improvements naturally led to the discovery of new transient phenomena: we are likely witnessing the dependence of the transients on stellar mass, metallicity, mass loss rate and binary interaction.

1.1 Supernovae Classification

SN classification is based on the identification of individual features in the optical spectra near maximum luminosity. These spectra show the properties of the stellar outer layers, since the ejected material is still optically thick. A fine-tuning of the classification is then performed studying the parameters of the light curves built over several months of photometric observations (Turatto 2003). In Figure 2 typical light curves and early spectra of standard SNe events are displayed. In 1941 Minkowski identified two main classes

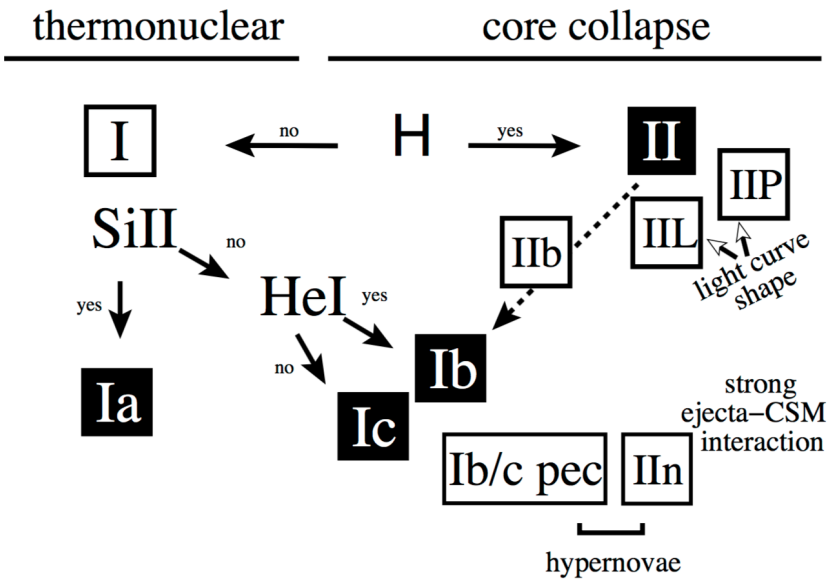

Figure 3: Schematic overview of SNe classification. The different explosion mechanism is highlighted above the diagram. The four main classes are highlighted through black squares (Figure from Turatto 2003).

of objects: those that did not show hydrogen lines were defined as "Type I" events (SN I), while spectra that displayed clear hydrogen features were labelled "Type II" events (SN II) (Figure3). Later this eary classification scheme was expanded, as more variety was found in the two main classes. Type I SNe have been split into three sub-types:

SN Ia present strong Si II features but no He I lines in their spectra;

SN Ib show no hint of Si II and their spectra are dominated by He I lines;

SN Ic only show very weak Si II and He I lines, with prominent O I and Ca II lines.

On the other hand, SN II spectra clearly show Balmer lines and may be divided into four sub-classes, depending on their light curve shape and spectroscopic properties:

SN IIP exhibit a period of constant luminosity for up to 100 days after maximum brightness. The flat portion of the light curve is called "plateau", and is followed by a rapid luminosity decline;

SN IIL show a fairly rapid, linear decline in magnitude after maximum light.

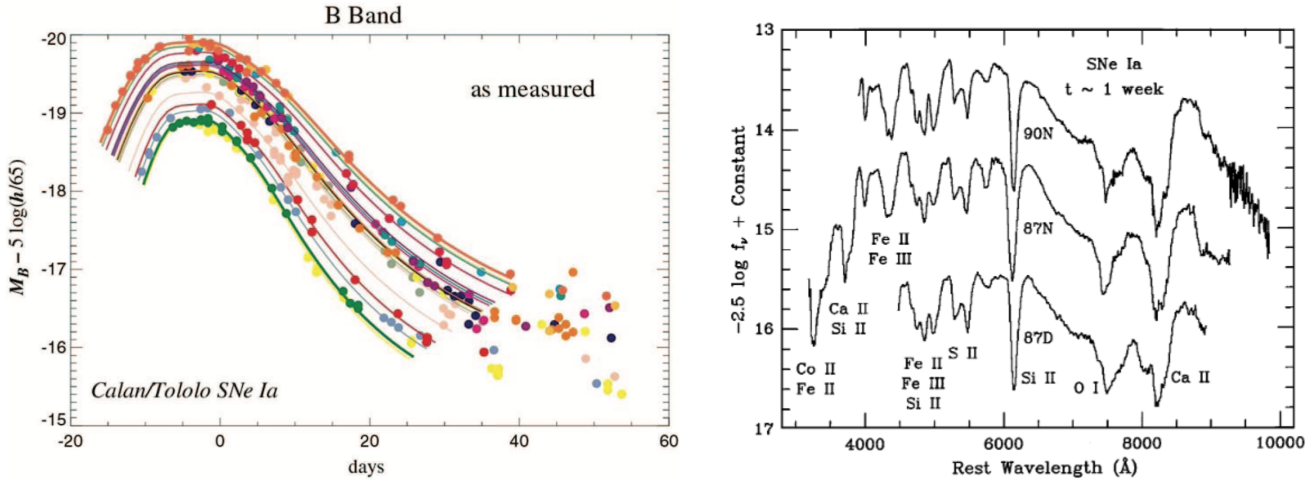

Figure 4: On the left, typical SN Ia B-band light curves. Empirical correlation was found between decline rates and absolute peak magnitude (eg Phillips 1993). On the right, spectra from three different supernovae were taken a week after maximum brightness. Both light curves and spectra show the homogeneity of standard SN Ia (Figures from Miquel 2007 and Filippenko 1997).

SN IIn are characterized by narrow spectral lines, likely related to the interaction of the ejecta with the slowly expanding circumstellar medium;

SN IIb show broad Hydrogen lines during the first weeks, evolving towards SN Ib later on.

1.2 Type I Supernovae

1.2.1 SN Ia

Type Ia Supernovae are the most common kind of stellar explosion and occur in all types of galaxies (Branch D. 2017), including those with no sign of star formation. It is now widely accepted that SN Ia originate from the thermonuclear explosion of a Carbon-Oxygen White Dwarf (CO WD), leaving no remnant behind (Branch et al. 1995). Light curves of SN Ia are characterized by a fast rise to maximum (16-18 days), well reproduced by a fireball model, where the luminosity increases as t^2 (Leibundgut 2000). Around 30 days after maximum brightness, many objects show a "secondary shoulder" in the infrared bands, with variable strength and duration. After $\sim$ 50 days

the decline in luminosity is exponential, powered by the radioactive decay $^{56}Co \longrightarrow {}^{56}Fe$. Spectra of SN Ia show no evidence of H or He lines, but many intermediate mass elements are recognizable, including calcium, silicon and sulfur. The spectra at late phases are instead dominated by the iron group emission lines. In Figure 4 a sample of light curves and spectra for standard SN Ia are shown. The search for the progenitor systems of SN Ia is not an easy task. In order to ignite nuclear fusion inside a stable core supported by the degeneracy pressure, it is necessary to have an interaction between the WD and a companion star. Two main progenitor channels were proposed: the Single Degenerate and the Double Degenerate scenarios. The former envisions a main sequence star or a red giant filling the Roche Lobe of a CO WD: part of the envelope of the non-degenerate star is accreted on the WD until explosive carbon burning is ignited just before reaching the Chandrasekhar mass, which is the maximum mass that can be supported by the pressure of a degenerate gas of electrons. The Double Degenerate scenario invokes a binary system of CO WDs which loses angular momentum through gravitational waves emission. If the sum of the masses of the two stars exceeds the Chandrasekhar mass, the merger ignites carbon burning and leads to the explosion of the system (for a review on Type Ia progenitors see Maeda & Terada 2016). Given the number of observational constraints, no single model is able to perfectly reproduce the experimental data: it is possible that both the Single and the Double Degenerate scenario lead to the thermonuclear explosion of a WD, accounting for the variety of features observed.

1.2.2 SN Ib and SN Ic

SN Ib and SN Ic are thought to originate from massive stars stripped of their hydrogen envelopes which undergo core collapse: for this reason they are also labelled "stripped envelope SNe". SN Ib/c only appear in spiral galaxies, in proximity of star forming regions, suggesting young and massive progenitors (Branch D. 2017). Their light curves appear similar to those of SN Ia, with a fast rise and a subsequent slow, linear decline in magnitude that roughly follows the radioactive decay of ^{56}Co (Figure 5). Early spectra are characterized by the presence of O I, Ca II, Fe II and Ti II lines, while in later phases spectra are dominated by forbidden lines like [O I], [Ca II], and [Fe II] (Tartaglia 2015). It is tempting to assume that SN Ib originate from the core collapse of Wolf-Rayet stars which lost their hydrogen envelope, while SN Ic originate from Wolf-Rayet stars which shed both their hydrogen and their helium envelope (Dessart 2015). However, the lack of detection

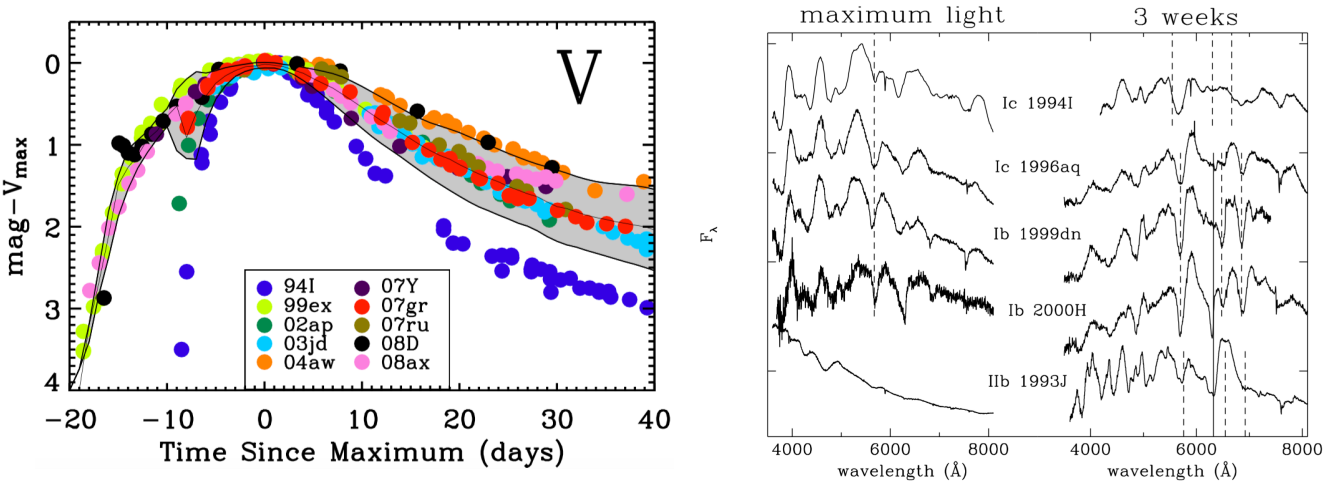

Figure 5: On the left, light curves for 10 well-studied SN Ib/c, normalized at maximum brightness. The grey area represents a mean template light curve, built showing 1 σ deviations from the mean magnitude at each epoch. From $\sim$ 20 days onward the decline is powered by the ^{56}Co decay. On the right, spectral evolution of SN Ib and SN Ic from the moment of maximum brightness to three weeks later. For reference, appropriately blue-shifted He I lines are shown as dashed lines, while Hα is represented as a solid line. (Figures from Drout et al. 2011 and Turatto 2003).

of the progenitors in pre-explosion images shows that an additional channel involving lower mass stars is plausible (Smartt 2009). Close binary systems may lead to the formation of helium stars with a wide range of masses, even able to explain the observed SN Ib/c rates without invoking single-star progenitors (Yoon et al. (2010)).

1.3 Type II Supernovae

Type II SNe display a variety of different features both in their light curves and in their spectra (Figure 6). These stellar explosions originate from the core collapse of massive progenitors, and are therefore tightly associated with star-forming regions like stripped envelope SNe (Branch D. 2017). Masses of the progenitors span from $\sim$ 8 $M_\odot$ to over 25 $M_\odot$, leaving a neutron star as compact remnant (Smartt 2009). More massive stars may collapse onto a black hole or explode through the pair instability mechanism (M > 140 $M_\odot$) (Kasen et al. 2011). On the other extreme of the mass function, it is still unclear whether stars with 8 $M_\odot$ < M < 12 $M_\odot$ end their lives as O-Ne-Mg

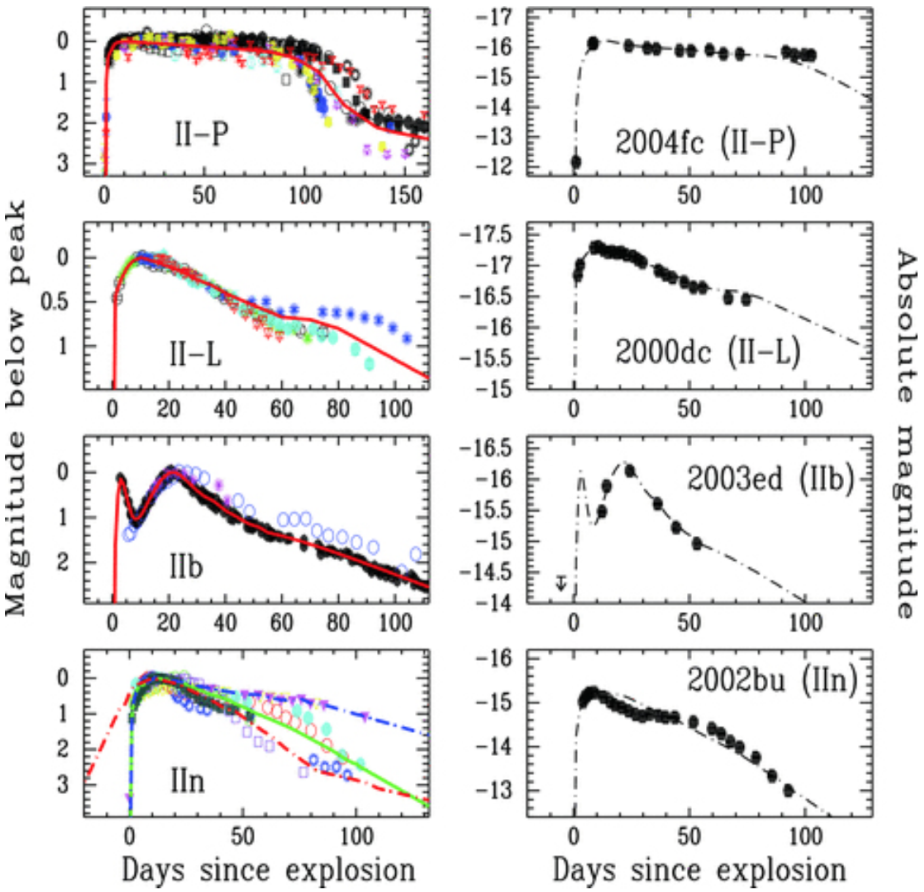

Figure 6: Light curves of several type II SNe. For each class of objects an average light curve is built and fitted to a single event on the right panels. For SN IIn three average light curves are shown: fast, average and slow declining (Figure from Li et al 2011).

white dwarfs or undergo core collapse (see section 1.4.1).

1.3.1 SN IIP and SN IIL

SN IIP are the most common type of explosion among the type II supernovae, making up roughly 70 % of the observed core collapse events (Li et al. 2011a). Among the SN IIP class, the peak luminosity may vary by a factor ~ 100 and the light curve shape may differ significantly, suggesting a wide diversity of progenitor stars. At the early phases, the shocked material is responsible for the SN luminosity: these layers cool down through an almost adiabatic expansion, causing a steady drop in luminosity. When the temperature drops

to 10000 K in the outer layers, hydrogen starts recombining: this recombination wave powers the plateau phase. The photosphere recedes in mass, but maintains roughly the same radius and temperature (T $\sim$ 5500 K), resulting in a constant luminosity (Branch, Wheeler 2017a). SN IIL probably don't have the massive hydrogen envelopes needed to keep the luminosity constant for one hundred days. After 150 days both SN IIP and SN IIL light curves settle onto an exponential decay powered by the ^{56}Co radioactive decay to ^{56}Fe. SN IIP usually eject $\sim 0.1 M_{\odot}$ of ^{56}Ni, which decays in ^{56}Co with a 6.1 days halflife (Branch, Wheeler 2017a). The spectra of the SN IIP in the early phases show a blue continuum, denoting a colour temperature higher than 10000 K (Filippenko 1997). There is a lack of noticeable features, except for shallow Balmer and He I lines. As time passes, spectral features become recognizable and during the plateau Balmer and Ca II lines appear, showing well developed P-Cygni profiles. Weaker lines of FeII and other iron-group elements also show up. Since the velocity of the ejecta at the photosphere diminishes constantly, the P-Cygni profile becomes progressively narrower. During the ^{56}Co decay-powered decline, the continuum fades and spectra are dominated by Hα, [O I], Ca II and [Ca II] emission lines. The spectral evolution of a typical SNIIP is shown in Figure [8]a. SN IIL present very similar spectra to SN IIP: the only striking difference seems to be the frequent absence of blueshifted absorption for Hα (Filippenko 1997).

1.3.2 SN IIn

Among core collapse SNe it is possible to find objects with narrow emission lines, that lead to infer an expansion velocity ranging from few 10 km/s to $\sim$ 1000 km/s (Schlegel 1990). These objects are called SN IIn and are thought to arise from interaction between the fast expanding SN ejecta and a dense circumstellar medium (CSM), previousy expelled by the star itself through mass loss episodes . Studying the bolometric light curve of a SN IIn, it is possible to estimate the mass loss rate of the progenitor, which often results higher than 10^{-3} M$_{\odot}$ year^{-1} (Moriya et al. 2014). In Figure 7 typical SNIIn spectra are shown. The narrow lines originate from the photoionized, slowly expanding CSM, while high velocity (v $>$ 10000 km/s) ejecta are responsible for the broad component, which is sometimes visible under the narrow CSM lines. Since there is a heavy dependence on the mass loss history of the progenitor, SN IIn can show a variety of different features, making them quite a heterogeneous class of objects.

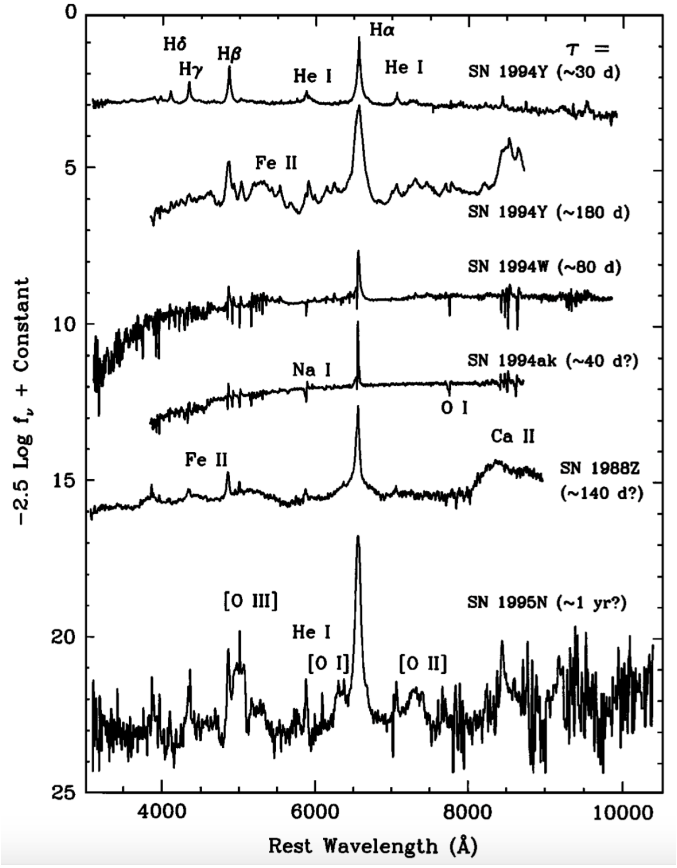

Figure 7: Several spectra for SN IIn events: narrow Balmer lines indicate low expansion velocity of the emitting material. The epochs refer to the estimated time of explosion rather than the time of maximum brightness, since rise to maximum can differ significantly among SN IIn (Figure from Filippenko 1997).

1.3.3 SN IIb

SNIIb are a subclass of type II SNe originating from the explosion of a massive star which has lost most of its hydrogen envelope (Branch, Wheeler 2017b): this may have been caused by mass loss events or binary interaction. At the early phases the spectra show evident Balmer lines, but they are replaced with strong He I lines as soon as the photosphere recedes beyond the thin hydrogen envelope into deeper ejecta layers. After the appearance of helium, both the light curve and the spectra resemble those of SN Ib, making SN IIb a link between envelope retaining SN II and stripped envelope SN Ib/c (Turatto 2003).

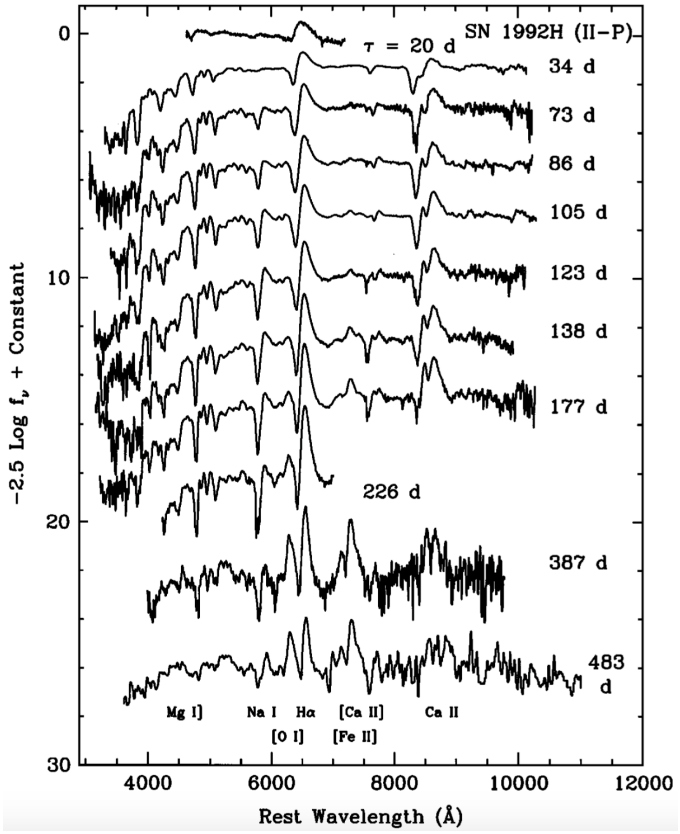

Figure 8: Spectral evolution of SN 1992H in NGC 5377, with typical P-Cygni profiles. As the velocities of the ejecta quench with time, the profile gets narrower. In late stages iron group emission lines show up over a flat continuum (Figure from Filippenko 1997).

1.4 Core Collapse Mechanism

Stars with masses greater than ~ 8 $M_\odot$ undergo core collapse as the last stage of their evolution (Smartt 2009). The contraction of these massive stars cannot be stopped by electron degeneracy, and they successfully ignite ^{12}C in a non degenerate environment. From this point onward, the evolution of the core is sensitively accelerated by neutrino losses: due to their long mean free path, neutrinos efficiently dissipate the energy produced from nuclear burning. In response, the star contracts and heats up according to the virial theorem, increasing the nuclear reaction rates and hence neutrino losses. For this reason, evolution after ^{12}C ignition only lasts few 10^3 years (Chiu 1961). Stars with $M > 10$ $M_\odot$ complete nuclear burning cycles until they form a stable ^{56}Fe core, which has the greatest binding energy per nucleon: at this

point nuclear burning processes stop, as they would be endothermic. At the end of their burning cycles, massive stars present an inert ^{56}Fe core (typically $\sim$ 1.5 $M_\odot$) surrounded by concentric burning shells, remnant of the previous burning phases. Since no nuclear burning process is active in the iron core, the core starts contracting in a timescale defined by neutrino losses. Due to the high temperature and density of the core, the collapse cannot be stopped by the electron degeneracy pressure: an extremely relativistic gas of degenerate electrons has an equation of state too soft to restore the dynamical stability (Janka et al. 2007). The collapse is accelerated by electron capture and photodisintegration processes. Electron captures reduce the electron degeneracy pressure and decrease the effective Chandrasekhar mass (M_{Ch} $\sim$ 5.76 Y_e^2 $M_\odot$, where Y_e is the mean number of electrons per nucleon), fostering the dynamical instability. Photodisintegration kicks in at T $\sim 10^{10}$ K, when iron-peak nuclei are broken into α particles, protons and neutrons. Photodisintegration of heavy elements require $\sim$ 2 MeV per nucleon: this energy is absorbed from the radiation field, leading to a drop in the internal energy and therefore a drop in pressure exerted by photons (Branch, Wheeler 2017c). The inner iron core ($\sim$ 0.7 $M_\odot$) undergoes a homologous contraction, while matter outside the homologous core is approximately in free fall. The collapse is stopped by the pressure of the degenerate gas of nucleons, in particular neutrons formed through electron captures. The maximum central density reached is $\rho_c \sim 6\text{x}10^{14}$ g cm^{-3}, which is twice the nuclear density: the inner core experiences a bounce back, impacting the free falling material and forming a shock wave (Branch, Wheeler 2017d). This "bounce shock" is not able to drive a prompt explosion, since it is quenched by neutrino losses and dissociation of ^{56}Fe into α particles (Myra, Bludman 1989). One popular mechanisms proposed to power the explosion is the absorption of neutrinos produced by matter accreting on the stiff nucleon core. Absorbing $\sim$ 1% of the outgoing neutrino flux would be sufficient to revitalize the shock and blow up the outer layers of the star: see the work by Janka (2001) for a detailed discussion on shock revival by neutrino heating.

1.4.1 Electron Capture Supernovae

Stars within the range of masses 8 $M_\odot$ < M < 10 M $_\odot$ are thought to form a degenerate Oxygen-Neon-Magnesium core through nonexplosive ^{12}C burning, also undergoing thermal pulses (Ritossa et al. 1996). Given their similarities with AGB stars, these objects are labelled "Super-AGB stars", and their fate is uncertain due to the many complications involved in modelling their interiors and evolution, especially regarding the role of mixing, con-

vective overshooting and mass loss rates (Poelarends et al. 2008). Whether super-AGB stars evolve in a O-Ne-Mg WD or undergo core collapse through electron capture is still being investigated (Doherty et al. 2017).

Electron captures are especially significant in the case of strongly degenerate O-Ne-Mg cores: if such core can grow (through shell burning) to 1.38 $M_\odot$, electron captures on ^{24}Mg and ^{20}Ne isotopes should lead to dynamical instability and therefore collapse of the core, giving birth to an "electron-capture supernovae" (EC-SN) (Leung et al. 2019). Zha et al. (2019) follow the evolution of a 8.4 $M_\odot$ star from the main sequence to oxygen ignition in its strongly degenerate O-Ne-Mg core and then perform two-dimensional hydrodinamical symulations for the oxygen deflagration to investigate the fate of the star. An interesting result is that the star undergoes core collapse if the central density at the start of the deflagration is $\rho_c > 10^{10.01}$ g cm^{-3}, while a thermonuclear explosion occurs if $\rho_c < 10^{10.01}$ g cm^{-3}. Since estimated central density at the start of the deflagration exceeds the critical value of $10^{10.01}$ g cm^{-3} (Takahashi et al. 2019, Zha et al. 2019), the core is expected to collapse, leaving a relatively low-mass neutron star. A new class of objects is being investigated as possible EC-SN candidate (Botticella et al. 2009, Pumo 2010).

1.5 Supernovae Impostors and Gap Transients

Among the transients that populate the luminosity gap between supernovae and classical novae, there are some events that reproduce SNe features without actually disrupting the star itself, earning the name of "supernova impostors" (Van Dyk et al. 2000). On the other hand, some Gap Transients are thought to be faint core collapse supernovae (Pastorello et al. 2007a, Botticella et al. 2009). Our present time understanding on the subject is summarized by Pastorello & Fraser (2019), where the main classes of Gap Transients are identified.

1.5.1 Supernova Impostors

Supernova impostors are non terminal eruptions of massive stars, often associated with Luminous Blue Variables (LBVs) (Humphreys et al. 1999). Stars with masses M > 40 $M_\odot$ may undergo an unstable phase with hectic variations in magnitude after exhausting hydrogen in their core and before reaching the Wolf-Rayet stage (Figure 9). The hydrogen envelope is quickly

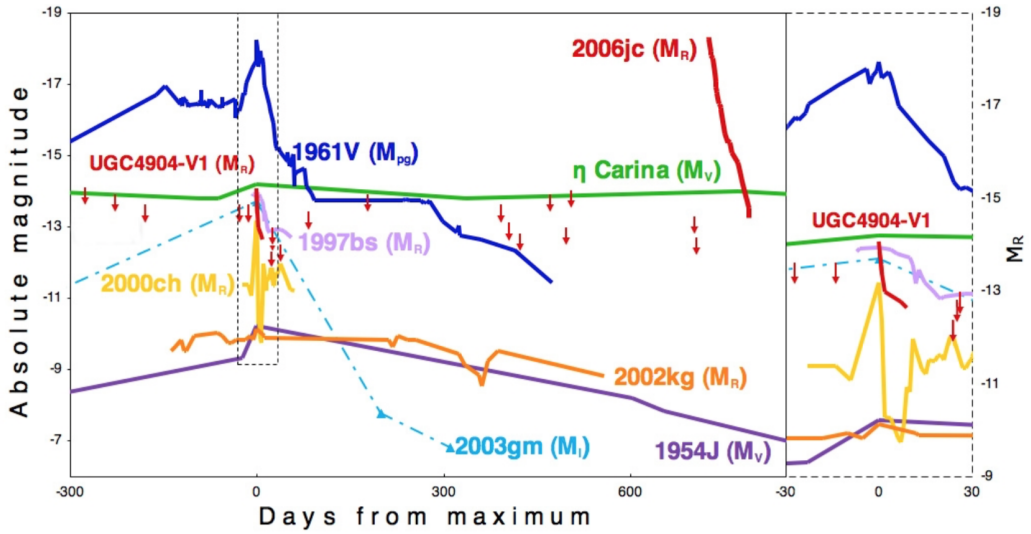

Figure 9: Several LBVs light curves: the eruptions appear to be erratic and can differ greatly in luminosity. In the case of SN2006jc, the supernova explosion was heralded by a LBV-like event, here labelled UGC4904-V1 (Figure from Pastorello et al. 2007b).

lost with a rate of $\sim 10^{-4} - 10^{-5}$ $M_\odot$ yr^{-1} and forms a massive circumstellar nebula around the star. Well-known examples of LBVs are η-Carinae and P Cygni. Spectral features of LBVs resemble those of SN IIn, in particular the narrow emission lines (v $\sim 10^2$ to 10^3 km s^{-1}) resulting from the photoionization of circumstellar material previously ejected. An important spectral difference between LBVs and SN IIn lies in the absence of broad lines under the narrow lines, indicating that there are no fast-expanding ejecta, usually associated with the terminal explosion of a star. The mechanism that drives the outbursts is still unclear: close encounters are a viable explanation for binary stars, while super Eddington continuum driven winds are proposed for isolated stars (Owocki et al. 2004).

1.5.2 Mergers

Mergers in close massive binary systems may give birth to Gap Transients called "Luminous Red Novae" (LRNe), which show a characteristic double peaked light curve (Figure 10, upper panel). Spectra taken at the first luminosity maximum present a blue continuum with H and Fe II emission lines. At the second peak, the spectra becomes similar to that of G or K-type stars, with narrow metal absorption lines and weaker Balmer lines. During the final

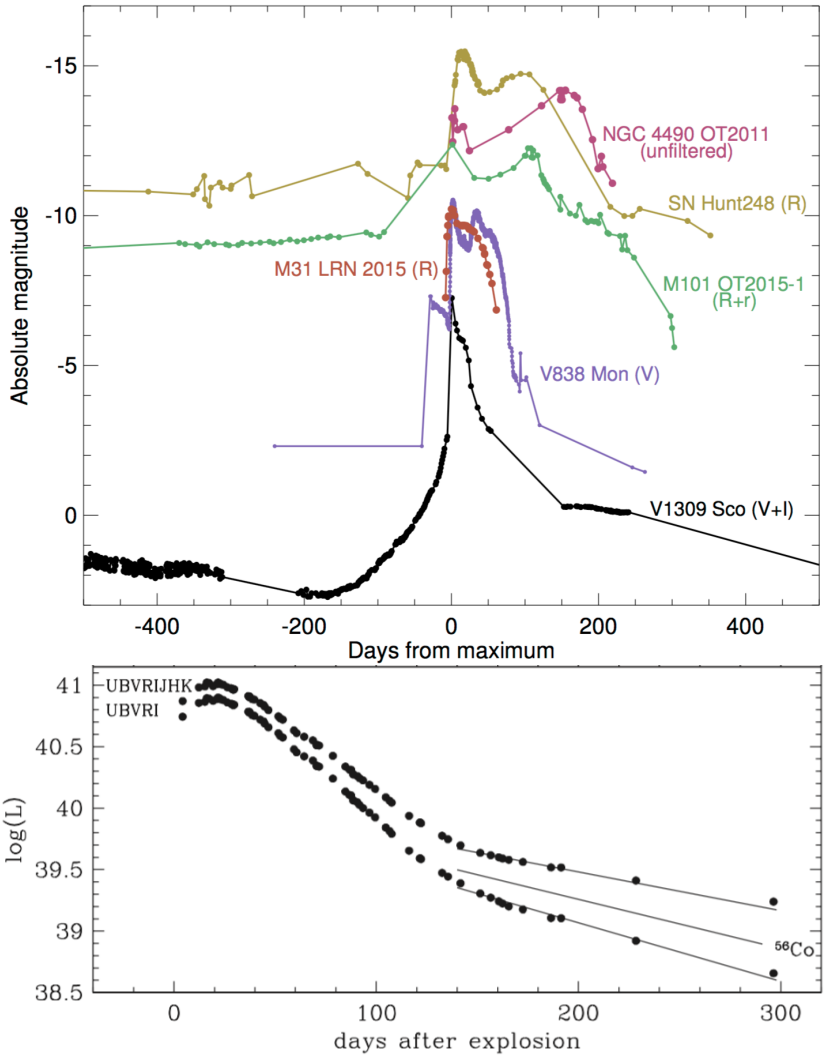

Figure 10: Top panel: light curves for merger candidates, most of which show the typical double peaked shape. Bottom panel: the ILRT SN 2008S displays a SN IIL-like bolometric light curve that follows the ^{56}Co decay at the latest stages of its evolution (Figures from Metzger, Pejcha 2017 and Botticella et al. 2009).

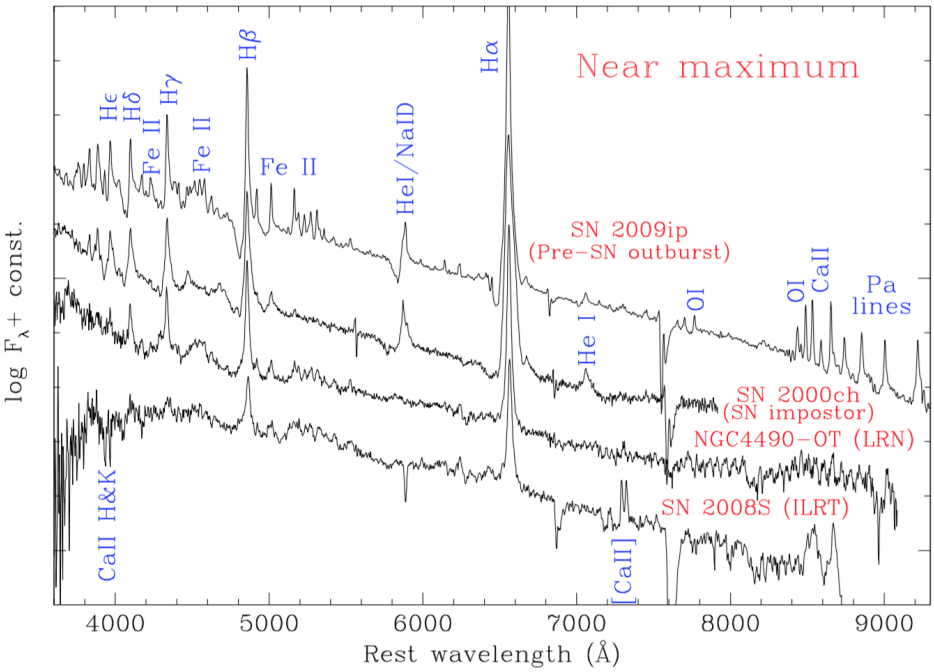

Figure 11: Spectra near maximum for different types of gap transients. The [Ca II] doublet is a distinctive feature for ILRT that remains detectable throughout the whole spectral evolution (Figure from Pastorello & Fraser 2019).

decline, LRNe spectra evolve toward those of M-type stars, showing strong molecular absorption bands and again a prominent Hα emission. The LRN prototype is V838 Mon, but the origin of these transients as mergers was identified through the study of V1309 Scorpii (Tylenda et al. 2011, Mason et al. 2010). The periodic modulation of luminosity allowed to infer the presence of a binary system with a period of d $\sim$ 1.4 days. In the years before the outburst the period was following an exponential decrease, interpreted as the shrinking of the binary orbits, until the two stars merged. The first light curve peak is powered by the ejected common envelope, which emits radiation while expanding and cooling. The second peak appears after the interaction between the fast expanding common envelope and the slow outflows on the equatorial plane, which formed during the inspiral of the binary system (Metzger, Pejcha 2017). The absolute magnitude of the merger may vary greatly ($-15 < M_V < -4$ mag), owing to the wide range of masses involved: frequent, faint event are produced by low mass mergers, while luminous transients are linked with more massive binary systems (Kochanek et al. 2014).

1.5.3 Faint Core Collapse Supernovae

Faint core-collapse supernovae may also populate the gap. "Intermediate Luminosity Red Transients" (ILRT) are plausible examples of EC-SN: the prototype of these objects is SN 2008S (Botticella et al. 2009), which showed a light curve similar to a faint SN IIL, with an early peak and a late decline compatible with the ^{56}Co decay (Figure 10). Spectral features include Hα, near-infrared Ca II triplet and the [Ca II] doublet at 7291.5 Åand 7323.9 Å. This doublet is a distinctive trait of the ILRT, unique among gap transients (Figure 11). The progenitor of SN 2008S and other ILRT were detected in the mid-infrared domain thanks to Spitzer, while optical and near-infrared images from HST failed to identify a pre-outburst source. This points toward a star embedded in a cocoon of dust which is later sublimated by the explosion. It is still debated whether SN 2008S-like transients are actually terminal events or stellar outbursts (Smith et al. 2009): in the following section we present the case of NGC300OT, a crucial ILRT which may shed light on this peculiar class of objects.

2 Electron Capture Supernova Candidates

The nature of Intermediate Luminosity Red Transients (ILRT) is still debated. An important mechanism that could give birth to these gap transients is the electron capture supernova (EC-SN) scenario, where the collapse of the stellar core is triggered by electron capture reactions. These events are thought to originate from stars with initial masses of ∼8-10 $M_\odot$. Adopting Pumo et al. (2009) conventions, let M_{up} be the initial mass above which a star ignites carbon, and M_{mas} the mass above which a star completes all nuclear burning cycles, leading to the collapse of an iron core. Stars with initial masses spanning from M_{up} to M_{mas} are called Super-AGB stars (Ritossa et al. (1996)). After carbon burning they develop an inert, degenerate O-Ne core, and they can be considered as more luminous and more massive AGB stars undergoing thermal pulses and mass loss episodes. The fate of Super-AGB stars depends on the competing effects of mass loss and core growth. If the hydrogen-free core is accreted through shell burning up to 1.38 $M_\odot$, electron captures on ^{24}Mg and ^{20}Ne will trigger the collapse of the core, leading to an EC-SN (Poelarends et al. 2008, Leung et al. 2019). High mass loss rates, on the other hand, can quench shell burning and inhibit the growth of the core, giving birth to a O-Ne-Mg white dwarf. Following the model described by Poelarends et al. (2008), EC-SN originate from the collapse of O-Ne-Mg cores of ∼9 $M_\odot$ super-AGB stars in a 0.25 $M_\odot$ range, with some studies extending the mass window up to 1.5 $M_\odot$ (Siess 2007). Further uncertainties are added by the metallicity dependence of M_{up} and M_{mas} (Pumo et al. 2009). EC-SN are predicted to display distinctive features: luminous super-AGB progenitors (∼10^5 $L_\odot$, Poelarends et al. 2008), low explosion energies (∼10^{50} erg) and low ejected ^{56}Ni mass (few 10^{-3} $M_\odot$, Wanajo et al. 2009). Pumo et al. (2009) suggest that EC-SN light curves may resemble faint SNII, showing IIP or IIL behaviour depending on the mass of the hydrogen envelope the star is able to retain before the collapse. The transients SN2008S and NGC300OT, prototypes of ILRT, find a consistent interpretation in the EC-SN framework.

2.1 The first ILRT: SN2008S

SN2008S is a faint optical transient (OT) discovered by Arbour, Boles (2008) in NGC 6946 (5.7 ± 0.3 Mp, Sahu et al. (2006)) and later observed by Botticella et al. (2009) with an excellent sampling. The peak absolute magnitude of M_V = -14.17±0.16 mag places this transient in the luminosity gap between classical novae and faint SNe. After maximum luminosity, the light

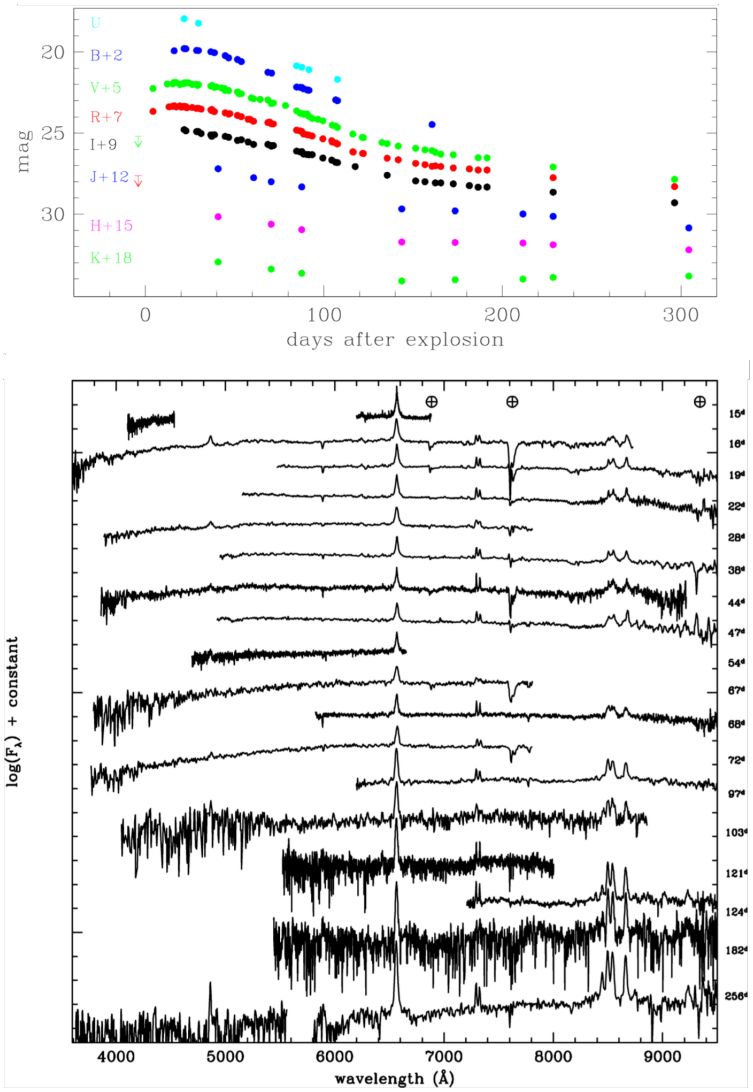

Figure 12: Top panel: UBVRIJHK light curves of SN2008S. Bottom panel: spectral evolution of SN2008S, corrected for Galactic extinction. The phase from the explosion is reported on the right, while the symbols $\oplus$ mark the positions of the main telluric absorption features. Hα, the [CaII] doublet and the CaII triplet are clearly detectable at all epochs (Figure from Botticella et al. 2009).

curve declines linearly with time, resembling that of a faint SNIIL (Figure [12], left panel). Between 140 and 290 days, the decline rate is 0.88 ± 0.05 mag/100 d, compatible with the decay of ^{56}Co (1.023 mag/100 d) (Botticella et al. 2009). Assuming that the late ligh curve tail is powered by radioactive decay of ^{56}Co, the inferred mass of ^{56}Ni produced is as low as 0.0014 ± 0.0003 $M_\odot$, not far from the window of 0.002 - 0.004 $M_\odot$ predicted by Wanajo et al. (2009) for EC-SNe. Optical spectra show a slow evolution, with strong Hα, [CaII] doublet and CaII triplet emission lines, without broad P-Cygni profiles (Figure [12], right panel). The [CaII] forbidden doublet is a rare feature, seldom seen in stellar spectra. In fact, in a dense environment the electrons that would produce [CaII] lines are collisionally de-excited to the ground state before decaying through photon emission (Humphreys et al. 2011). As a consequence the [CaII] doublet must form in a low density medium. Furthermore, the excited Ca^+ ions that would produce the [CaII] doublet can be ionized to Ca^{++} by a photon with wavelenght 1218.9 Å, only a few Å from the Lyα line. A Lyα line broader than ∼800 km s^{-1} would strongly suppress the [CaII] emission (Berger et al. 2009): since we clearly see the forbidden doublet, we expect expansion velocities not larger than ∼1000 km s^{-1} for SN2008S.

Fe II, O I, Na I and Mn II multiplet 4 are also identified in the spectra (Botticella et al. 2009). The [Ca II] doublet and Fe II lines present a narrow, asymmetric profile with a prominent red wing, while Hα, Hβ and the CaII triplet show broader lines with multicomponent profiles (figure [13], left). In the early spectra in particular, the Hα line exhibits narrow, intermediate and broad components with FWHM velocities of $v_n \sim 250$ km s^{-1}, $v_i \sim 1000$ km s^{-1} and $v_b \sim 3000$ km s^{-1} respectively (Botticella et al. 2009). It is possible to associate the broad component with high velocity ejecta, the intermediate component with shocked circumstellar medium and the narrow component with unshocked circumstellar medium. The absence of high velocity absorptions or P-Cygni profiles, however, suggest that we are not directly looking at the ejecta. Multiple photon-scattering events with thermal electrons may broaden the wings of a narrower component, thus accounting for the observed broader components (Dessart et al. 2009). In this case, the fastest expanding component would have at $v_i \sim 1000$ km s^{-1}, compatible with the presence of the [Ca II] doublet, as discussed above.

A progenitor star was identified by Prieto et al. (2008) in pre-explosion images taken from Spitzer in the mid-infrared (with detections at 4.5, 5.8 and 8.0 μm). The same target was not found in deep optical and near-infrared (NIR) images obtained by the Hubble Space Telescope (HST) and the Large Binocular Telescope (LBT). The best fit on the observations performed with

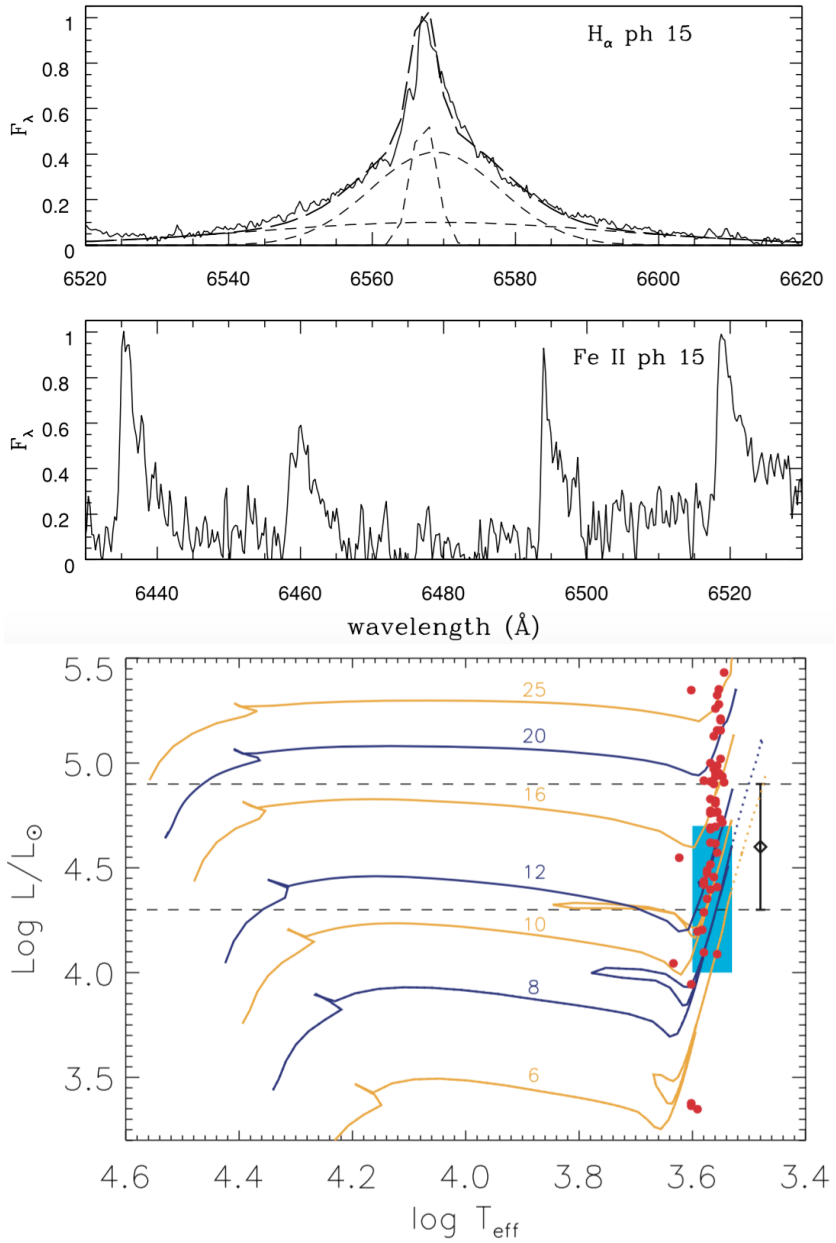

Figure 13: Left panels: narrow wavelenght regions of the spectrum of SN2008S taken 15 days after the explosion. It is possible to appreciate both the multiple components of the Hα and the asymmetric red wings of the FeII emission lines. Right panel: HR diagram containing the evolutive tracks for stars between 6 and 25 $M_\odot$. Red dots mark the positions of Red Supergiants (RSG) in the Milky Way, while the shaded area identifies the region occupied by RSG progenitors of SNIIP. The progenitor of SN2008S is shown as a black point with error bar (Figures from Botticella et al. 2009).

a single-temperature blackbody provides a bolometric luminosity of 3.5 x $10^4 L_\odot$ and a temperature of ∼440 K (Prieto et al. 2008). These measures, along with the optical upper limits, suggest the presence of a fairly massive star engulfed in a cocoon of dust. This material was previously ejected through a steady wind or mass loss episodes. Based on the bolometric luminosity of the source, Prieto et al. (2008) deduce a progenitor mass of ∼10 $M_\odot$ with an upper limit of 20 $M_\odot$. Botticella et al. (2009) estimate, through the code DUSTY, a luminosity of $10^{4.5} L_\odot$ and a temperature of 3000 K for the central source irradiating the surrounding dust. On the HR diagram, such star is consistent with an evolved 6-9 $M_\odot$ star (Figure [13], right panel). These considerations make the progenitor of SN2008S compatible with a super-ABG star, endorsing the EC-SN scenario.

2.2 Discovery of NGC300OT

On 2008 May 14, an OT of magnitude 14.2 was discovered in the nearby galaxy NGC 300 (1.88 ± 0.05 Mpc, Gieren et al. 2005) during the SN search program at the Bronberg Observatory (Monard 2008). A first analysis of the event, hereafter denoted as NGC300OT, was provided by Bond et al. (2009). Depending on the distance modulus adopted for NGC 300 and the absorption along the line of sight, the estimates of the peak V band magnitude range between $M_V \sim -12.0$ and -12.9 mag. Although the early phases follow up is not available because the object was behind the sun, the light curve is reminiscent of that of a SN IIP: after peak, it displays a period of constant luminosity before fading more rapidly. Finally, it settles on a linear magnitude decline compatible with the ^{56}Co decay (Figure [14]). Swift and Very Large Array observations did not detect a source coincident with the transient, neither in the X-rays nor in the radio domains (Berger et al. 2009). The X-ray monitoring spanned from 2008 May 20 to October 15, while radio observations extended from 2008 May 21 to November 24 (dates in UT). The upper limits determined for the luminosity of NGC300OT are roughly one order of magnitude below the faintest SN detected in the X-rays and two orders of magnitude below the faintest radio SN discovered (Berger et al. 2009).

Low-resolution spectra taken at early phases show absorption features similar to F-type stars, with Balmer and Ca II emission lines superimposed to an otherwise black body continuum. The countinuum vanishes in three months, leaving a spectrum dominated by hydrogen and calcium emission lines (Figure [15]). The Full Width at Half Maximum (FWHM) of the Hα line at

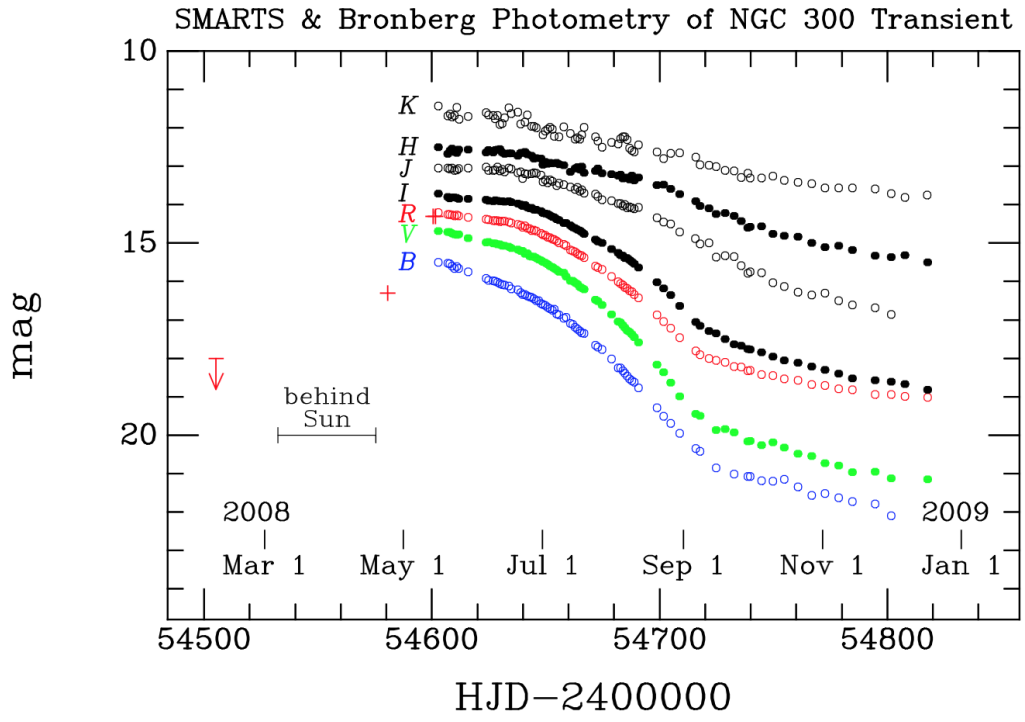

Figure 14: Published BVRI and JHK light curves of NGC300OT. Discovery and prediscovery observations are shown as crosses. The rise of the object was not observed as NGC 300 was behind the sun until end of April (Figure from Bond et al. 2009).

maximum light indicates an expansion velocity of 1050 km s^{-1}, declining to 300 km s^{-1} in June 2009 (Humphreys et al. 2011). The [Ca II] lines appear to be significantly narrower, showing a FWHM of ∼290 km s^{-1}, without clear evolution between 2008 May 23 and 2008 June 22. The CaII IR triplet displays a width similar to that of the Hα, constant during the first few months (Berger et al. 2009). The difference in line width suggests that the forbidden [CaII] doublet forms in a different region with respect to the broad lines, probably in a lower density environment, as argued above.

Thanks to the proximity of the target, it has been possible to obtain for the first time high resolution spectroscopy of an ILRT, spanning from 2008 May 20 to 2008 August 23 (Berger et al. 2009). The complex profiles of the spectral lines suggest the presence of a composite circumstellar environment, likely originating from previous mass loss episodes. The Hα line displays two narrow absorption features at all epochs: one shifted redward of 30 km s^{-1} with respect to the rest wavelength of the transition, and a weaker one

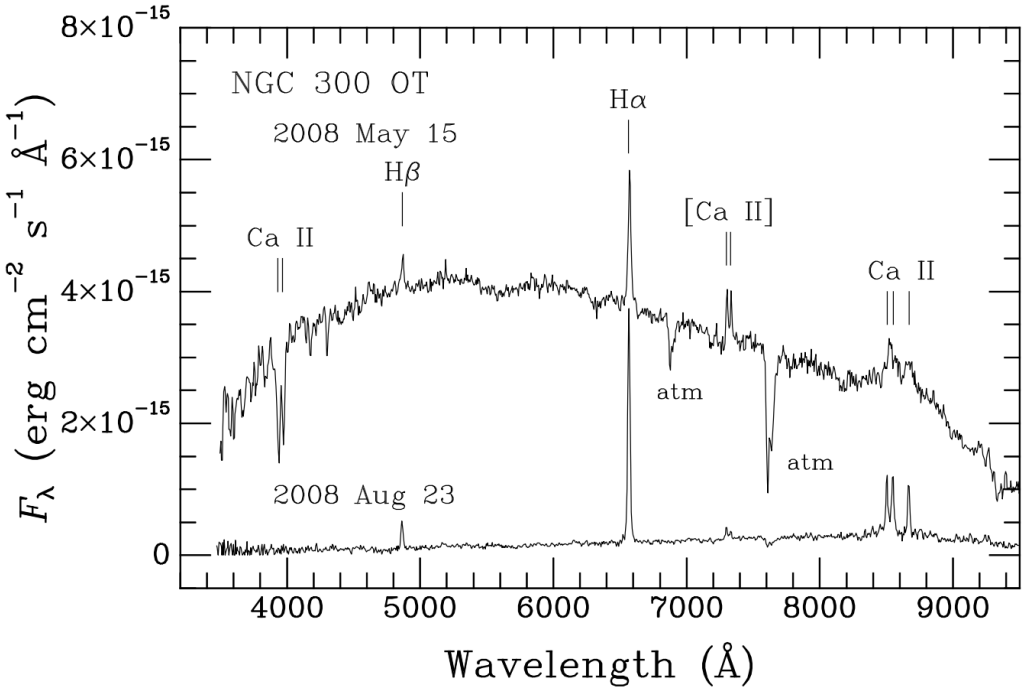

Figure 15: Low resolution spectra of NGC300OT. The early spectrum shows a continuum similar to that of an F-type star with both absorption and emission lines, while the late spectrum is dominated by H and CaII emission lines (Figure from Bond et al. 2009).

blue shifted at -130 km s^{-1}, both with a width of ∼40 km s^{-1} (Figure [16], upper left). The forbidden [Ca II] doublet shows a remarkable asymmetry, without evidence of blue wing or P-Cygni profiles (Figure [16], upper right). While Berger et al. (2009) invoke gas inflowing from outer layers to explain this feature, Humphreys et al. (2011) argue that self-absorption is highly unlikely for a forbidden emission line, and ascribe the observed asymmetry to electron scattering in an expanding envelope. The Ca II triplet presents a narrow absorption component due to interstellar medium, along with a varying number of broad absorption lines: on August 23 only a single broad absorption component is detected, while on June 6 three different absorption lines appear redward of the emission peak at 30, 80 and 200 km s^{-1}, with velocity widths of 200, 40 and 100 km s^{-1}, respectively (Figure [16], lower panel). Other features include Fe II and He I, as well as narrow OI and Na I lines: these narrow lines may originate in the interstellar medium or in a slow moving wind coming from the progenitor. Since oxygen is not abundant in the interstellar medium, the second scenario seems more reasonable (Berger et al. 2009).

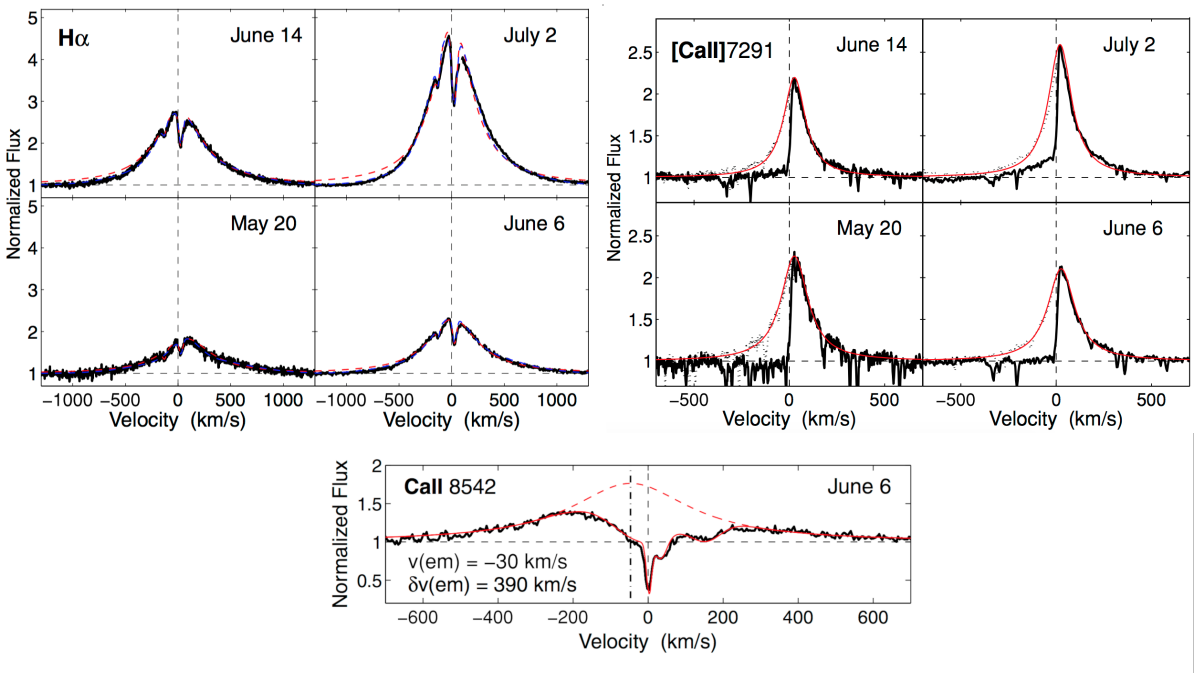

Figure 16: High resolution spectra of NGC300OT. On the upper left, Hα velocity profile taken at four different epochs. Red dashed lines indicate Lorentzian fit while blue dashed lines represent gaussian fits. The same is reproduced on the upper right for one of the [Ca II] doublet lines and in the lower panel for one of the Ca II triplet lines (Figure from Berger et al. 2009).

2.3 Progenitors of SN2008S and NGC300OT

Similarly to SN2008S, the progenitor of NGC300OT was detected by Prieto (2008) in archival Spitzer images (Figure [17], left panel). The Spectral Energy Distribution (SED) built from observations at 3.6, 4.5, 5.8, 8.0 and 24 μm is compatible with a $\sim$340 K black body with luminosity of $\sim$5.6 x 10^4 $L_\odot$ (Figure [17], right panel). No detection within 5σ was obtained from the archival HST images (Berger et al. 2009) (Figure [18], left panel). The inferred zero age main sequence mass is dependent on the stellar model, but it is around $\sim$10 $M_\odot$ (Thompson et al. 2009). The progenitor of NGC300OT is therefore identified as a massive star, in analogy with SN2008S, compatible with a super-AGB enclosed in a dusty cocoon. The study performed by Thompson et al. (2009) on the mid-infrared color-magnitude diagram of M33 reveals that the progenitors of NGC300OT and SN2008S are intrinsically rare and lay at the red end of the AGB branch. In addition, they populate a region clearly separated from LBVs, suggesting their outbursts to be different classes

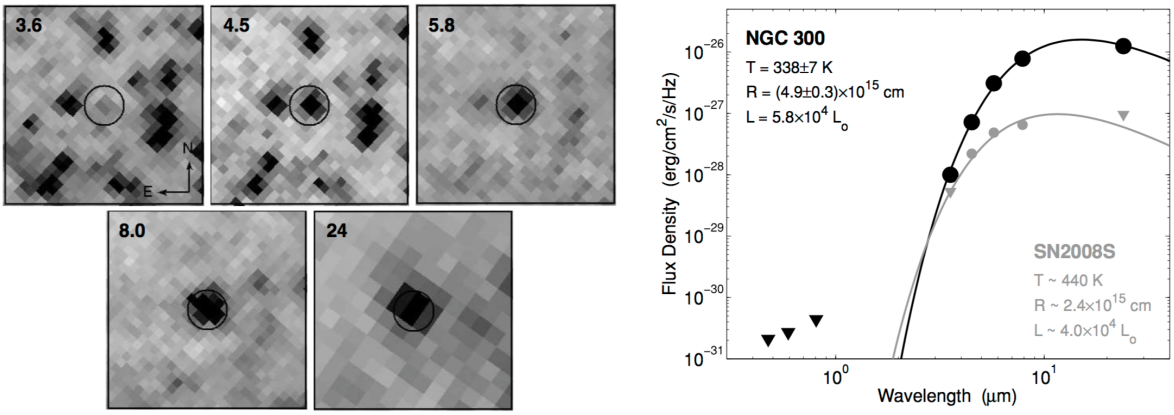

Figure 17: Left: a luminous source is clearly detected in archival Spitzer images at the location of NGC300OT. On the upper left side of each subpanel the observed wavelength in μm is dislayed (figure from Berger et al. 2009). Right, SED of NGC300OT and SN2008S progenitors, built using Spitzer observations (black circles) and Hubble Space Telescope upper limits (triangles). The two stars, like their transients, share analogous properties (Figures from Berger et al. 2009).

of gap transients (Figure [18], right panel). It is reamarkable, however, that the progenitors of NGC300OT and SN2008S differ from other extreme-AGB stars identified in M33, as they do not show clear variability in timescale of years, as opposed to the other 18 sources studied. Their small variability could be explained with high frequency thermal pulses that make their mass loss episodes appear as a steady wind (Thompson et al. 2009).

Despite this consistent scenario, a somewhat discrepant estimate for the mass of the NGC300OT progenitor is given by Gogarten et al. (2009). They suggested an alternative approach to the methods used by Prieto et al. (2008) and Botticella et al. (2009) and studied the stellar population surrounding the progenitor, with the advantage of avoiding the significant uncertainties that afflict stellar evolution models (hence the resulting mass estimate). Most transients occur in the late and fast evolving stages of stellar evolution: if the age of the neighbouring stars is known, then the mass of the progenitor can be constrained through the main sequence turnoff mass, which becomes a lower limit. This method assumes that the examined stars share the same age and metallicity, and can only be adopted when the surrounding stars are resolved, which is obviously the case of by NGC 300. Gogarten et al. (2009) find that the age of the stellar population enclosing the transient ranges from 8 to 13 Myr, corresponding to a turnoff mass of 12-17 $M_{\odot}$. Such stars would

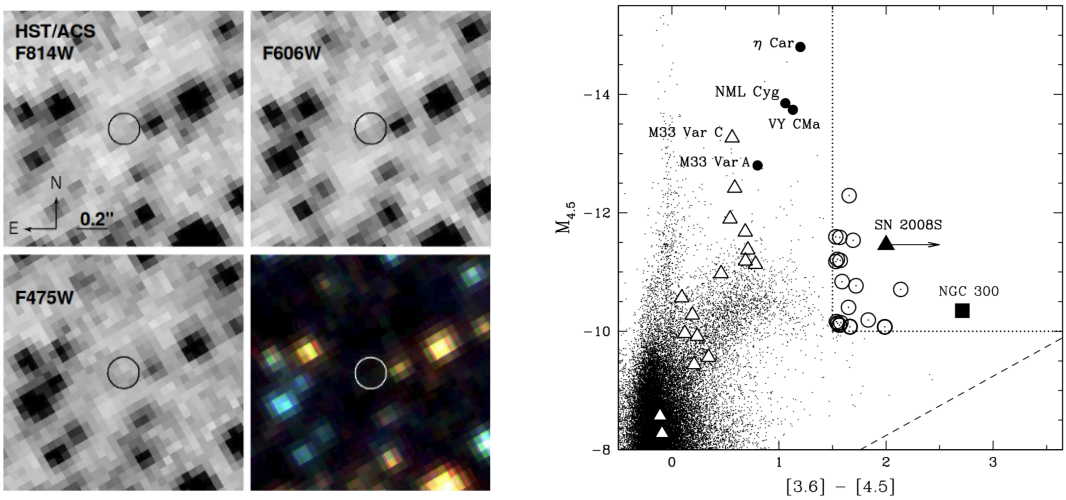

Figure 18: Left: no source is detected in the images taken from the HST at the position of NGC300OT (Figure from Berger et al. 2009). Right: color-magnitude diagram highlighting the peculiar location of the NGC300OT progenitor. On the diagram stars from M33 are also shown: open circles denote extreme AGB candidates, while open triangles indicate LBV candidates. A few yellow hypergiants, well-studied LBVs and SN2008S are added for comparison (Figure from Thompson et al. 2009)

not lead to the explosion of an EC-SN, so the transient NGC300OT must be interpreted in a different way, for example as an LBV-like outburst from a star more massive than 20 $M_{\odot}$ (Smith et al. 2009). In order to discriminate between the terminal explosion and the non-terminal eruption scenarios, late time imaging to detect the surviving star in the mid to infrared domains becomes crucial (section 2.5).

2.4 SED Evolution and the Role of Dust

Observing the absorption spectrum of NGC300OT at maximum, Humphreys et al. (2011) infer an intrinsic colour of $(B\text{-}V)_0$ ∼0.4 mag, leading to the estimate a total absorption of $A_V = 1.2$ mag, coming both from interstellar extinction and circumstellar material. Applying this correction, the analysis of the SED at the second day from detection yields a temperature of 7500 K for the photosphere, and suggests the presence of dust emitting as a black body at 715 K (Figure [19], left panel). The luminosity at maximum of the OT was 1.5 x 10^7 $L_{\odot}$. Given the temperature measured from the SED, the resulting radius of the photosphere is ∼11 AU, while the 715 K dust is

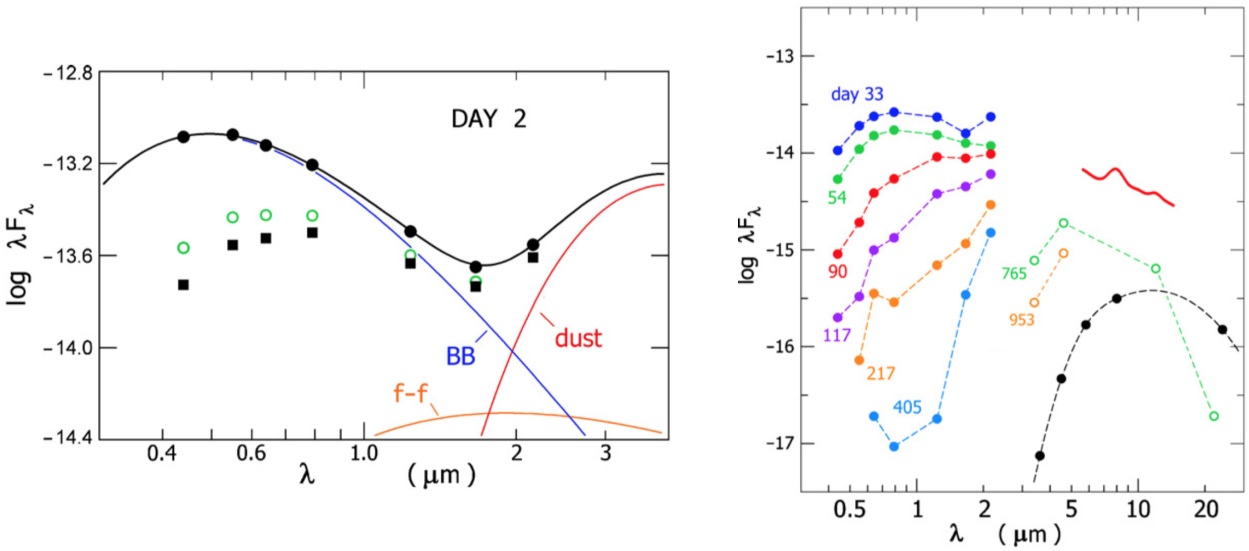

Figure 19: Left panel: early SED of NGC300OT, well fitted with a 7500 K black body from the expanding photosphere, a Free-Free component and a coll black body with a temperature of 715 K representing dust emission. Filled squares represent observed photometry, while magnitudes corrected for $A_V = 1.2$ mag are shown as filled circles. Right panel: SED evolution of NGC300OT. The SED becomes steadily redder with time, consistently with the progressive formation of dust. The SED of the progenitor is shown in black for comparison (Figures from Humphreys et al. 2011)

distant ∼1500 AU from the star (Humphreys et al. 2011). The SED becomes redder with time (Figure [19], right panel), likely due to dust formation as the environment cools down.

Mid-infrared observations may offer valuable information on the role of the dust (Prieto et al. 2009): the spectrum of NGC300OT taken by Spitzer 93 days after discovery shows broad features at 8 μm and 12 μm, which are likely associated with carbon rich dust (Figure [20], left panel). The late time SED of NGC300OT is well fitted by three black bodies (Figure [20], right panel):

1. Photosphere: T_1 ∼3890 K, R_1 ∼11 AU
2. Hot dust: T_2 ∼1500 K, R_2 ∼67 AU
3. Warm dust: T_3 ∼485 K, R_3 ∼515 AU

While the first blackbody can be easily attributed to the photosphere, the other two components require some discussion. The second component may

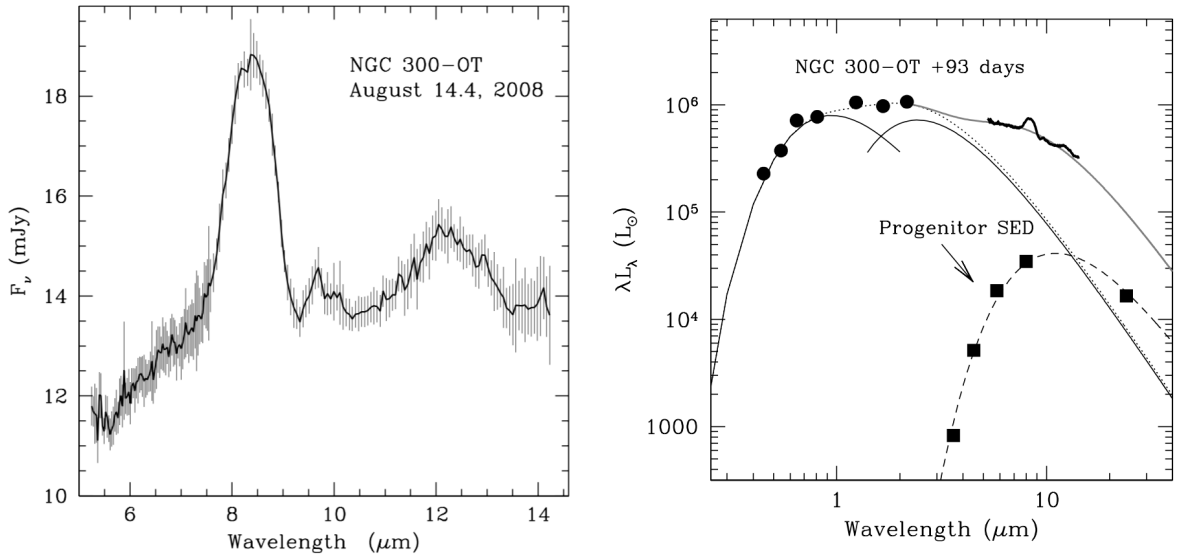

Figure 20: On the left, low-resolution spectrum of NGC300OT taken in the mid-infrared 93 days after the detection of the transient. This final spectrum was obtained mediating 20 spectra: the error bars show the root mean square of each pixel after the combination. On the right panel is shown a fit of three black bodies at different temperatures to the optical and infrared data taken 93 days after the detection of NGC300OT. Optical and near-infrared fluxes are measured by Bond et al. (2009). The three components represent the photosphere, the hot dust and the warm dust. The progenitor SED is shown for comparison (Figures from Prieto et al. 2009)

.

arise from dust formed after the explosion, as proposed by Botticella et al. (2009) for SN2008S. Indeed, its radius of ∼67 AU combined with the time passed after the first detection of the transient suggest an expansion velocity of ∼1000 km s^{-1}, compatible with the velocities measured from optical spectra by Humphreys et al. (2011) and Berger et al. (2009). It is unlikely that the second component comes from preexisting dust: assuming a sublimation temperature of 1500 K for the dust grains, Prieto et al. (2009) find that the dust-free cavity generated by the explosion ranges from 80 to 250 AU, depending on the emissivity law assumed, hence supporting the new dust formation scenario. On the other hand, the third component lies at ∼515 AU, well outside the dust-free cavity: to reach such distance with a constant expansion the ejecta would need a velocity of ∼8000 km s^{-1}, much larger than velocities inferred from optical spectral lines. Therefore the third component must originate from preexisting dust, warmed up but not destroyed

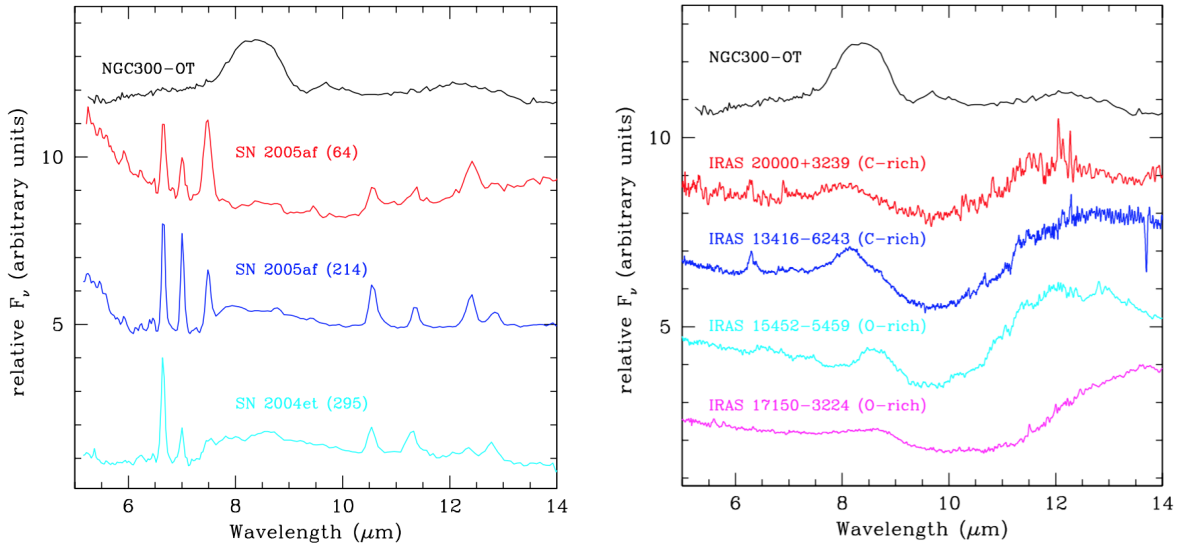

Figure 21: Left: mid-infrared spectrum of NGC300OT, after subtraction of the continuum, along with three spectra of SN IIP (their phase in days is reported in brackets). The lack of narrow components of Ni, Ar, Ne and Co is evident in NGC300OT. Right panel: the same spectrum is compared to those of Galactic proto-planetary nebulae. NGC300OT bears strong similarities to Carbon rich proto-planetary nebulae, as both display broad emission features at around 8 μm and 12 μm (Figures from Prieto et al. 2009)

by the outburst.

In Figure [21] the mid-infrared spectrum of NGC300OT is compared with typical spectra of SNIIP and proto-planetary nebulae. No fine-structure lines of Fe peak elements are visible in the spectrum. This proves that the dust is not primarily heated by the radioactive decay of ^{56}Ni and ^{56}Co, setting NGC300OT apart from classical SN IIP (Figure [21], left panel). However, this result does not rule out a terminal explosion, since it is consistent with the low ^{56}Ni mass production measured by Botticella et al. (2009) for SN2008S, as well as the low ^{56}Ni predicted by Wanajo et al. (2009) for EC-SNe. The similarities between NGC300OT and the carbon rich spectra of proto-planetary nebulae as well as the lack of typical silicates features indicate that the composition of the dust surrounding the transient is likely dominated by carbon (Figure [21], right panel).

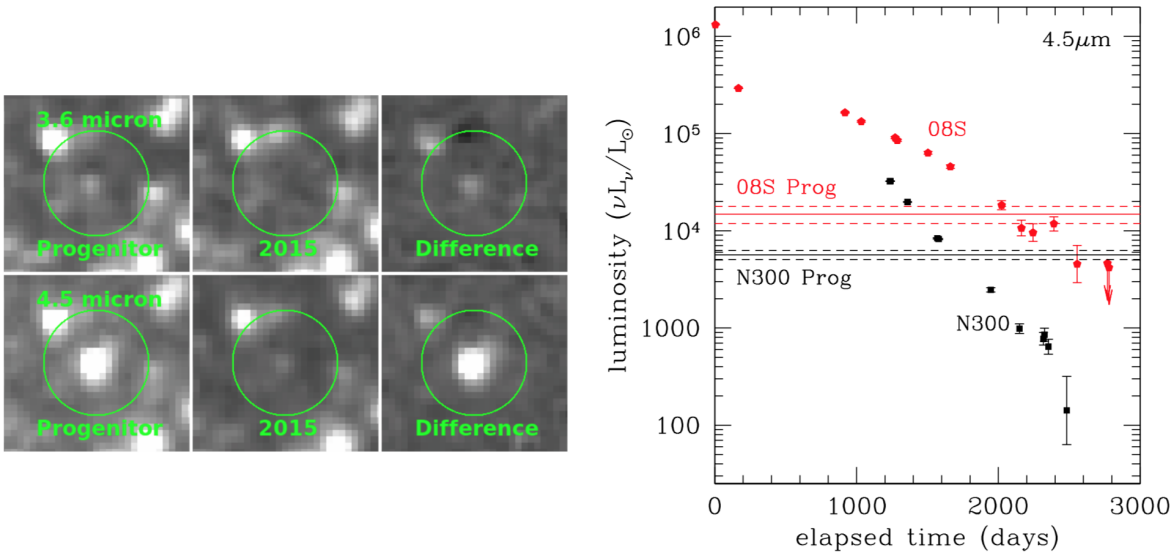

Figure 22: Left panel: Spitzer images of the NGC300OT progenitor and the transient observed in 2015, seven years after maximum. Green circles are 5" large. The difference between the two epochs show that the transient is now much fainter than the progenitor at both 3.6 and 4.5 μm. On the right, light curves at 4.5 μm for SN2008S (red pentagons) and NGC300OT (black squares). The luminosity of the progenitors is shown as a solid line, with 1σ uncertainties shown as dashed lines. Both objects are well below their progenitor luminosity (Figures from Adams et al. 2016).

2.5 Late Time Imaging of the Progenitor Sites

Adams et al. (2016) have continued monitoring the two prototypes of ILRT using HST, Spitzer, LBT, the Chandra X-rays observatory and the Magellan Telescope. The X-ray observations of SN2008S on 2012 May 21 do not identify a counterpart to the transient. Likewise, 4 years after the first detection, only upper limits can be measured in the optical and near infrared bands. Conversely, the investigation with Spitzer has produced light curves for both NGC300OT and SN2008S at 3.6 and 4.5 μm, showing that the two transients are now more than 15 times fainter than their quiescent progenitors in the mid-infrared (Figure [22]). This constrain is significant, and favours the scenario in which ILRT are the terminal explosions of the progenitor stars, leaving behind a compact remnant (likely a neutron star). However, it is still possible that the progenitors survived and are now being obscured by dust formed in the ejecta, as described in section [2.4]. Such dusty shell has an optical depth that decreases with time, as the grains are geometrically

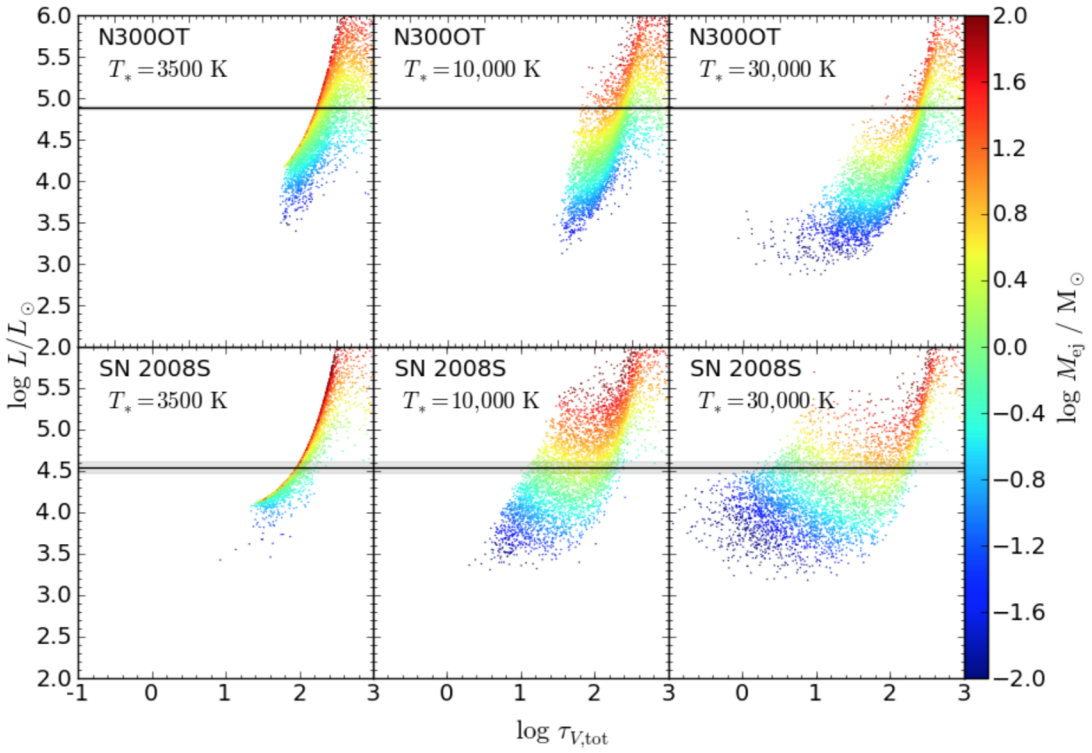

Figure 23: Monte Carlo results for the luminosity of the surviving star and optical depth of the dust shell. Three different temperatures are chosen for the obscured star: $T_* = 3500$, 10000 and 30000 K. The top row is relative to NGC300OT, while the bottom row represents SN2008S. Progenitors luminosities and relative 1σ uncertainties are reported for comparison as horizontal lines and gray shading. The points are colored depending on the mass ejected, calculated from equation [1] and assuming $\kappa = 100$ cm^{2}g^{-1} (Figure from Adams et al. 2016).

diluted with the expansion of the material:

$$\tau(t) = \frac{M_{ej}\kappa}{4\pi v_e^2 t^2} \tag{1}$$

where τ is the optical depth, t is time, M_{ej} is the ejected mass, v_e is the expansion velocity of the dusty shell and κ is the opacity. Using a Markov Chain Monte Carlo wrapper around the radiative transfer code DUSTY, Adams et al. (2016) present several possible surviving systems, depending on the luminosity of the star and on the optical depth of the obscuring dust. Figure [23] reports three different temperature scenarios for the surviving star: T_*

= 3500 K, compatible with an AGB star similar to the progenitors of the transients, $T_* = 10000$ K, consistent with a star on a blue loop as suggested by Humphreys et al. (2011), and finally $T_* = 30000$ K. If the surviving stars present similar temperatures and luminosities to the progenitors (Figure [23], left panels), the sources observed by Adams et al. (2016) must be obscured by a dust shell with $\tau > 100$ for NGC300OT and $\tau > 10$ for SN2008S. If the surviving stars are significantly fainter than the progenitors, lower optical depths are allowed. The lower right panel of Figure [23] shows, for SN2008S, a very hot ($T_* = 30000$ K) and unobscured ($\tau \sim 0$) surviving star with the luminosity of the progenitor. With $T_* > 45000$ K it is possible to obtain the same result for NGC300OT. However, there are lower limits to the optical depth inferred from Kochanek (2011) that set the condition $\tau > 15$, not allowing the existence of a hot surviving star with the progenitor luminosity. Despite being physically consistent, most of these models require an ejected mass > 1 $M_\odot$, and it is still unclear whether stars with M $\sim$10 $M_\odot$ can withstand such a large, non-teminal mass loss in a short amount of time . The most promising explanation remains therefore a terminal explosion, where the late mid-infrared luminosity is provided by the interaction between the ejecta and the CSM (Kochanek 2011) or radioactive decay (Botticella et al. 2009). Future monitoring in the mid-infrared may solve the residual uncertainties on the nature of ILRT: if their fluxes keep decreasing, the theory of a surviving star enshrouded by dust will require increasingly unreasonable ejected mass to explain the observations, leaving room only for a terminal SN explosion.

3 Data Reduction

Images of the transient were obtained through the observations of several telescopes over 18 months. The list of telescopes and instruments used, along with their main features, is reported in Table [1]. A typical example of an early phase image, with the identification of our target, is reported in Figure [24]. Pre-reduction steps of the imaging frames are performed through standard IRAF tasks: the frames are trimmed to keep only the relevant portion of the images, then master-bias and master-flat images are obtained respectively running the tasks ZEROCOMBINE and FLATCOMBINE. Flat and bias frames are combined through median instead of the average to properly remove the contribution from outliers.

3.1 Photometry with SNOoPY

Instrumental magnitudes and subsequent calibration are obtained through SNOoPY (SuperNOva PhotometrY Cappellaro (2014)), a dedicated pipeline designed for PSF fitting of multi-wavelenght data acquired from different instruments and telescopes. SNOoPY consists in a series of Python scripts calling IRAF standard tasks through PYRAF Tartaglia (2015). Main parameters of different instruments are recorded in a file called snoopy.default, which has been updated with the specifics of the different telescopes: fundamental instrument features are the RON, GAIN and scale of the telescope, as well as the filters used. Other fundamental quantities, such as the Modified Julian Date (MJD), the airmass affecting the observation, the exposition time or the coordinates of the observed field are found in the header of each image. The seeing is measured by selecting non-saturated stars through the task ECSEEING, which evaluates their mean Full Width at Half Maximum (FWHM). All the images are then astrometrized with the task ECASTRO by identifying some of the stars in the observed field with the stars available in the USNO-A2.0 catalogue (Figure [25]).

The subsequent step was to determine a model Point Spread Function (PSF) in each frame. To do this, isolated and unsaturated stars (Figure [26]) were manually selected and their profiles were averaged through the task ECPSF. Stars that were saturated or in crowded environments were not taken into account to compute the PSF model; however they still proved useful, as SNOoPY records instrumental magnitudes obtained from aperture photometry of all stars considered, as well as their positions. These pieces of information were fundamental when computing the subsequent calibration.

Finally, the PSF model is fit at the transient position: the task ECSNFIT allows

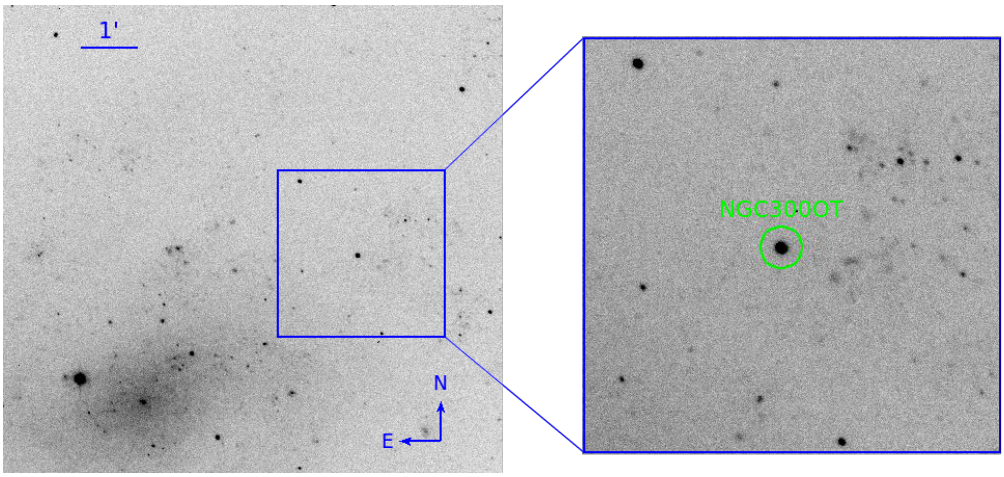

Figure 24: Indentification of the transient NGC300OT on an r-band image taken with the Swope Telescope on 2008 June 27. On the lower left of the first panel it is possible to see the galaxy NGC 300.

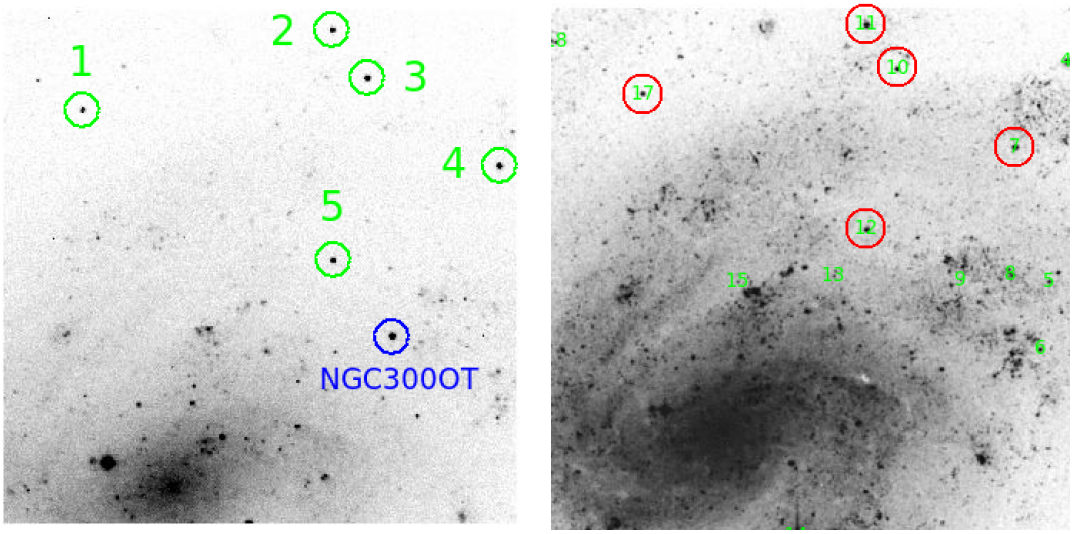

Figure 25: Left panel: Swope image of NGC300OT taken with an r filter on 2008 May 30. Right panel: USNO-A2 catalogue centered on the same coordinates. The conversion from pixel to physical units is obtained matching some of the observed stars (circled in green on the left panel) with the corresponding stars in USNO-A2 catalogue (circled in red on the right panel). Note the presence of the bright transient highlighted in blue in the Swope image, which is obviously missing in the reference catalogue.

Telescope	Diam	Location	Instrument	Scale	Filters
PROMPT	1.3 m	CTIO	Apogee	0.585	U,B,V,R,I; g,r,i,z
Swope	1 m	LCO	SITe#3	0.435	B,V and u,g,r,i,z
Gemini South	8.1 m	GO	GMOS-S	0.146	r,i,z
Magellan Clay	6.5 m	LCO	LDSS3-Two	0.371	g,r,i,z
NTT	3.58 m	La Silla	EFOSC, SOFI	0.24, 0.288	U,B,V,R,I,J,H,K
REM	0.6 m	La Silla	ROSS, REMIR	0.575, 1.22	V,R,I,J,H,K

Table 1: List of telescopes used for photometry. The diameter reported is that of the primary mirror of the telescope. The scale is in units of arcsec pixel^{-1}.
NTT = New Technology Telescope, REM = Rapid Eye Mount
CTIO = Cerro Tololo Inter-American Observatory, LCO = Las Campanas Observatory, GO = Gemini Observatory

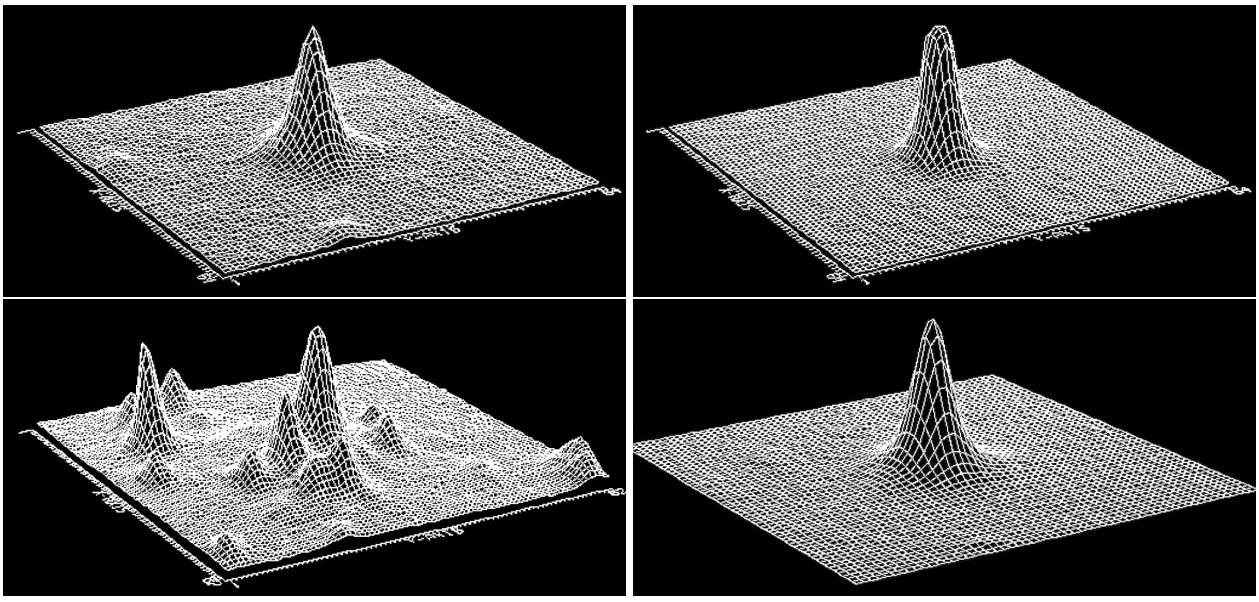

Figure 26: Examples of standard and problematic stellar profiles taken from a Magellan image, g band. From top left to bottom right we show an isolated, unsaturated star, a saturated star, a crowded environment and an example of a mediated profile. When the situation is less obvious it is possible to quantitatively compare the Moffat fit result with the average result for the stars in the same image. Five stars are usually enough to build a good PSF model.

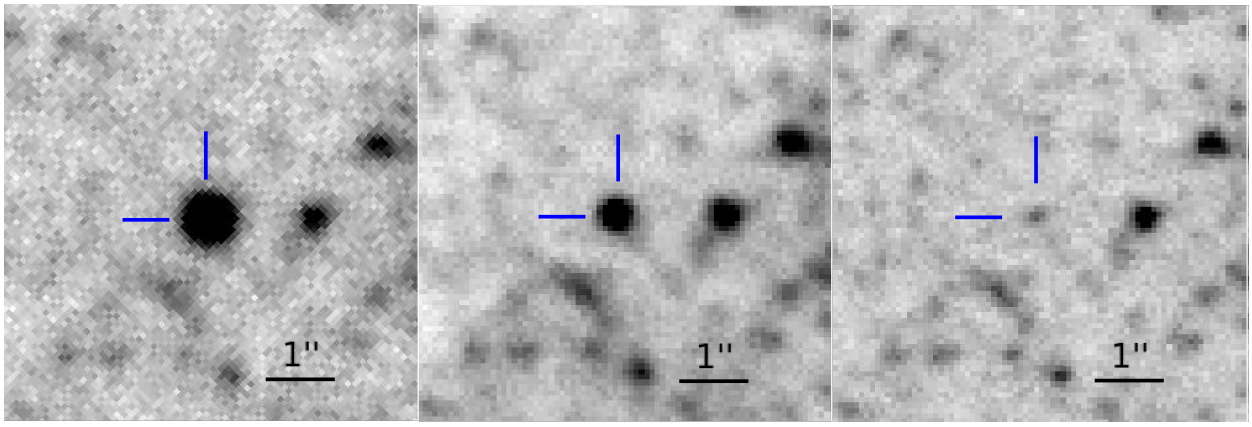

Figure 27: NGC300OT observed by the Gemini South Observatory at three different epochs in r band: 7-1-2009, 19-5-2009, 26-8-2009. Note the "fast" decline in luminosity of the target. In the right panel is shown our last detection of the object in r band. Subsequent observations, performed in November 2009, can only give upper limits to the luminosity, since the object is no longer clearly visible.

to fit the local analytic PSF to the target, evaluating the background in an annulus defined by the user (by default between 2 and 3 times the FWHM of the target) while subtracting the transient's flux contribution. This measure of the background is then used along with the analytic PSF to fit the object profile and measure its instrumental magnitude. The error on this procedure was obtained through ECARTERR, which places many artificially created star close to the target, with magnitudes and profiles coincident with that inferred for the object. The dispersion of the artificial stars' instrumental magnitudes gives the root mean square (rms) associated with the instrumental magnitude of the transient, which must be summed in quadrature with the PSF fitting error given by DAOPHOT. When the signal to noise ratio is low (≤ 2.5) the target becomes difficult to be discriminated from the background. A dedicated task called ECLIMIT estimates an upper limit to the luminosity of the object. This feature becomes particularly useful during the late stages, when the transient fades significantly (Figure [27]).

In order to calibrate the instrumental magnitudes, it is necessary to build a catalogue of standard stars. This can be done using the task ECZEROPOINT, which retrieves magnitudes and coordinates of the reference stars inside the field of a given image from the sloan, apass, panstarrs or skymapper catalogue. A large number or reference stars are contained in the Prompt field (9.9' x 9.9'). The magnitudes and coordinates of a few additional stars, located in a more peripheral position from NGC300OT, have been manually added to our reference catalogue. The calibration is performed by solving the following equations for each star, in

each band:

$$m_{0,\lambda} - m_{\lambda} = a_{\lambda} + b_{\lambda}(colour) \tag{2}$$

where m_{λ} is the instrumental magnitude, $m_{0,\lambda}$ is the calibrated magnitude, a_{λ} is the Zero Point (ZP) and b_{λ} is the Colour Term (CT). Both ZPs and CTs can usually be found among the instrument information, or they can be retrieved through a least square solution knowing the magnitudes of the reference stars. While the Colour Term for a defined instrumental configuration remains roughly constant, the Zero Point can change significantly even during the same night. To account for this, the task ECNIGHTCAL compares the measured magnitudes of the reference stars with those of the catalogue. The difference between the observed and the catologual magnitudes gives the zero corrections in each filter for each night (Figure [28]).

Finally, the task ECSNCAL receives as input the instrumental magnitudes, CT and ZP corrections for individual nights and produces the calibrated apparent magnitudes as output. The results in different bands are ready to be displayed as light curves.

3.2 Spectroscopy

We collected 22 optical spectra, spanning a period of 8 months from the discovery of the transient, and 2 NIR spectra, taken on 2008 October 08 and 2009 October 12, respectively. The log of the observations, along with information about the instruments used, is reported in Table [2]. The reduction of the spectra is obtained using standard IRAF tasks contained in the CTIOSLIT package. We extract monodimensional spectra with the task APALL, performing an optimized extraction along the dispersion axis, after subtracting the sky lines. The wavelength calibration is achieved through the task IDENTIFY, with which we compare the extracted 1d-spectrum with He, Ne or Ar lamps spectra taken with the same instrumental configuration. The resolution of the spectra is measured through the mean FWHM of unblended sky lines. The flux calibration is performed using the observation of a standard star. This procedure has an accuracy of typically 10-15%, limited by the sky conditions and the errors in positioning the slit on the target. We subsequently check the resulting calibration against our multi-band photometric data. In particular, we use the task CALCPHOT, contained in the package STSDAS, to obtain the magnitude in a specific band for each spectrum. The difference between the magnitude obtained through the photometry and the

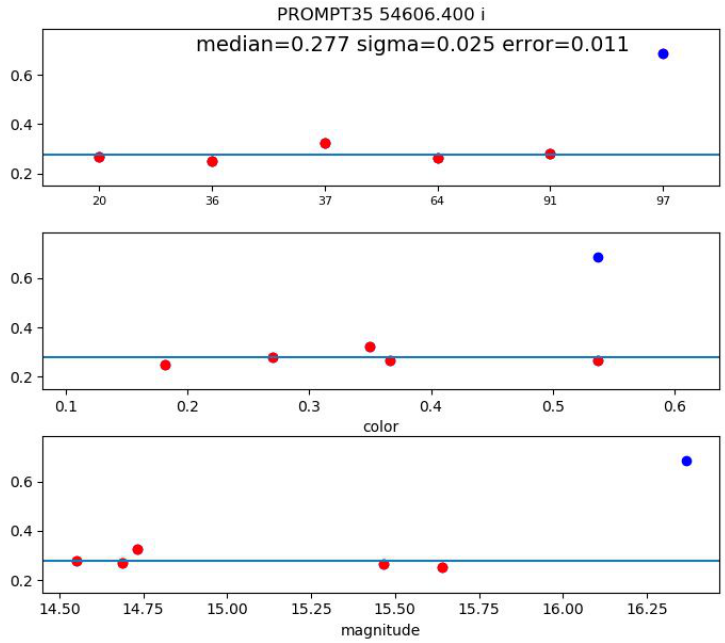

Figure 28: Example of Zero Point calibration for a non-photometric night. On the Y axis is shown the zero difference between measured and catalogue magnitudes, which will be adopted as ZP correction. The blue point has been discarded due to high discrepancy with other data. In general, faint reference stars are less reliable than bright ones.

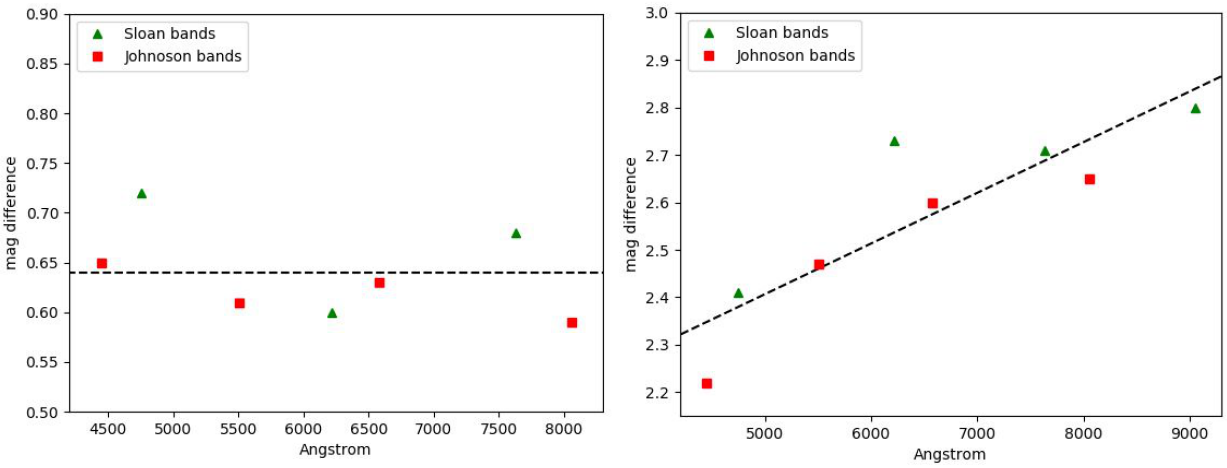

Figure 29: Flux calibration for the spectra taken on 2008 June 13 and 2008 May 16, respectively. For the first spectrum the correction factor is simply a constant, while for the second one a wavelength dependent parameter is applied.

Date	Telescope+Instrument	Grism	Range (Å)	Res (Å)	Exp. time (s)
2008-05-16	BMagellan+IMACSshort	g200	4000-10500	6	100x2
2008-05-30	DuPont+B&C	g300	3500-9600	8	300
2008-06-04	DuPont+B&C	g300	3500-9600	8	300
2008-06-06	NTT+EFOSC	gm3-gm5	3300-9200	B11 R15	1460x2
2008-06-11	CMagellan+LDSS3	-	3700-9800	4	300x3
2008-06-13	NTT+EFOSC	gm3-gm5	3300-9200	B11 R15	1460x2
2008-06-15	NTT+EFOSC	gm3-gm5	3300-9200	B11 R15	1460x2
2008-06-16	BMagellan+IMACSlong	g300	3700-7900	4	300x3
2008-07-01	VLT+FORS	300V	3300-9200	11	1800
2008-07-02	VLT+UVES	SHP700+HER_5	3400-8000	B0.12 R0.36	1500x6
2008-07-05	NTT+EFOSC	gm3-gm5	3300-9200	B11 R15	1460x2
2008-07-08	VLT+FORS	300V	3300-9200	11	2160
2008-07-15	NTT+EFOSC	gm3-gm5	3300-9200	B11 R15	1460x2
2008-07-23	CTIO4m+R-CSpec	KPGL3-1	4000-7600	5	720
2008-07-24	CTIO4m+R-CSpec	KPGL3-1	4000-7600	5	1200
2008-07-25	CTIO4m+R-CSpec	KPGL3-1	4000-7600	5	1200
2008-08-05	NTT+EFOSC	gm3-gm5	3300-9200	B11 R15	1460x2
2008-09-17	CMagellan+LDSS3	VPH-All	3700-9400	6	900
2008-10-02	Palomar200i+DBSP	300/3990+158/7500	3300-10300	B11 R16	1800x2
2008-10-08	TNG+NICS	IJ+HK	8700-24700	IJ16 HK30	–
2008-10-14	WHT+ISIS	R158R+R300B	3400-10200	B4 R6	600x3
2009-01-07	CMagellan+LDSS3	VPH-All	4000-8000	6	1580
2009-01-21	CMagellan+LDSS3	VPH-All	4000-8000	6	1800
2009-10-12	VLT+X-Shooter	-	10100-24400	3.6	300

Table 2: Log of spectroscopic observations along with main features of the instruments used. FORS spectra were taken from Patat et al. (2010).

magnitude measured in the spectra yields the scaling factor, as expressed by the Pogson law:

$$\frac{I_\lambda}{I_{\lambda,0}} = 10^{-0.4(M_{\lambda,phot} - M_{\lambda,spec})} \tag{3}$$

where I_0 and I are the fluxes before and after the correction, and M is the magnitude, either obtained through photometry or through spectroscopy. All quantities are wavelength dependent, hence the subscript λ. We observe two cases, in our spectra: either the correction factor I / I_0 does not vary with λ, or there is a linear dependence with λ. In the latter case, a linear function was applied to flux-correct the spectrum. An example of both instances is shown in Figure [29].

4 Photometry

NGC300OT was intensively studied, with extensive photometric and spectroscopic data sets published by other authors, as described in Section [2]. In particular, Humphreys et al. (2011) and Bond et al. (2009) provided optical and NIR photometric observations from 2008 May 14 to 2009 June 1, and optical spectra from 2008 May 15 to 2009 January 20. They also obtained one NIR-spectrum, on 2009 July 19, but with low resolution and modest S/N. Berger et al. (2009) provided high resolution spectra from May to August 2008, and Adams et al. (2016) obtained very late IR photometry, between 2010 and 2015. In this context, our photometric data provide new coverage of the transient during the late phases, in particular until 2009 November 16. NIR observations span even further, with the latest measures taken in K-band on 2010 January 23. Our optical spectra provide additional sampling to the existing literature, especially during the early phases in June and July 2008. Finally, we present for the first time two NIR spectra with good S/N for NGC300OT.

4.1 Optical Ligh Curves

The optical follow up campaign started on 2008 May 16 and was stopped on 2009 November 16. The apparent light curves are shown in figure [30]. Due to the lack of tight constraints on the explosion epoch, we adopt the discovery date, 2008 April 22, as reference epoch. The actual peak was not observed, as the object was behind the sun: thus we refer to our first, brightest observations as the "peak luminosity". Three main phases can be identified from the light curve shapes. Up to $\sim$ 55 days the luminosity of the transient declines very slowly, with the decline rate (γ_1) being lower for the red bands (eg, *r*R*i*I). This pseudo-plateau phase is followed by a fast decline (γ_2) between 55 and 155 days after explosion epoch, with blue bands (eg, B*g*V) declining faster. Although SN 2008S did not show a pseudo-plateau, the magnitude decrease during this phase is remarkably similar to that of NGC300OT (Botticella et al. 2009). On the other hand, the ILRT AT 2017be shows a pseudo-plateau phase followed by a much slower decline ($\sim$ 2 mag/100days) compared to NGC300OT (Cai et al. 2018). After 155 days, a slower linear decline phase (γ_3) starts. The decline rate values are reported in Table [3], along with the absolute magnitudes at peak for each band, calculated as described in Section [4.4]. NGC300OT at peak appears to be $\sim$ 2 mag fainter in R-band than SN 2008S. In order to compare the *ugriz* magnitudes with UBVRI magnitudes, it is necessary to convert both set of data in the same magnitude scale, scaling by the following zero point values:

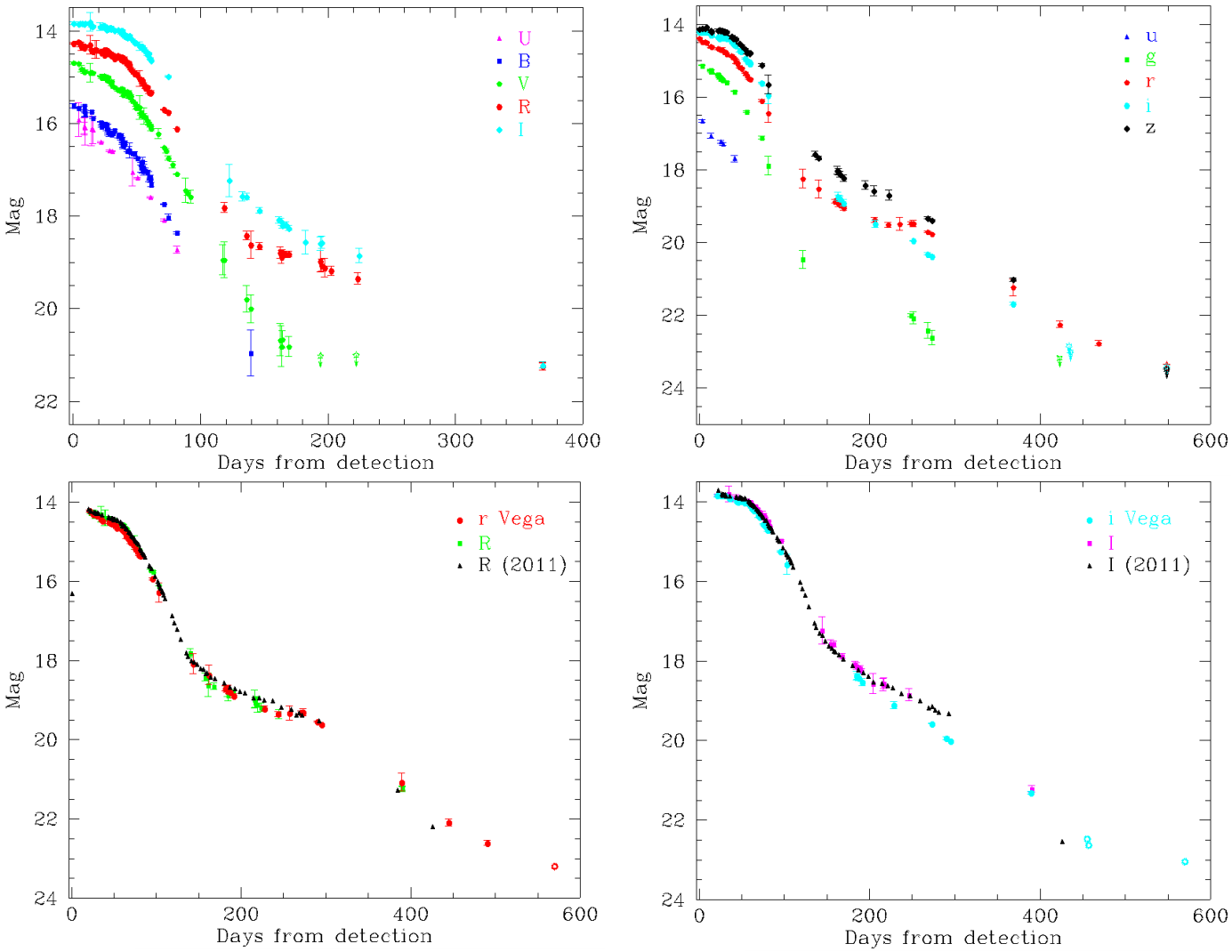

Figure 30: Upper panels: multi-band optical light curves of NGC300OT. The UBVRI magnitudes are calibrated to the Vega magnitude scale, while the sloan *ugriz* magnitudes are calibrated using the AB magnitude scale. Empty symbols represent upper mangnitude limits. Lower left: Sloan r and R-band magnitudes from this work, compared with the R-band magnitudes from Humphreys et al. (2011). Lower right: the same comparison is shown for *i* (Vega) and I bands. The Sloan r and i-magnitudes are scaled to the Vega system.

Filter	M_{max}	γ_1 (mag/100days)	γ_2 (mag/100days)	γ_3 (mag/100days)
U	-10.76 ± 0.36	2.38 ± 0.47	–	–
B	-11.03 ± 0.05	1.98 ± 0.16	4.5 ± 0.5	–
V	-11.90 ± 0.02	1.11 ± 0.10	4.41 ± 0.35	–
R	-12.27 ± 0.02	0.72 ± 0.10	3.95 ± 0.1	1.18 ± 0.03
I	-12.66 ± 0.03	0.45 ± 0.08	3.75 ± 0.3	1.51 ± 0.05
u	-10.94 ± 0.04	2.57 ± 0.44	–	–
g	-11.44 ± 0.02	1.69 ± 0.11	5.74 ± 0.3	1.34 ± 0.18
r	-12.36 ± 0.03	1.14 ± 0.08	4.06 ± 0.3	1.21 ± 0.05 (a)
i	-12.70 ± 0.03	0.64 ± 0.10	3.38 ± 0.3	1.38 ± 0.07
z	-12.91 ± 0.03	0.24 ± 0.09	3.32 ± 0.07	1.41 ± 0.03

Table 3: Peak magnitudes and magnitude decline rates during the three different phases for the optical bands.
(a) For the *r*-band, the latest phase can be separated into two periods: from 155 to 240 days the decline is shallower (0.85 ± 0.09 mag/100days), and in this period the *r*-band becomes more luminous than the *i*-band. After 240 days the linear decline (1.37 ± 0.14 mag/100days) becomes compatible with that of the *i* and *z*-bands.

Band	m_{AB} - m_{Vega}
u	0.91
g	-0.08
r	0.16
i	0.37
z	0.54

The UBVRI and *ugriz* magnitudes are consistent with the ones published by Humphreys et al. (2011) (Figure [30]), except for the *i* band. After 200 days from discovery, we note a systematic discrepancy between *i* and I bands. This can be explained through the different width of the Johnson Cousins and Sloan transmission filters, that cover different features of the spectrum of NGC300OT. The response curves of the standard UBVRI and *ugriz* filters are shown in (Figure [31]), along with a spectrum of the transient. In Table [4] we report the differences between the *i* and I magnitudes obtained from the photometry and from the spectrophotometry. There is a mismatch in the epochs in which photometry and spectra were taken, preventing a coeval comparison, but there is a clear

Date	$(i\text{-}I)_{phot}$	$(i\text{-}I)_{spec}$
2008-05-16	0.38 ± 0.03	0.44
2008-05-30	0.39 ± 0.02	0.47
2008-06-04	0.42 ± 0.03	0.51
2008-06-11	0.43 ± 0.02	0.48
2008-06-13	0.41 ± 0.01	0.50
2008-06-16	0.42 ± 0.03	0.51
2008-07-01	0.47 ± 0.06	0.49
2008-07-05	0.48 ± 0.02	0.54
2008-07-08	0.50 ± 0.03	0.54
2008-07-10	0.55 ± 0.03	0.49
2008-07-15	0.55 ± 0.02	0.57
2008-08-05	——	0.64
2008-09-17	——	0.8
2008-10-02	——	0.84
2008-10-14	——	0.85
2008-10-26	0.52 ± 0.11	——
2008-11-02	0.60 ± 0.09	——
2008-12-09	0.79 ± 0.10	——

Table 4: Difference between Sloan *i*-band (ABmag) and Johnson Cousins I-band (Vega mag) magnitudes. Data in the second and third column are obtained from photometry and spectrophotometry, respectively. The large difference observed in the *i* and I-bands is explained with the flux contribution of the strong Ca II NIR triplet, which is contained in the Johnson Cousins I passband but not in the Sloan *i* passband.

trend where both sets of data systematically increase the magnitude gap between *i* and I-band. This suggests that the origin of the discrepancy lies in the different wavelength window of the filters used.

4.2 NIR Light Curves

NIR observations are crucial for ILRTs, since the contribution of these bands to the total luminosity of the transient is significant at all epochs. Our late time sampling (>400 days) is coherent with a linear decline in magnitude, and the early time observations are overall consistent with the ones published in the liter-

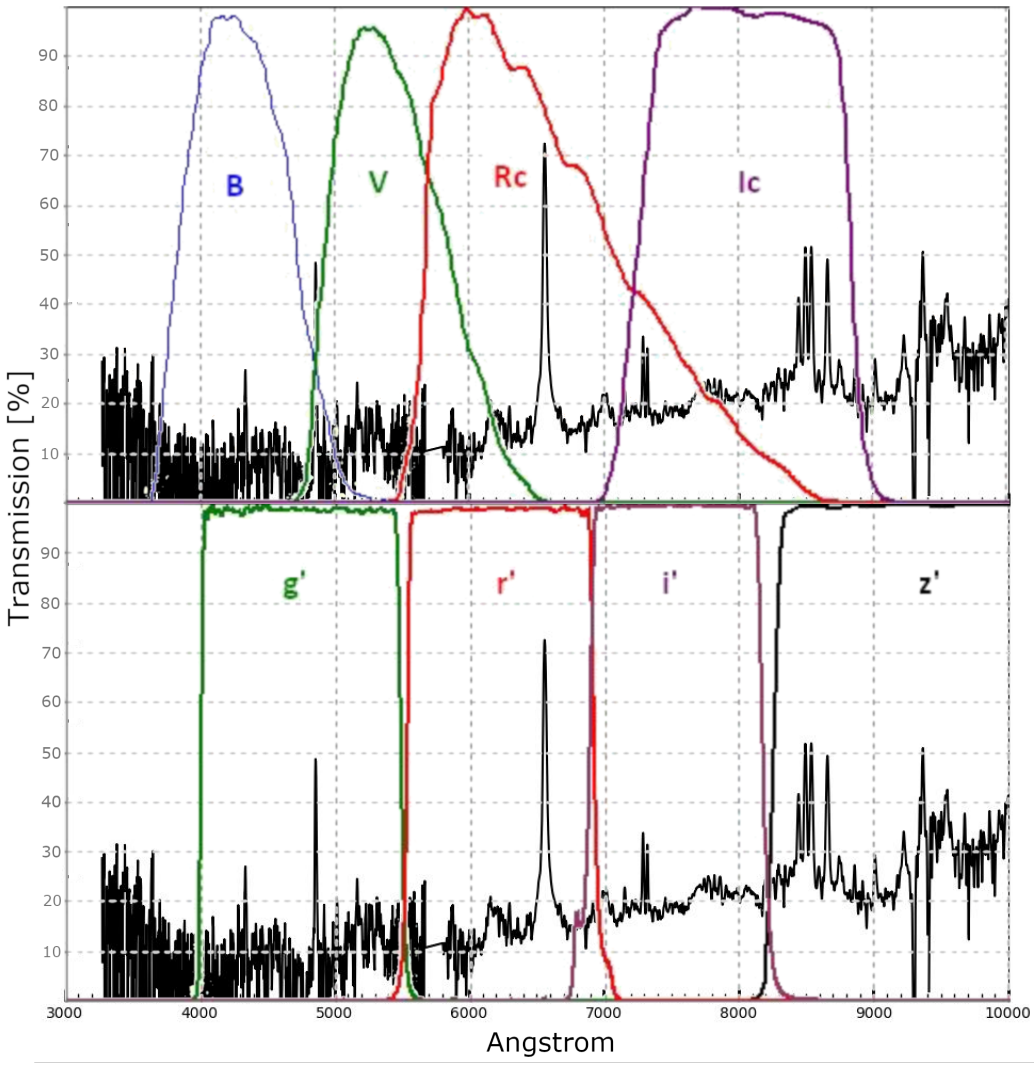

Figure 31: Sloan and Johnson bands overlapped to a spectrum of NGC300OT (2008 October 14), plotted in logarithmic scale. In particular, the I band covers the Ca II NIR triplet feature (around 8500 Å), while the *i* band cuts it off completely. This leads to a significant difference in magnitude when this feature becomes more relevant than the underlying continuum.

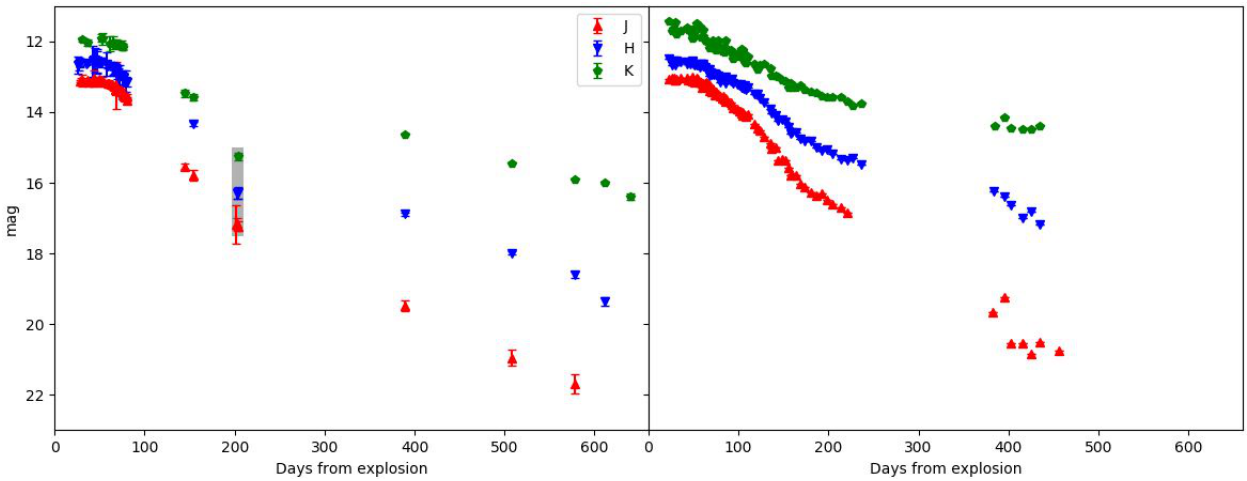

Figure 32: Left panel: our J, H and K-band light curves of NGC300OT. Right panel: NIR light curves published by Humphreys et al. (2011). The epoch (around 200 days) with discrepant photometry between the two data sets obtained is highlighted with a grey patch.

Filter	M_{max}	γ_1 (mag/100days)	γ_2 (mag/100days)	γ_3 (mag/100days)
J	-13.34 ± 0.04	0.12 ± 0.11	2.78 ± 0.19	1.19 ± 0.04
H	-13.77 ± 0.23	-0.18 ± 0.11	2.47 ± 0.26	1.05 ± 0.1
K	-14.49 ± 0.07	-0.33 ± 0.20	2.33 ± 0.16	0.66 ± 0.08

Table 5: NIR peak magnitudes and decline rates in three different phases.

ature (Humphreys et al. 2011). A notable exception, however, is the observation on 2008 November 14, which is systematically fainter in all three bands than Humphreys et al. (2011) photometry, in particular over 2 mag fainter in the K-band (Figure [32]). Our NIR data set was taken with the REM telescope up until 2008 November 14, while thereafter the observations were performed with SOFI at the New Technology Telescope (NTT). Both instruments mounted a K-short band filter, so the discrepancy is not due to the different spectral range observed. The zero point calibration performed with 2MASS standard stars appears reliable (Figures [33] and [34]). Since we do not see any clear reason to discard such observation, we perform the following analysis separately on the two data sets: the first one contains only our original, unpublished measures (OAPD set), while in the second one we replace our NIR measures between 139 (2008 September 26) and 295 days (2008 December 17) after explosion with those of Humphreys

Filter	γ_2 (mag/100days)	γ_2' (mag/100days)
J	2.78 ± 0.19	2.83 ± 0.1
H	2.47 ± 0.26	1.74 ± 0.21
K	2.33 ± 0.16	1.67 ± 0.16

Table 6: Comparison of the magnitude decline after the pseudo-plateau phase for OAPD (γ_2) and Humphreys (γ_2') data sets.

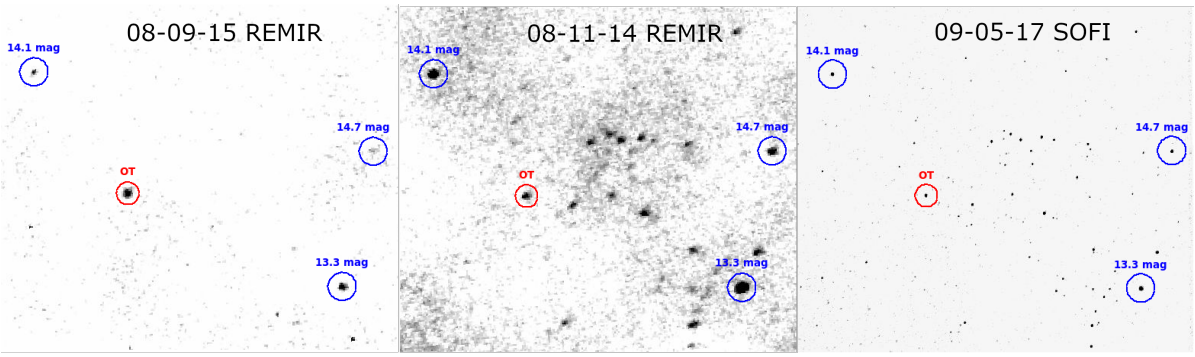

Figure 33: K-band images of NGC300OT at 144, 203 and 389 days after discovery. Local standard stars are included in the field for reference. Our reduction yields a magnitude of 15.2 mag for NGC300OT on 2008 November 14, and indeed the transient appears to be fainter than all the reference stars displayed.

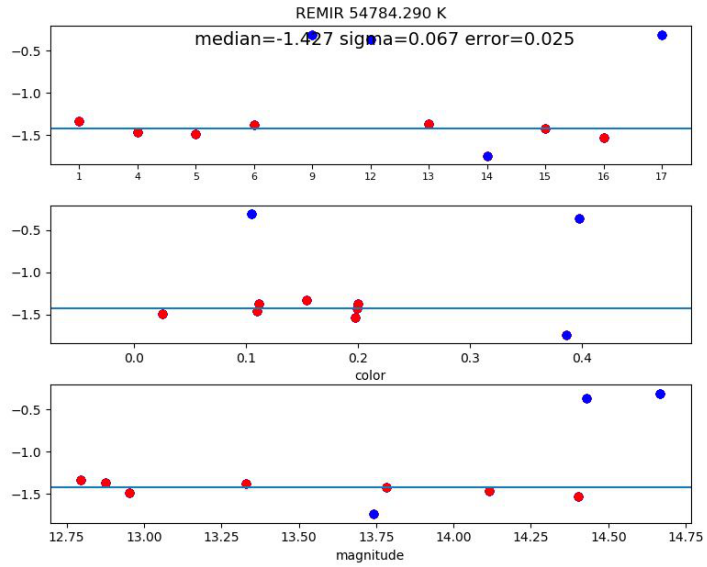

Figure 34: Zero point calibration for the K-band observation on 2008 November 14. After rejecting three outliers (indicated with blue points), the calibration is solid. The standard stars are retrieved from the 2MASS catalogue.

et al. (2011) (Humphreys set). The NIR light curves show a behaviour similar to the optical light curves (Table [5]): an early pseudo-plateau and a fast decline, followed by a shallower linear decline at late epochs. The Humphreys data set shows similar time scales to the optical light curves, with a pseudo-plateau lasting up to $\sim$ 60 days and a sharp decline ending roughly after day 160. For the OAPD set, however, the sharp decline lasts until day 200, and a significant rebrightening appears in the K-band, before the light curve settles back onto a linear decline (Table [6]).

4.3 Host Galaxy Distance and Reddening

The galaxy hosting the transient is the well-studied NGC 300, classified as SA(s)d by de Vaucouleurs et al. (1991). In the NASA/IPAC Extra-galactic Database (NED), a redshift of z = 0.000480 ± 0.00003 is reported along with 75 independent measures of the distance of NGC 300. Many of them are quite old estimates, hence we select 9 recent works, chosen among those with lowest uncertainty and prioritizing primary distance indicators such as Cepheids and the RGB tip, but including also measures done with Planetary Nebulae (PNLF) and Globular Clusters Luminosity Function (GCLF) (Table 7). The final value for the distance modulus is obtained through a weighted mean of these distance values, adopting their er-

Author (et al)	Year	Method	m-M (mag)	D (Mpc)
Gieren	2005	Cepheids	26.37 ± 0.07	1.88
Tully	2013	Cepheids	26.48 ± 0.06	1.98
Bhardway	2016	Cepheids	26.28 ± 0.05	1.80
Rizzi	2006	RGB Tip	26.36 ± 0.02	1.87
Dalcanton	2009	RGB Tip	26.53 ± 0.03	2.02
Jacobs	2009	RGB Tip	26.59 ± 0.06	2.08
Pena	2012	PNLF	26.29 ± 0.22	1.81
Julie	2006	GCLF	26.71 ± 0.14	2.20
Gogarten	2010	Red Clump	26.43 ± 0.09	1.93
Final Value			**26.42 ± 0.15**	**1.92**

Table 7: Distance estimates of NGC 300 from NED (see text for details).

rors as weights. The error associated to the final estimate is determined using the standard deviation of the data from the weighted mean. We follow this approach since the weighted mean error results unreasonably small and does not account for the observed scatter of the values. The Galactic reddening towards NGC 300 is determined from Schlafly & Finkbeiner (2011), providing a colour excess is E(B-V) = 0.0109 ± 0.0001 mag. The host galaxy reddening to the object is estimated from the equivalent width of the interstellar NaID lines in high resolution spectra, yielding E(B-V) = 0.05 ± 0.05 mag (Berger et al. 2009).

4.4 Absolute and Colour Light Curves

We obtain the absolute magnitudes from the apparent ones through the relation:

$$M_X = m_X - \mu - A_X \tag{4}$$

where M_X is the absolute magnitude in the X band, m_X is the apparent magnitude in X band, μ is the distance modulus and A_X is the absorption in the X band. The absorption in a generic X band is calculated starting from the reddening E(B-V) and applying the extinction laws from Cardelli et al. (1989). The resulting absolute and colour light curves are shown in Figure [35]. Except for the U-B colour, which remains roughly constant ($\sim$ 0.3 mag) during the observed period, all colours show different behaviours before and after the $\sim$100 days mark. During the first phase, B-V, V-R and R-I increase steadily (to 1.21 ± 0.03, 0.93 ± 0.05 and

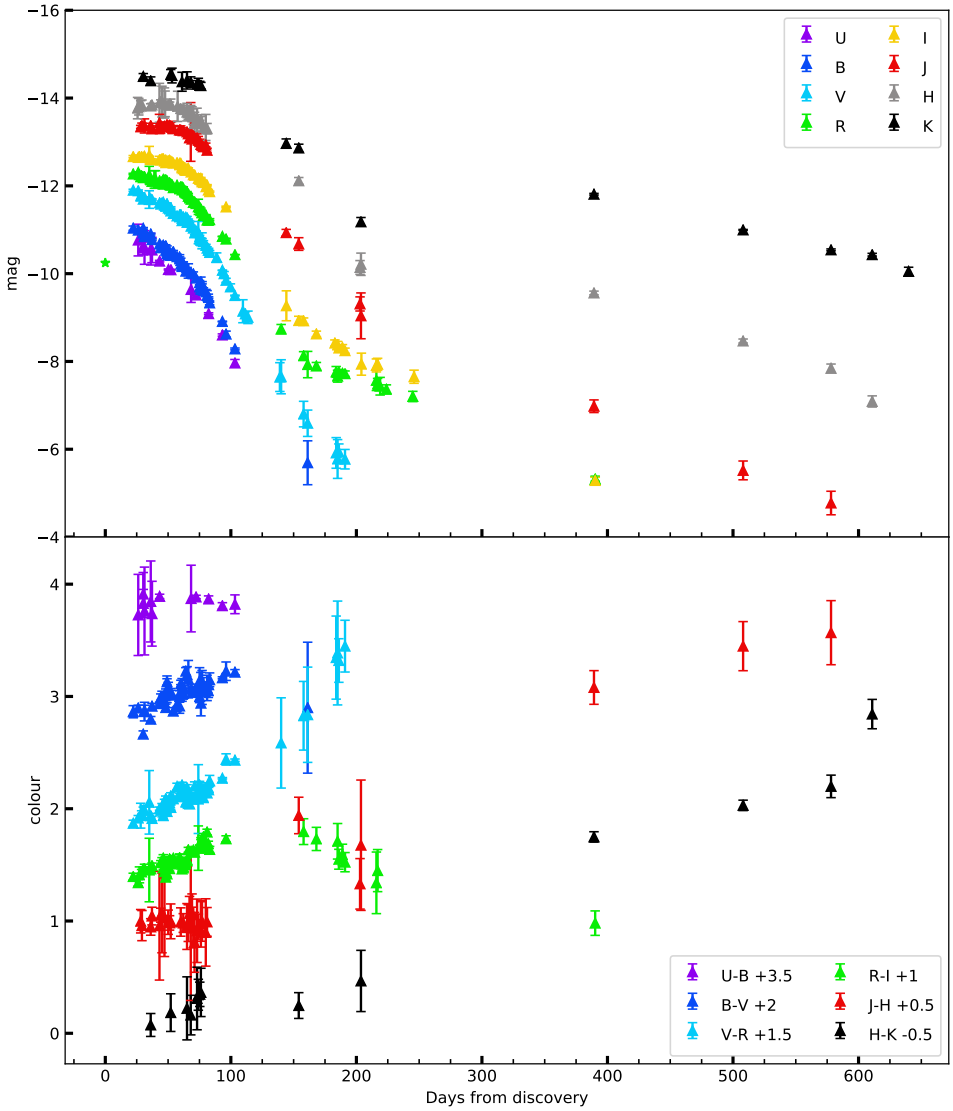

Figure 35: Absolute and colour light curves of NGC300OT. The star marker in the upper panel denotes the discovery of the object. Colour light curves are shifted by an arbitrary constant for clarity.

Transient	Class	μ	A_V	Reference
SN 2008S	ILRT	28.78 ± 0.08	~ 2.1	Botticella et al. (2009)
AT 2017be	ILRT	29.47 ± 0.15	0.28 ± 0.09	Cai et al. (2018)
AT 2017jfs	LRN	32.7 ± 0.15	0.07	Pastorello et al. (2019)
M31-LRN2015	LRN	24.43 ± 0.06	0.37 ± 0.18	Williams et al. (2015)
SN 2000ch	LBV	30.17 ± 0.56	0.04	Pastorello et al. (2010b)
SN 2005cs	SN IIP	29.26 ± 0.33	0.15	Pastorello et al. (2009)
SN 1999br	SN IIP	31.19	0.1	Pastorello et al. (2004)
SN 2005E	Ca-rich	32.66	0.10	Perets et al. (2010)
SN 2012hn	Ca-rich	32.14 ± 0.15	0.93	Valenti et al. (2014)
SN 2008ha	SN I	31.64	0.25	Valenti et al. (2009)

Table 8: Distance moduli and reddening values used to compare various transients (Gap Transients and faint SNEe) to NGC300OT.

0.73 ± 0.03 mag respectively). This can be interpreted as a cooling black body, which becomes progressively redder with time. After ~100 days the behaviour become more complex: V-R steepens, while B-V and R-I start decreasing. On the other hand, J-H remains roughly constant (~ 0.5 mag) during the time interval, while H-K displays a slow increase. During the second phase, both J-H and H-K show a fast increase, with the object becoming severely red around 600 days (3.0 ± 0.3 and 3.35 ± 0.15 mag respectively).

4.5 Comparison with Other Transients

In Figures [36] and [37] we compare the absolute and colour light curves of NGC300OT with other Gap Transients as well as faint SN explosions. The distance modulus and absorption in the V-band adopted for each transient are reported in Table [8], along with the reference paper. Among Gap Transients we choose two ILRT (SN 2008S, AT 2017be), two LRN (M31-LRN2015, AT 2017jfs) and one LBV outburst (SN 2000ch). Both the absolute light curves and the colour curves of the three ILRT appear homogeneous in their evolution, with NGC300OT being a fainter and redder twin of SN 2008S. The two LRN display a second peak in their light curves, as well as fast increasing B-V and R-I, separating them from the ILRT class. The erratic behaviour and bluer colours of the LBV SN 2000ch allow to discriminate this impostor from the other Gap Transients shown. In Figure

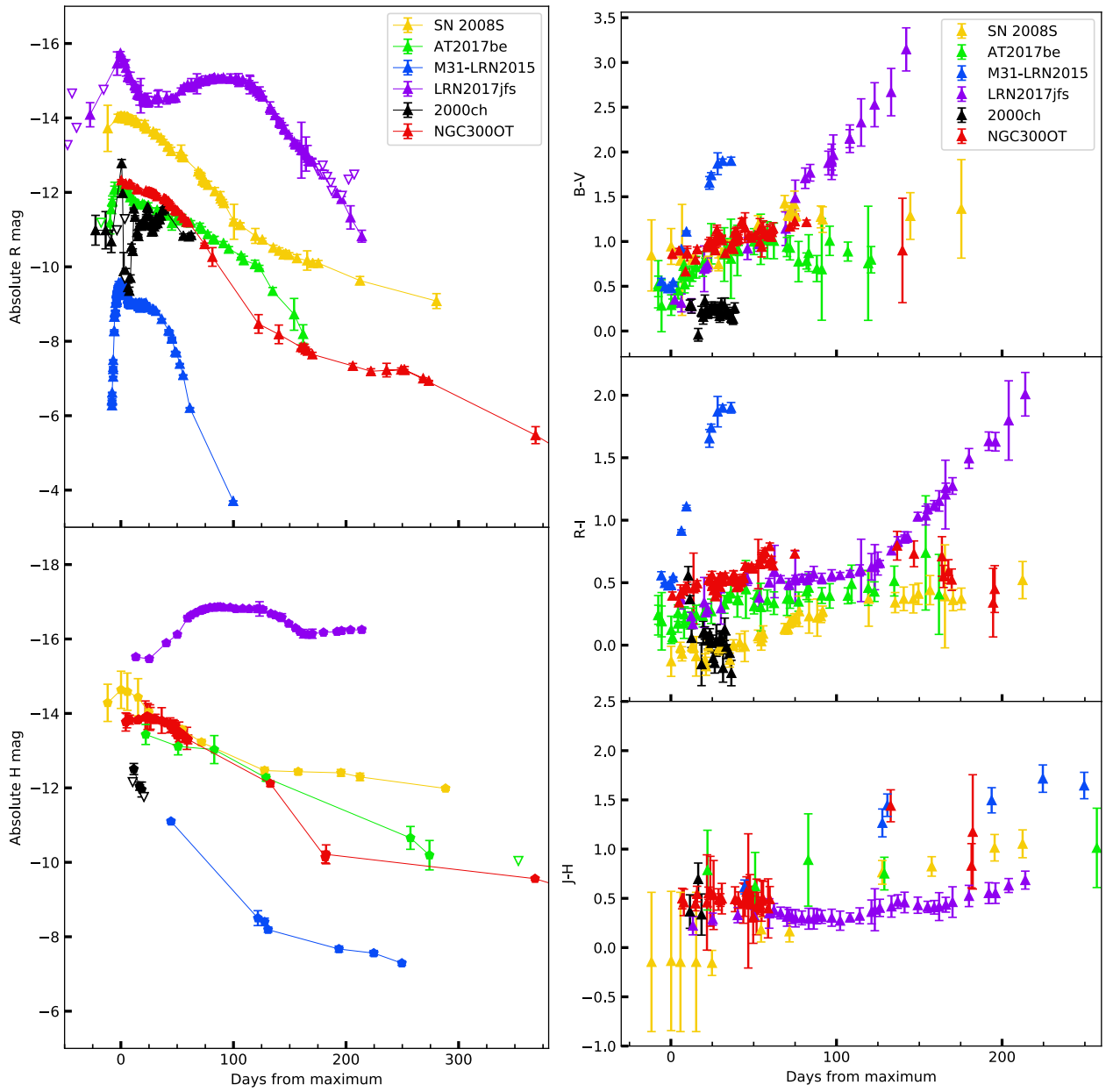

Figure 36: Left panels: R and H-band absolute light curves for several Gap Transients. In particular, SN 2008S (ILRT), AT2017be (ILRT), AT2017jfs (LRN), M31-LRN2015 (LRN) and SN 2000ch (LBV outburst). Right panels: B-V, R-I and J-H colours for the same objects.

[37] we display two faint SN IIP (SN 2005cs, SN 1999br), two Ca-rich transients (SN 2005E, SN 2012hn) and a faint SN Iax (SN 2008ha). Ca-rich transients are Type I SNe which lie on the bright end of the Gap (between -14 and -16.5 mag) and have spectra characterized by strong [Ca II] doublet emission (see Taubenberger (2017) for a review in the context of thermonuclear SNe). The decline of NGC300OT is definitely faster with respect to SN IIP, and the luminosity drop is not as abrupt. At the same time, the other SN I show a much narrower peak. Although without a perfect match, the colour evolution is more compatible with SN IIP than, for instance, with Ca-rich transients, which show a faster colour evolution at early phases.

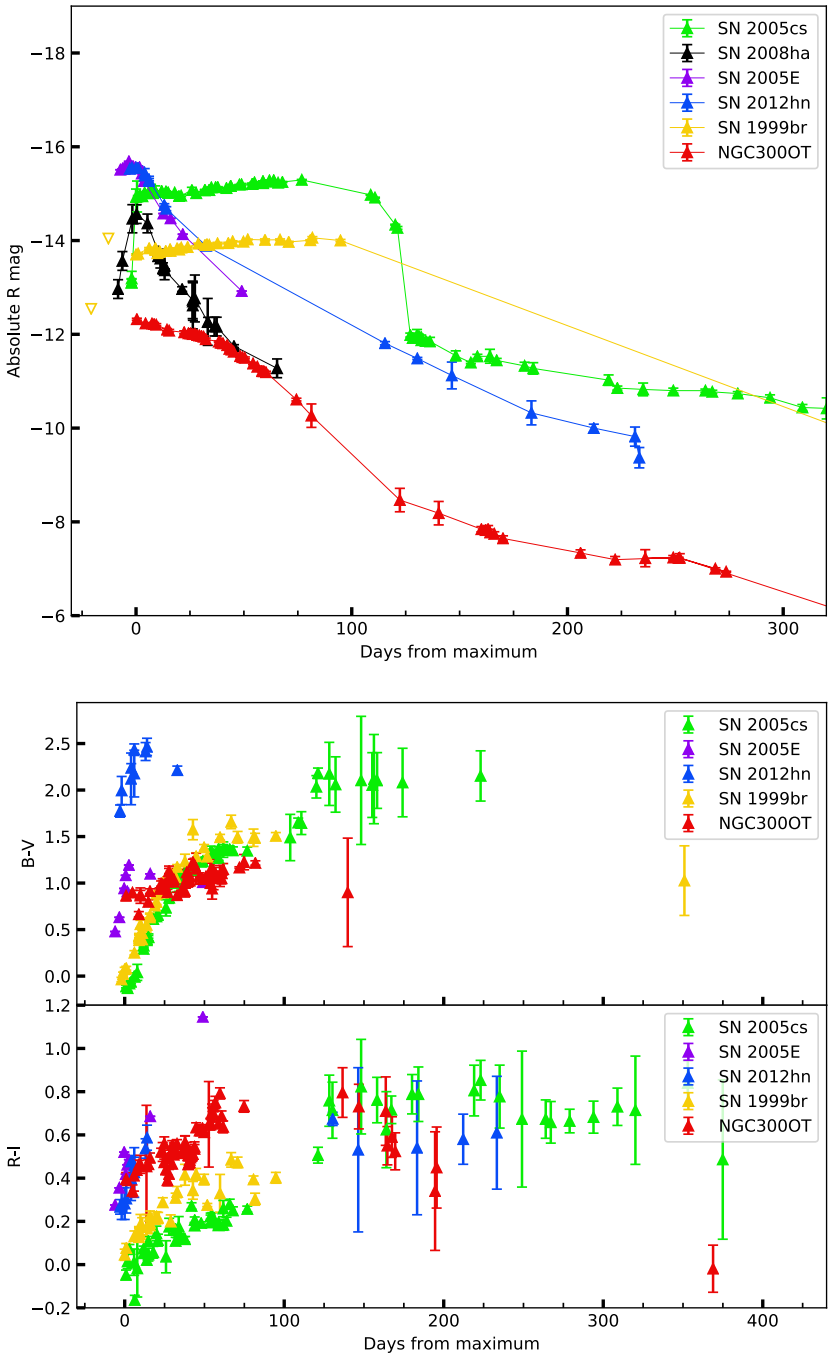

Figure 37: Top panel: R-band absolute light curve of NGC300OT compared with those of several faint SNe. In particular, SN 2005cs (IIP), SN 2008ha (faint Iax), SN 2005E (Ca-rich), SN 2012hn (Ca-rich), SN 1999br (IIP). Bottom panel: B-V and R-I colour curves for the same objects.

4.A Appendix

Here we report the results of our data reduction. A small sample of measures has been taken from AAVSO (https://www.aavso.org), while some of the magnitudes measured have been inferred through spectrophotometry performed on our spectra. The symbol * denotes an upper limit for the luminosity at that epoch. Information on the instruments used are reported in Table [1].

Table A: Johnson-Cousins photometry of NGC300OT (Vega system).

Date yyyymmdd	JD -2400000	U (err)	B (err)	V (err)	R (err)	I (err)	Source
20080516	54602.89	...	15.609(0.049)	14.688(0.023)	14.275(.016)	13.833(.025)	PROMPT3+5
20080520	54606.88	15.920(0.361)	15.654(0.016)	14.700(0.019)	14.240(.012)	13.853(.025)	PROMPT2+5
20080521	54607.84	...	...	...	14.291(.060)	13.834(.038)	REM
20080522	54608.83	...	...	14.819(.072)	14.338(084)	...	REM
20080523	54609.55	...	...	14.819(0.021)	14.320(.015)	13.837(0.016)	PROMPT5
20080524	54610.87	16.088(0.123)	15.719(0.018)	...	...	...	PROMPT3
20080524	54610.87	16.065(0.191)	15.613(0.018)	14.892(0.023)	14.360(.011)	13.851(.016)	PROMPT2+5
20080525	54611.87	...	15.802(0.038)	14.869(0.025)	...	...	PROMPT2
20080525	54611.87	16.089(0.383)	15.788(0.079)	14.866(0.025)	14.337(.031)	13.827(0.028)	PROMPT3+5
20080529	54615.82	...	...	...	...	13.851(.028)	REM
20080529	54615.66	...	...	14.9 (.2)	14.3 (.2)	13.8(.200)	Monard AAVSO
20080530	54616.85	16.128(0.360)	15.742(0.020)	14.888(0.014)	14.407(.014)	13.897(0.02)	PROMPT2+5
20080531	54617.85	16.147(0.288)	15.870(0.020)	14.900(0.015)	14.444(.013)	13.904(0.02)	PROMPT2+5
20080602	54619.67	...	...	...	14.4 (.2)	...	Monard AAVSO
20080603	54620.63	...	...	...	14.4 (.2)	...	Monard AAVSO
20080606	54623.80	...	...	...	...	13.908(.082)	REM
20080606	54623.90	16.400(.018)	15.969(.008)	14.976(.009)	14.432(.011)	...	EFOSC
20080607	54624.84	...	16.056(0.023)	15.005(0.017)	14.475(0.012)	13.907(0.011)	PROMPT2+5
20080608	54625.82	...	16.023(0.037)	14.980(0.048)	14.450(0.035)	13.883(0.026)	PROMPT3+5
20080609	54626.81	...	15.998(0.030)	14.962(0.018)	14.401(0.010)	13.882(0.011)	PROMPT4
20080609	54626.82	...	16.022(0.021)	14.989(0.017)	14.508(0.015)	13.902(0.027)	PROMPT2+5
20080610	54627.82	...	16.030(0.030)	15.029(0.016)	14.422(0.012)	13.937(0.014)	PROMPT3+5
20080611	54628.81	...	16.112(0.049)	15.040(0.017)	14.408(0.017)	13.972(0.019)	PROMPT4
20080611	54628.81	...	16.012(0.025)	15.054(0.018)	14.453(0.015)	13.914(0.011)	PROMPT3+5
20080612	54629.80	...	16.130(0.117)	15.009(0.020)	14.431(0.015)	13.966(0.015)	PROMPT4
20080612	54629.81	...	16.185(0.024)	14.998(0.014)	14.480(0.012)	13.941(0.014)	PROMPT2+5
20080613	54630.80	...	16.220(0.054)	15.094(0.018)	14.492(0.010)	13.931(0.024)	PROMPT4+5
20080613	54630.93	16.591(.013)	...	...	...	...	EFOSC
20080614	54631.81	...	...	15.116(0.018)	14.52(0.011)	13.921(0.017)	PROMPT4
20080614	54631.81	...	...	15.099(0.016)	14.47(0.014)	13.966(0.017)	PROMPT5
20080615	54632.80	...	16.23(0.032)	15.161(0.026)	14.50(0.011)	13.950(0.011)	PROMPT4
20080615	54632.80	...	16.18(0.023)	15.083(0.019)	14.52(0.014)	13.940(0.014)	PROMPT2+5
20080615	54632.92	16.597(.011)	...	...	...	...	EFOSC
20080616	54633.80	...	16.20(0.022)	...	14.520(0.020)	13.95(0.011)	PROMPT2+5
20080617	54634.80	...	16.14(0.027)	15.218(0.017)	14.587 (0.014)	13.98(0.013)	PROMPT2+5
20080620	54637.79	...	16.259(0.058)	15.273(0.026)	14.532 (0.013)	13.97(0.014)	PROMPT4
20080622	54639.79	...	16.267(0.054)	15.295(0.036)	14.614 (0.021)	14.02(0.042)	PROMPT4
20080622	54639.85	...	16.307(0.044)	15.250(0.026)	14.601 (0.021)	13.99(0.023)	PROMPT2+5
20080623	54640.78	...	16.348(0.055)	15.246(0.024)	14.564 (0.012)	13.99(0.016)	PROMPT4
20080623	54640.86	...	16.428(0.025)	15.257(0.017)	14.601 (0.011)	14.00(0.013)	PROMPT2+5
20080624	54641.78	...	16.458(0.055)	15.381(0.031)	14.639 (0.015)	14.08(0.013)	PROMPT4
20080624	54641.78	...	16.483(0.057)	15.327(0.020)	14.573 (0.013)	14.06(0.011)	PROMPT2+5
20080625	54642.78	...	16.417(0.043)	15.334(0.022)	14.628 (0.020)	14.10(0.017)	PROMPT4
20080625	54642.78	...	16.425(0.022)	15.299(0.016)	14.600 (0.033)	14.07(0.014)	PROMPT2+5
20080626	54643.78	...	...	15.350(0.048)	14.65(0.021)	14.10(0.030)	PROMPT4
20080626	54643.78	...	...	15.349(0.046)	14.68(0.016)	14.13(0.017)	PROMPT5
20080627	54644.78	...	16.588(0.023)	15.306 (0.022)	14.703(0.019)	14.146(0.019)	PROMPT2+5
20080628	54645.81	...	16.568(0.065)	15.318 (0.032)	14.717(0.018)	14.126(0.014)	PROMPT4
20080628	54645.77	...	...	15.419(0.024)	14.690(0.015)	14.109(0.014)	PROMPT5
20080629	54646.79	...	16.584(0.164)	15.373 (0.029)	14.784(0.015)	14.104(0.016)	PROMPT4
20080629	54646.76	...	...	15.416(0.043)	14.737(0.020)	...	PROMPT5
20080630	54647.76	...	...	15.407(0.019)	14.822(0.024)	...	PROMPT5
20080701	54648.97	17.04(0.29)	16.634(0.033)	15.508 (0.024)	14.851(0.019)	14.185(0.015)	PROMPT5
20080703	54650.77	...	16.650(0.045)	15.551 (0.020)	14.924(0.013)	14.247(0.010)	PROMPT3+5
20080704	54651.83	...	...	15.660(0.035)	14.915(0.013)	14.257(0.010)	PROMPT3+5

Table A: continued.

Date yyyymmdd	JD -2400000	U (err)	B (err)	V (err)	R (err)	I (err)	Source
20080705	54652.94	17.17(.014)	16.746(.006)	15.619(.006)	14.949(.005)	...	EFOSC
20080707	54654.75	...	...	15.652(.253)	15.023(.173)	14.328(.096)	REM
20080708	54655.75	...	16.947(0.111)	15.750 (0.035)	15.038(0.015)	14.336(0.015)	PROMPT4
20080708	54655.75	...	16.850(0.048)	15.794 (0.025)	15.040(0.022)	14.346(0.013)	PROMPT3+5
20080709	54656.81	...	16.825(0.102)	15.828 (0.048)	15.109(0.028)	14.357(0.024)	PROMPT4
20080709	54656.74	...	16.997(0.076)	15.808 (0.031)	15.071(0.020)	14.331(0.024)	PROMPT3+5
20080710	54657.74	...	16.970(0.144)	15.833 (0.046)	15.148(0.032)	14.406(0.018)	PROMPT4
20080710	54657.73	...	17.000(0.122)	...	15.160(0.016)	14.381(0.021)	PROMPT3+5
20080710	54657.70	...	...	15.840(.182)	...	...	REM
20080711	54658.82	...	17.024(0.057)	15.861 (0.024)	15.220(0.018)	14.424(0.02)	PROMPT3+5
20080713	54660.86	...	17.060(0.056)	15.945 (0.024)	15.217(0.017)	14.519(0.01)	PROMPT3+5
20080714	54661.73	...	17.140(0.109)	16.007 (0.030)	15.324(0.021)	14.486(0.01)	PROMPT3+5
20080715	54662.93	17.597(.021)	17.189(.018)	16.028(.019)	15.317(.010)	...	EFOSC
20080715	54662.72	...	17.166(0.054)	16.058 (0.026)	15.329(0.018)	14.595(0.01)	PROMPT3+5
20080716	54663.73	...	17.312(0.043)	16.106 (0.043)	15.315(0.023)	14.632(0.01)	PROMPT3+5
20080721	54669.37	...	...	16.222(.107)	...	...	Mendicini
20080726	54673.91	18.083(.026)	17.735(.008)	16.512(.004)	15.(.005)	...	EFOSC
20080727	54675.25	...	...	16.59 (.05)	...	...	GCO AAVSO
20080729	54676.84	...	18.022(0.068)	16.74(0.046)	15.(0.02)	14.980(0.018)	PROMPT3+5
20080801	54680.30	...	...	16.89(.07)	...	...	GCO AAVSO
20080805	54683.92	18.721(.081)	18.360(.021)	17.08(.010)	16.11(.004)	...	EFOSC
20080811	54690.26	...	...	17.44(.262)	...	...	Mendicini
20080813	54692.21	...	...	17.50(.051)	...	...	Mendicini
20080815	54694.25	...	...	17.58(.142)	...	...	Mendicini
20080910	54719.70	...	...	18.94(.328)	...	...	REM
20080911	54720.71	...	...	18.93(.388)	17.808(.105)	...	REM
20080915	54724.86	...	...	...	...	17.23(.341)	REM
20080925	54734.73	...	...	...	...	17.56(.098)	REM
20080929	54738.59	...	...	19.78(0.29)1	18.416 (0.094)	17.57(0.07)	PROMPT5
20081002	54741.83	...	20.953(.500)	19.99(.300)	18.616(.300)	...	SpectroPhot
20081009	54748.78	...	...	...	18.649(0.081)	17.87(0.06)	PROMPT5
20081024	54763.53	...	...	...	...	18.08(0.07)	PROMPT4
20081025	54764.56	...	...	20.67(0.349)	18.783 (0.123)	...	PROMPT4
20081026	54765.67	...	...	20.81(0.442)	18.880 (0.136)	18.12(0.08)	PROMPT5
20081027	54766.69	...	...	20.65(0.185)	18.789 (0.059)	18.19(0.06)	PROMPT4
20081030	54769.54	...	...	...	18.818 (0.066)	18.18(0.06)	PROMPT4
20081101	54771.58	...	...	20.81(0.222)	18.824 (0.062)	18.25(0.05)	PROMPT4
20081114	54784.64	...	...	...	...	18.56(.251)	REM
20081126	54796.58	...	...	...	18.976 (0.231)	18.59(0.14)	PROMPT5
20081126	54796.58	...	...	21	...	...	*PROMPT5
20081127	54797.56	...	...	...	19.059(0.128)	18.56(0.14)	PROMPT4
20081129	54799.56	...	...	...	19.109(0.201)	...	PROMPT4
20081204	54804.56	...	...	...	19.179(0.101)	...	PROMPT4
20081224	54824.56	...	...	21	...	...	*PROMPT4
20081225	54825.59	...	...	...	19.343(0.117)	...	PROMPT4
20081226	54826.59	...	...	...	...	18.84(0.15)	PROMPT4
20090519	54970.85	...	...	...	21.238(.080)	21.21(.074)	EFOSC
20090519	54970.93	...	...	...	21.224(.049)	...	EFOSC

Table B: Sloan photometry of NGC300OT (AB mag system).

Date yyyymmdd	JD -2400000	U (err)	B (err)	V (err)	R (err)	I (err)	Source
20080516	54602.380	...	...	14.383(0.021)	14.210(0.024)	14.124(0.022)	PROMPT
20080520	54606.400	...	...	14.474(0.018)	14.207(0.014)	14.108(0.025)	PROMPT
20080520	54606.400	16.653(0.040)	15.129(0.011)	...	...	...	Swope
20080523	54609.390	...	...	14.477(0.013)	14.199(0.012)	14.109(0.031)	PROMPT
20080524	54610.380	...	...	14.487(0.034)	...	...	PROMPT
20080525	54611.367	...	...	14.501(0.023)	14.202(0.018)	14.074(0.014)	PROMPT
20080530	54616.350	...	15.246(0.014)	14.607(0.024)	14.286(0.013)	14.160(0.013)	PROMPT
20080530	54616.325	17.065(0.065)	15.286(0.006)	...	...	...	Swope
20080531	54617.345	...	15.29 (0.04)	14.628(0.027)	14.287(0.017)	14.196(0.021)	PROMPT
20080607	54624.335	...	15.368(0.01)	14.663(0.032)	14.352(0.015)	14.155(0.021)	PROMPT
20080608	54625.320	...	15.409(0.020)	...	...	...	PROMPT
20080609	54626.315	...	15.439(0.027)	14.684(0.021)	14.376(0.017)	14.152(0.036)	PROMPT
20080610	54627.315	...	15.489(0.018)	14.688(0.013)	...	14.167(0.014)	PROMPT
20080611	54628.310	...	15.464(0.014)	14.701(0.024)	14.335(0.011)	14.162(0.017)	PROMPT
20080611	54628.325	17.226(0.035)	15.483(0.007)	...	...	...	Swope

Table B: continued.

Date yyyymmdd	MJD -2400000	U (err)	B (err)	V (err)	R (err)	I (err)	Source
20080612	54629.315	...	15.511(0.009)	14.696(0.048)	14.355(0.008)	14.157(0.014)	PROMPT
20080613	54630.335	...	...	14.721(0.030)	14.328(0.011)	14.179(0.013)	PROMPT
20080613	54630.360	17.290(0.032)	15.537(0.009)	...	...	...	Swope
20080614	54631.317	...	...	14.732(0.020)	14.356(0.022)	14.197(0.018)	PROMPT
20080615	54632.315	...	...	14.740(0.022)	14.350(0.010)	14.177(0.029)	PROMPT
20080616	54633.325	...	...	14.758(0.022)	14.354(0.023)	14.212(0.017)	PROMPT
20080617	54634.317	...	15.590(0.015)	14.810(0.025)	14.383(0.015)	14.206(0.013)	PROMPT
20080623	54640.385	...	...	14.862(0.016)	14.463(0.013)	14.315(0.016)	PROMPT
20080624	54641.300	...	...	14.888(0.018)	14.475(0.012)	14.354(0.053)	PROMPT
20080625	54642.295	...	...	14.899(0.019)	14.528(0.009)	14.388(0.013)	PROMPT
20080627	54644.255	17.691(0.093)	15.838(0.008)	...	...	...	Swope
20080627	54644.273	...	...	14.937(0.022)	14.563(0.014)	14.390(0.039)	PROMPT
20080628	54645.273	...	...	15.016(0.059)	14.578(0.027)	14.411(0.029)	PROMPT
20080629	54646.280	...	...	15.033(0.032)	...	...	PROMPT
20080630	54647.260	...	...	15.077(0.017)	...	...	PROMPT
20080703	54650.250	...	...	15.171(0.030)	14.710(0.056)	14.523(0.010)	PROMPT
20080704	54651.330	...	...	15.193(0.015)	14.744(0.012)	...	PROMPT
20080705	54652.425	...	...	15.208(0.020)	...	14.571(0.019)	PROMPT
20080709	54656.245	...	...	15.330(0.023)	14.930(0.022)	14.681(0.021)	PROMPT
20080711	54658.230	...	16.399(0.029)	15.398(0.017)	14.987(0.022)	14.776(0.050)	PROMPT
20080713	54660.365	...	...	15.491(0.016)	15.010(0.014)	14.787(0.026)	PROMPT
20080714	54661.230	...	...	15.494(0.022)	15.065(0.052)	14.800(0.024)	PROMPT
20080715	54662.220	...	...	15.514(0.021)	15.065(0.011)	14.787(0.016)	PROMPT
20080729	54676.345	...	17.112 (0.032)	16.097(0.029)	15.612(0.023)	15.111(0.039)	PROMPT
20080805	54683.300	...	17.88(0.25)	16.44 (0.25)	15.94(0.25)	15.65 (0.25)	Spectrophot
20080917	54724.300	...	20.46(0.25)	18.24 (0.25)	...	...	Spectrophot
20080929	54738.100	...	...	...	...	17.557(0.070)	PROMPT
20081002	54742.300	...	...	18.52 (0.25)	...	...	Spectrophot
20081003	54742.090	...	...	...	...	17.674(0.052)	PROMPT
20081023	54762.097	...	...	18.862(0.056)	18.554(0.063)	...	PROMPT
20081025	54764.085	...	...	18.881(0.074)	18.588(0.105)	18.012(0.105)	PROMPT
20081026	54765.197	...	...	18.859(0.075)	18.642(0.131)	...	PROMPT
20081027	54766.120	...	...	18.932(0.069)	18.758(0.067)	18.044(0.086)	PROMPT
20081029	54768.060	...	...	18.962(0.046)	18.785(0.080)	18.118(0.081)	PROMPT
20081102	54772.100	...	...	19.058(0.055)	18.903(0.092)	18.225(0.090)	PROMPT
20081127	54797.080	...	...	...	...	18.417(0.117)	PROMPT
20081207	54807.060	...	...	...	...	18.576(0.135)	PROMPT
20081208	54808.060	...	...	19.368(0.066)	...	...	PROMPT
20081209	54809.080	...	...	...	19.478(0.096)	...	PROMPT
20081224	54824.090	...	...	19.511(0.067)	...	...	PROMPT
20081225	54825.070	...	...	...	...	18.698(0.134)	PROMPT
20090120	54851.040	...	21.99(0.043)	19.467(0.044)	...	...	GMOS-S
20090107	54838.050	...	...	19.480(0.182)	...	...	GMOS-S
20090122	54853.555	...	22.064(0.160)	19.475(0.014)	19.943(0.012)	...	Magellan Clay
20090208	54870.539	...	22.403(0.218)	19.705(0.020)	20.305(0.038)	19.317(0.024)	Magellan Clay
20090213	54875.544	...	22.606(0.193)	19.770(0.012)	20.382(0.014)	19.384(0.011)	Magellan Clay
20090123	54854.050	...	...	19.473(0.089)	...	...	GMOS-S
20090519	54970.403	...	...	21.228(0.228)	21.686(0.039)	21.013(0.056)	GMOS-S
20090713	55025.360	...	...	22.244(0.094)	...	...	GMOS-S
20090713	55025.380	...	23.173	...	...	...	*GMOS-S
20090724	55036.420	...	...	...	22.848(0.500)	...	*GMOS-S
20090726	55038.280	...	...	...	23.004(12.00)	...	*GMOS-S
20090828	55071.150	...	...	22.764(0.069)	...	...	GMOS-S
20091116	55151.133	...	...	23.364	23.415	23.487	*GMOS-S

Table C: NIR photometry of NGC300OT.

Date dd/mm/yyyy	JD -2400000	J (err)	H (err)	K (err)	Source
20/5/08	54606.35109	...	12.67(0.24)	...	REM
21/5/08	54607.33718	...	12.64(0.18)	...	REM
22/5/08	54608.82834	13.12(0.033)	12.608(0.10)	...	REM
23/5/08	54609.82545	13.09(0.056)	12.617(0.12)	...	REM
24/05/0	54610.908	...	...	11.94(0.067)	REM
25/5/08	54611.82019	13.10(0.161)	...	...	REM
30/5/08	54616.80650	13.09(0.054)	12.631(0.050)	12.044(0.089)	REM
31/5/08	54617.80371	13.16(0.069)	12.609(0.038)	...	REM
06/6/08	54623.78490	13.03(0.195)	12.558(0.443)	...	REM

Table C: continued.

Date dd/mm/yyyy	JD -2400000	J (err)	H (err)	K (err)	Source
07/6/08	54624.79958	13.10(0.046)	12.533(0.042)	...	REM
08/6/08	54625.79018	13.11(0.052)	12.531(0.351)	...	REM
09/6/08	54626.77918	13.12(0.073)	...	...	REM
10/6/08	54627.77623	13.11(0.067)	12.562(0.344)	...	REM
11/6/08	54628.27788	...	12.58 (0.29)	...	REM
12/6/08	54629.77144	13.07(0.057)	...	...	REM
13/6/08	54630.76827	13.11(0.088)	12.608(0.063)	...	REM
14/6/08	54631.83902	13.09(0.039)	12.592(0.051)	...	REM
15/6/08	54632.76271	13.10(0.093)	12.597(0.124)	11.900(0.113)	REM
16/6/08	54633.76298	13.13(0.137)	...	11.924(0.168)	REM
17/6/08	54634.85931	13.16(0.070)	...	...	REM
21/6/08	54638.25460	...	12.6(0.344)	...	REM
22/6/08	54639.74469	13.19(0.078)	...	...	REM
23/6/08	54640.74067	13.19(0.096)	12.689(0.082)	...	REM
24/6/08	54641.76544	...	...	12.066 (.216)	REM
25/6/08	54642.74297	13.21(0.066)	12.713(0.051)	...	REM
28/6/08	54645.72723	13.23(0.036)	12.770(0.201)	12.035 (0.196)	REM
29/6/08	54646.72454	13.28(0.045)	12.784(0.157)	...	REM
30/6/08	54647.72185	13.37(0.089)	12.789(0.122)	...	REM
01/7/08	54648.71903	13.23(0.669)	12.748(0.130)	12.073(0.119)	REM
02/7/08	54649.71640	13.40(0.042)	12.817(0.168)	...	REM
03/7/08	54650.71790	13.33(0.038)	12.874(0.177)	...	REM
04/7/08	54651.71084	13.35(0.064)	13.032(0.259)	...	REM
06/7/08	54653.73209	13.37(0.095)	12.947(0.266)	12.124(0.083)	REM
07/7/08	54654.74791	13.42(0.090)	12.964(0.066)	12.108(0.121)	REM
08/7/08	54655.89660	13.46(0.057)	13.010(0.054)	12.150(0.094)	REM
09/7/08	54656.77837	13.52(0.046)	13.031(0.202)	12.154(0.074)	REM
10/7/08	54657.69441	13.54(0.059)	13.035(0.166)	...	REM
11/7/08	54658.69177	13.57(0.059)	...	...	REM
13/7/08	54660.68630	13.53(0.042)	13.120(0.297)	...	REM
14/7/08	54661.68248	13.65(0.047)	13.148(0.119)	...	REM
15/9/08	54724.75556	15.53(0.074)	...	13.47(0.104)	REM
25/9/08	54734.73999	15.79(0.144)	14.335(0.075)	13.57(0.087)	REM
12/11/09	54782.55899	17.18(0.540)	...	...	REM
13/11/0	54783.55234	17.15(0.161)	16.309(0.157)	...	REM
14/11/09	54784.290	17.42(0.522)	16.236(0.254)	15.257(0.099)	REM
18/05/09	54969.905	19.48(0.144)	16.890(0.042)	14.628(0.019)	SOFI
14/09/09	55088.695	20.94(0.214)	17.984(0.045)	15.441(0.011)	SOFI
23/11/09	55158.731	21.69(0.268)	18.607(0.098)	15.895(0.021)	SOFI
26/12/09	55191.534	...	19.361(0.127)	16.005(0.031)	SOFI
24/01/10	55220.529	...	...	16.387(0.096)	SOFI

5 Physical Parameters Estimate

In the previous section we obtained the absolute magnitudes of NGC300OT in several broad band filters, starting from the epoch of peak luminosity to more than one year later. Here we are going to discuss the physical properties of the transient that can be determined from the study of our observations. In particular, we determine the ^{56}Ni mass ejected by the transient and the evolution of its temperature, radius and luminosity.

5.1 Bolometric Light Curve and Ejected ^{56}Ni Mass

We obtain a quasi-bolometric light curve by integrating the fluxes of NGC300OT from the ultraviolet to the NIR bands. If no observations are available in a given filter, we extrapolate the missing values making use of a well sampled band (typically R), assuming a constant colour from the last observed epoch. In order to avoid over-extrapolation, when the sampling of the transient becomes sparse (i.e. after $\sim$ 100 days) we only select the epochs with observations in the K-band, since it is the most luminous at these epochs and hence the most influential in the computation of the quasi-bolometric luminosity. Flux measures are corrected for reddening (see Section [4.3]), yielding the SED at each selected epoch. Then an integration of the SED using the trapezoidal rule provides the total flux received from the ultraviolet to NIR domains. As no information outside these boundaries is available we truncate the integration, ignoring the contribution outside the aforementioned limits. For this reason the inferred luminosity has to be considered ”quasi”-bolometric. Finally the flux is converted into luminosity adopting the distance of NGC 300 estimated in Section [4.3]. The results are shown in Figure [38].

In the case of NGC300OT, in analogy with other ILRTs, the luminosity contribution from the shortest wavelengths can safely be neglected, but the same is not true for the mid-infrared (MIR) contribution. As the SED peak shifts toward longer wavelegths, the bulk of the luminosity at late times is emitted in the MIR, leaving only the emission from spectral lines without continuum flux in the optical domain. For this reason, the quasi-bolometric light curve has to be treated as an underestimate of the total luminosity emitted, in particular at the late phases.

To estimate the ^{56}Ni mass ejected during the explosion, we follow two different approaches, both exploiting the late linear tail of the quasi-bolometric light curve. First of all, we make use of the measure performed by Botticella et al. (2009), which compared the quasi-bolometric luminosity of SN 2008S during the late tail

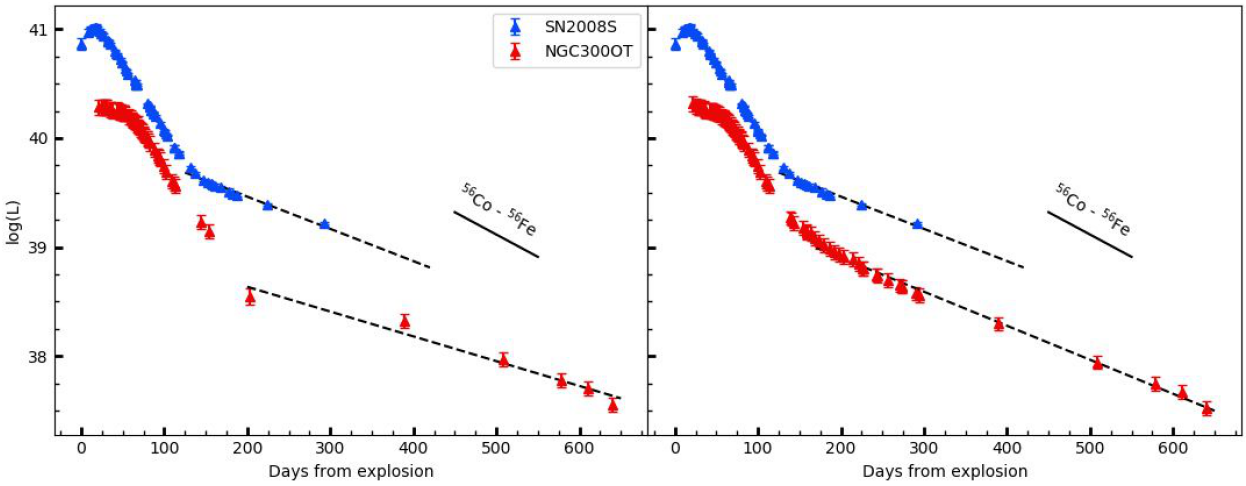

Figure 38: Quasi-bolometric light curves of SN 2008S and NGC300OT obtained from the integration from the optical to the NIR bands. Left panel: quasi-bolometric light curve obtained from our data set. Right panel: quasi-bolometric light curve from the second data set, with measures from Humphreys et al. (2011) including our late SOFI data. The decay rate of ^{56}Co is shown as a solid black line for comparison. The dashed black line is a linear fit to the late phase for both objects.

(140-300 days after explosion) with that of SN 1987A, obtaining M(^{56}Ni)$_{08S}$ = 1.4 x 10^{-3} $M_{\odot}$. The quasi-bolometric luminosities of SN 2008S and SN 1987A were calculated with the same technique used for NGC300OT. The ^{56}Ni ejected is obtained through the following relation:

$$M(^{56}Ni)_{N300} = M(^{56}Ni)_{08S} \times \frac{L_{N300}}{L_{08S}} \tag{5}$$

where M(^{56}Ni)$_{N300}$ is the ^{56}Ni mass ejected by NGC300OT and L_{N300} / L_{08S} is the ratio between the quasi-bolometric luminosities of NGC300OT and SN 2008S compared at the same epoch. We compute M(^{56}Ni)$_{N300}$ for both our and Humphreys et al. (2011) data sets: the results are reported in Table [9]. The measurements errors of each measure are calculated through the error propagation:

$$\delta M_{N300} = \sqrt{\left(\delta M_{08S}\frac{L_{N300}}{L_{08S}}\right)^2 + \left(M_{08S}\frac{\delta L_{N300}}{L_{08S}}\right)^2 + \left(M_{08S}\frac{L_{N300}\delta L_{08S}}{L_{08S}^2}\right)^2} \tag{6}$$

Quantities preceded by δ are associated errors. The first of the three terms contains the most relevant source of uncertainty, δM_{08S}. For this reason, a lower luminosity

OAPD		Humphreys	
Day	^{56}Ni x 10^{-4} $M_\odot$	Day	^{56}Ni x 10^{-4} $M_\odot$
203	1.8 ± 0.4 (22%)	158	5.3 ± 1.2 (23%)
292	2.3 ± 0.5 (22%)	224	3.8 ± 0.9 (24%)
389	3.7 ± 0.9 (24%)	292	3.1 ± 0.7 (23%)
Mean	**2.6 ± 0.6 (23%)**		**4.1 ± 0.9 (23%)**

Table 9: Ejected mass of ^{56}Ni measured for both data sets as described in the text. The final value is shown in bold at the bottom. The percentage errors are reported in brackets.

	ph (days)	ψ (mag/100d)	$^{56}Ni_{87A}$	$^{56}Ni_{Hamuy}$
300OT OAPD	200-620	0.57 ± 0.08	**2.6 ± 0.6**	**7.7 ± 3.0**
300OT Humphreys	140-620	0.78 ± 0.01	**4.1 ± 0.9**	**5.3 ± 1.3**
SN2008S	145-310	0.67 ± 0.03	14 ± 3	11 ± 2

Table 10: Phase, magnitude decline, ^{56}Ni mass ejected (in 10^{-4} $M_\odot$ units) estimated through a comparison with SN 1987A and ^{56}Ni mass calculated with Equation [7]. The ^{56}Ni mass for SN2008S was taken from Botticella et al. (2009).

is associated with a lower error, making a pondered mean skewed towards lower masses. Therefore, we choose to adopt the arithmetic mean of the three ^{56}Ni mass values for each data set. As the percentage errors in Table [9] remain roughly constant for the different measures, we associate to the final measure a percentage error which is the mean of the percentage errors of each measure.

For a second, independent estimate of the ^{56}Ni mass, we follow the approach of Hamuy (2003), and use the formula:

$$M(^{56}Ni)_{N300} = 7.886 \times 10^{-44} \times L_{N300} \times exp\left[\frac{(t - t_0)/(1 + z) - \tau_{Ni}}{\tau_{Co}}\right] M_\odot \qquad (7)$$

where (t-t_0) is the time after explosion in days, z is the host galaxy redshift, τ_{Ni} is the ^{56}Ni half life (6.1 days) and τ_{Co} is the ^{56}Co e-folding time (111.6 days). This relation assumes full deposition of the γ-rays produced by the ^{56}Co to ^{56}Fe decay. To obtain the final value, we calculate the ^{56}Ni mass for each point in the

light curve linear tail, then averaging the results. The propagation of error yielded an unrealistically low value that does not account for the observed scatter, so we adopt the standard deviation as the best estimate for the uncertainty of this measure (Table [10]). Since the late tail luminosity is likely powered also by other energy sources, such as the interaction between the ejecta and a dense circumstellar wind (Kochanek 2011) or the emission from a warm component like dust, our ^{56}Ni mass estimates should be regarded as upper limits to the true value, since we derived our estimated under the assumption that the whole luminosity comes from radioactive decays.

5.2 Spectral Energy Distribution Analysis

In order to infer the temperature (T) and radius (R) of the emitting source, we study the SED of NGC300OT. The temperature is obtained through the fit of the observed broadband fluxes with a Planck function:

$$B_\lambda(\lambda, T) = \frac{2h}{c^2} \frac{1}{e^{\frac{hc}{\lambda k_b T}} - 1} \tag{8}$$

where B_λ is the flux per unit wavelength, h is the Planck constant, c is the speed of light and k_b is the Boltzmann constant. The luminosity is measured integrating the resulting Planck function over the relevant wavelengths range, and then accounting for the interstellar reddening and the distance of the transient. Finally, the radius is inferred from the Stefan-Boltzmann law for a spherical black body:

$$L = 4\pi\sigma R^2 T^4 \tag{9}$$

where σ is the Stefan-Boltzmann constant. In Figure [39] we show a sample of the fits we performed, as well as the evolution of the inferred parameters. We find that the profile is well reproduced by a single black body until 117 days after maximum, while afterwards we carry out simultaneous two-component fits (hot plus warm black bodies), in order to account for the observed NIR excess. We note that the NIR fluxes become dominant when the Balmer decrement described in Section [6.2] starts to increase: this observation supports the scenario of dust formation around the transient from $\sim$ 100 days. After $\sim$ 180 days, the contribution of Hα is so dominant, with respect to the continuum, that the energy distribution is no longer that of a black body. For this reason, we stop the SED analysis at that epoch. Compared to SN 2008S and AT 2017be, the hot black body component of NGC300OT is the coldest among the three, with a temperature of $\sim$

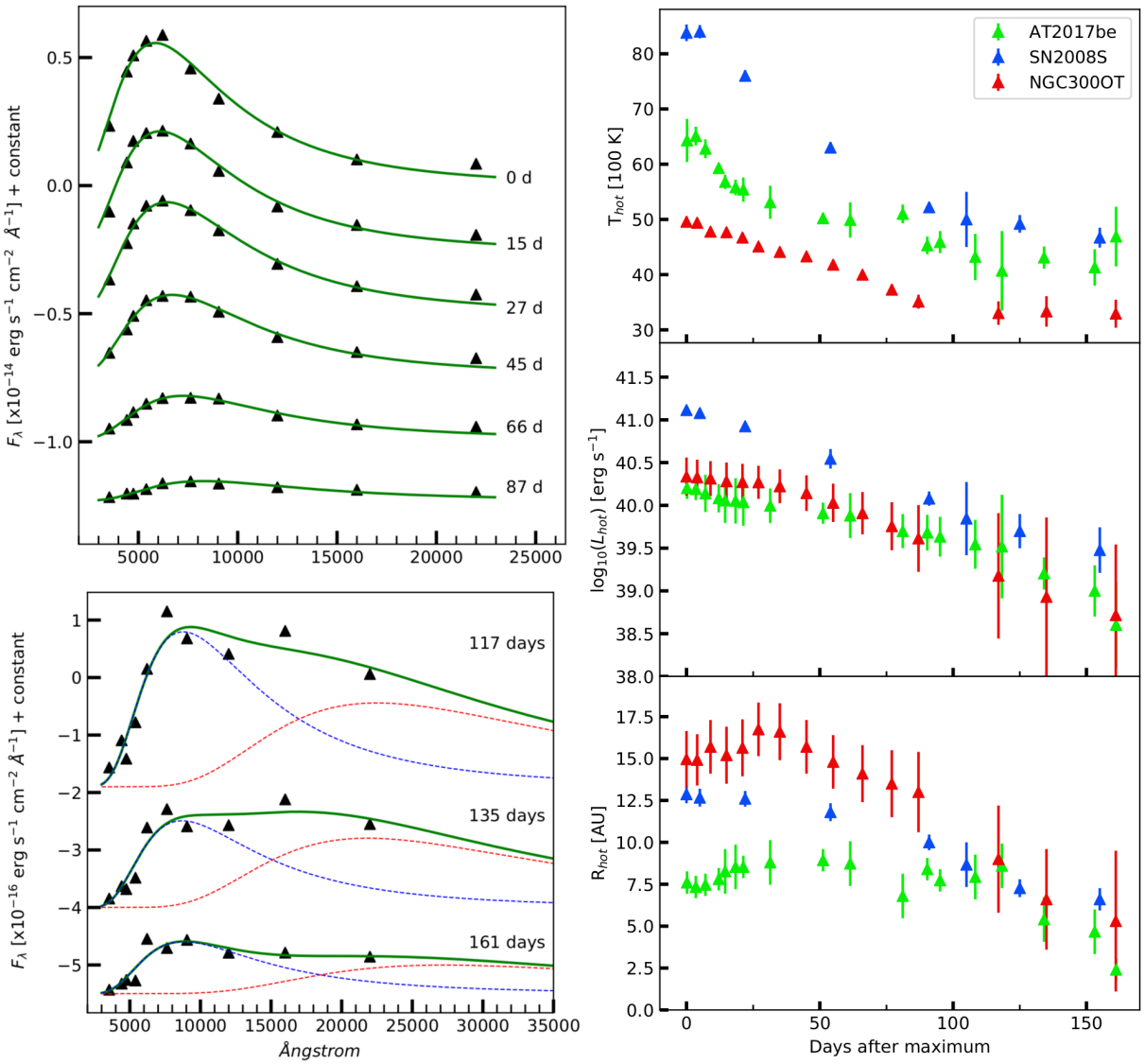

Figure 39: Top left: SED fit for NGC300OT. Phases reported are with respect to peak luminosity of the transient. Bottom left: from 117 days onward we fit the observations using simultaneously two black bodies, to fit the observations. The hot component is displayed as a blue dotted line, while the warm component is displayed in red. Right panels: temperature, luminosity and radius evolution of NGC300OT compared with those of ILRTs SN 2008S and AT 2017be.

5000 K at peak, steadily decreasing to 3300 K, where the temperature decrease appears to slow down significantly. During the first 50 days, the radius remains roughly constant ($\sim$ 16 AU), consistently with the pseudo-plateau displayed in the light curves. The luminosity evolution of NGC300OT is quite similar to that of AT 2017be, while SN 2008S is characterized by a luminosity which is roughly one order of magnitude greater than both the other transients, owing to its higher temperature. As time passes new dust forms, and the NIR fluxes are progressively dominated by this new warm component ($\sim$ 1200 K) that we detect after 100 days post-maximum. For this warm black body component we find that the temperature slightly declines with time, from around 1300 K to 1000 K at $\sim$ 160 days. Similarly the radius of the warm component remains roughly constant at 55 AU. Such values are in excellent agreement with the component identified as "hot dust" by Prieto et al. (2009) 93 days after the detection. As mentioned in Section [2.4], with the help of a MIR spectrum it was possible to infer the presence of three black bodies: the "hot dust" showed a temperature of 1500 K and a radius of 67 AU, in good agreement with our warm black body identified after $\sim$ 100 days. The lack of observations at higher wavelengths, however, leads to serious uncertainties on our measures. The values of some physical parameters inferred for the black body components are reported in Table [11].

Despite the remarkable agreement with a single black body fit at short wavelengths, there is a consistent excess in the K-band flux that appears to be constant with time. The lack of MIR measures makes it difficult to infer the parameters of a second black body at early stages, but following previous studies on ILRT we tentatively explain this NIR excess with the emission of cold dust that survived the explosion. This feature has already been observed in SN 2008S (Botticella et al. 2009), where early MIR flux observations allowed to detect a cold black body with a temperature of $\sim$ 590 K, attributed to an IR echo from pre-existing circumstellar dust. In a similar way, a cold component characterized by a temperature of $\sim$ 700 K was detected by Humphreys et al. (2011) for NGC300OT at day 2 after maximum light. We suggest that this cold component, produced by distant pre-existing dust, remains constant with time, explaining the early K-band flux excess.

Phase (Days)	T_{hot} (K)	L_{hot} (10^{39} erg s^{-1})	R_{hot} (AU)	T_{warm} (K)	L_{warm} (10^{39} erg s^{-1})	R_{warm} (AU)
0	4960 (90)	21.7 (4.9)	15.0 (1.7)			
4	4940 (80)	21.3 (4.4)	14.9 (1.5)			
9	4780 (70)	20.6 (4.2)	15.7 (1.6)			
15	4770 (80)	19.1 (4.2)	15.2 (1.7)			
21	4670 (80)	18.7 (4.0)	15.6 (1.7)			
27	4510 (60)	18.6 (3.6)	16.7 (1.6)			
35	4410 (60)	16.7 (3.3)	16.6 (1.7)			
45	4330 (70)	13.9 (2.9)	15.7 (1.6)			
55	4180 (70)	10.7 (2.4)	14.8 (1.6)			
66	4000 (80)	8.1 (2.0)	14.1 (1.7)			
77	3730 (100)	5.7 (1.6)	13.5 (2.0)			
87	3510 (130)	4.1 (1.6)	13.0 (2.4)			
117	3300 (210)	1.5 (1.1)	9.0 (3.2)	1290 (310)	1.7	62
135	3330 (280)	0.9 (0.8)	6.6 (3.0)	1330 (260)	1.4	53
161	3290 (250)	0.5 (0.4)	5.3 (4.2)	1060 (250)	0.6	55

Table 11: Evolution of temperature, luminosity and radius for the hot and warm black body components of NGC300OT. The error relative to each measure is reported in brackets. As only the blue tail of the warm black body component has been observed, the errors on its luminosity and radius are of the same order of magnitude af the measures themselves.

6 Spectroscopy

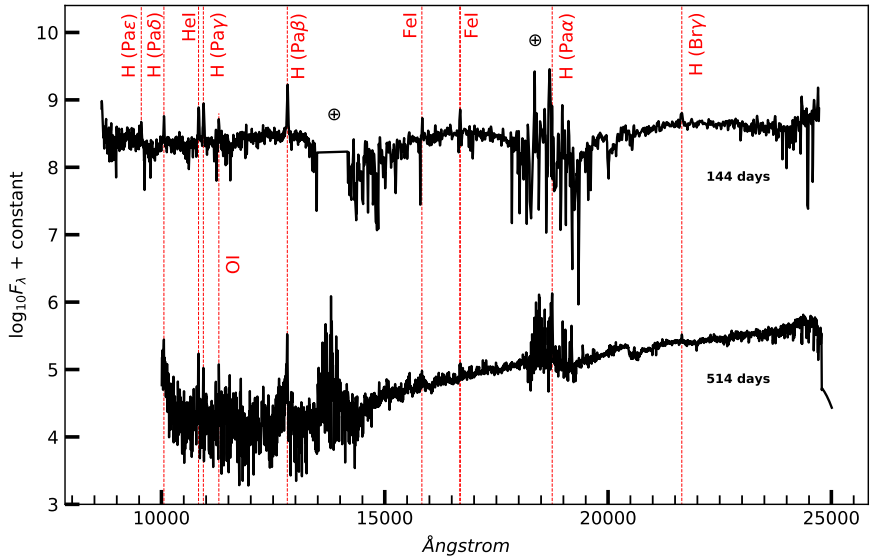

Figure 41: NIR spectra of NGC300OT, respectively taken with TNG+NICS and VLT+X-Shooter. The most prominent lines are indicated with red vertical lines. Epochs reported to the right are relative to the R-band maximum. The ⊕ symbols mark the telluric absorption bands of H_2O and CO_2.

6.1 Line Identification

Our optical spectra span 8 months, from 2008 May 16 (epoch of maximum light) to 2009 January 21. The optical spectrum of NGC300OT is characterized by strong hydrogen lines, the Ca II NIR triplet and the [Ca II] forbidden doublet. In the high-resolution UVES spectrum, taken on 2008 July 02, we identify the Balmer series from Hα to H11, with the exception of Hϵ, which is blended the Ca II H&K absorption feature. Additionally, we find [O I], O I, He I, Na I D, Fe I (multiplets 15 and 49), Fe II (multiplets 6, 14, 19, 40, 42, 46, 73) and Sc II (multiplet 29) lines (Figure [40]). In Table [12] we report a list of the most prominent lines, along with their FWHM and measured intensity. Unfortunately, the VLT+UVES spectrum used for line identification contains several wavelength gaps due to detectors configuration: for this reason we could not observe the Ca II NIR triplet at high-resolution. In the NIR spectra taken with TNG+NICS and

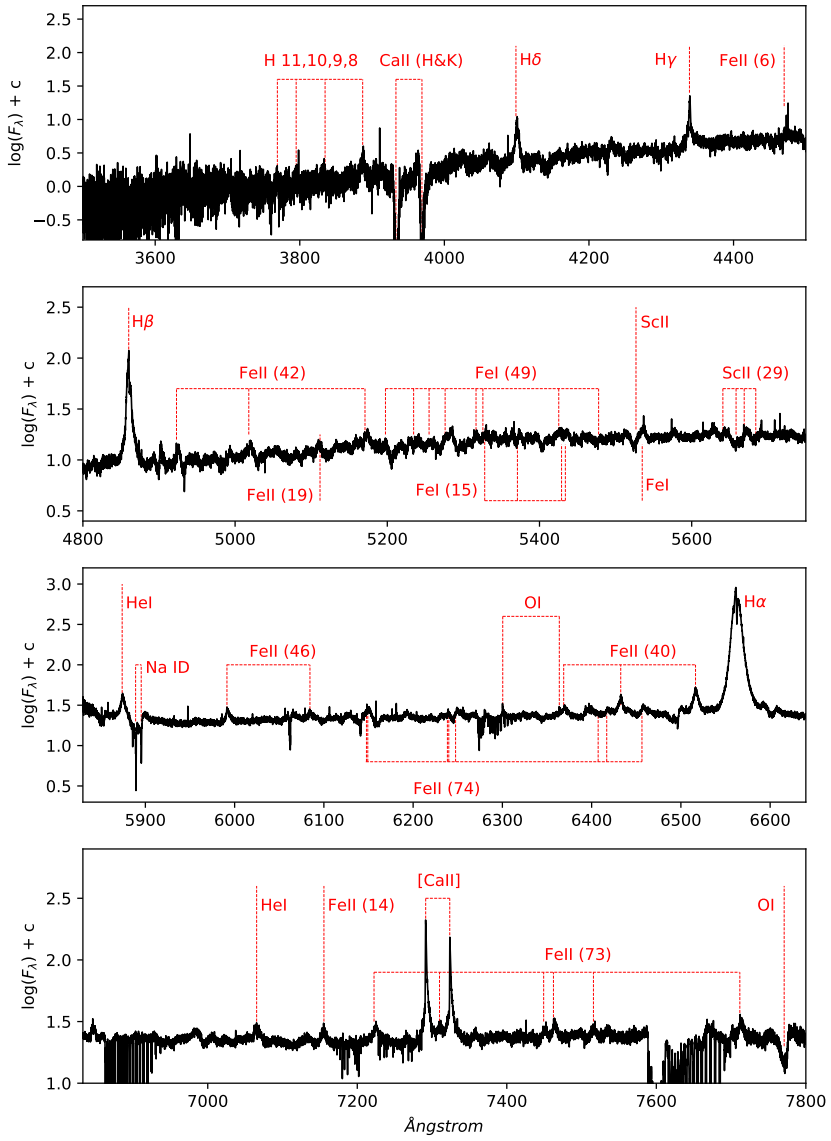

Figure 40: Line identification performed on the VLT+UVES spectrum of NGC300OT taken on 2008 July 02. The spectrum has been red-shift corrected.

VLT+X-Shooter, the most prominent features are again hydrogen lines: we observe the Paschen series from α to ϵ, along with the Brackett γ line. Additionally we detect He I, O I and Fe I lines, consistently with what we find in the optical spectra. All the lines were detected at both epochs.

6.2 Spectral Evolution

In Figures [42] and [43] we show our sequence of optical spectra, covering the epochs from maximum light to 243 days after peak luminosity. The Hα, Hβ, [Ca II] and Ca II NIR triplet are recognizable during the whole evolution of the spectrum. We do not detect P-Cygni profiles, that characterize typical SN explosions. The nebular phase starts roughly at $\sim$ 100 days after maximum light, since the contribution from the continuum in the spectrum taken at 123 days is already negligible. Here we present the evolution of the fluxes and FWHM velocities of the most prominent lines. We estimate the line parameters through the IRAF task SPLOT, assuming a Lorentzian profile and deblending the multi components when necessary (as for the case of the Ca II NIR triplet). In order to account for the resolution of the instrument used, we calculate the resulting width of the line as $w = \sqrt{FWHM^2 - resolution^2}$. To obtain the luminosity and FWHM velocity from the measured flux and width, we use the well known equations:

$$\mathrm{v}_{FWHM} = \frac{w}{\lambda_0} c \qquad \text{and} \qquad L_\lambda = 4\pi d^2 F_\lambda \tag{10}$$

where v_{FWHM} is the FWHM velocity, λ_0 is the position of the line centre at rest wavelength, c is the speed of light, L_λ is the luminosity, F_λ is the flux and d is the distance of NGC 300 (see Section [4.3]). Errors on the luminosities are conservatively assumed to be 20%, mainly owing to the error on the flux measure.

Here we analyze the evolution of the most prominent spectral features:

- **Hα** is the brightest and the broadest line detected in the spectra. Its FWHM velocity during the first 15 days after maximum decreases steadily from 760 to 610 km s^{-1}, then varies between 610 and 360 km s^{-1} in a rather erratic way. This behaviour is likely due to the FWHM of the line being close to the resolution of the instrument, therefore reducing the accuracy of the measure (compare Table [13] with Table [2]). Thanks to our VLT+UVES high-resolution spectrum we obtain a precise estimate for the Hα velocity at 46 days, $\mathrm{v}_{FWHM} \sim 540$ km s^{-1}. In Figure [44] the evolution of the Hα profile is displayed. The position of the peak does not appear to vary significantly with time. The Hα luminosity of the transient at maximum light

Line	λ_0 (Å)	λ_m (Å)	FWHM (Å)	F (10^{-15} erg s^{-1}cm^{-2})
Hα	6562.8	6562.5	11.4	162
Hβ	4861.3	4860.3	5.7	26.7
Hγ	4340.5	4339.4	5.3	9.0
Hδ	4101.7	4100.7	4.5	5.6
[Ca II]	7291.47	7292.0	2.8	13.8
[Ca II]	7323.89	7323.4	2.8	10.9
Ca II H&K	3933.66	3933.9	4.2	-
Ca II H&K	3968.47	3969.0	3.8	-
Fe II (40)	6516.05	6516.7	5.7	8.1
Fe II (40)	6432.65	6432.8	4.4	4.0
Fe II (40)	6369.45	6368.7	9.1	4.1
Fe II (42)	5169.0	5170.7	8.8	4.8
Fe II (42)	5018.4	5018.6	8.3	3.7
Fe II (42)	4923.9	4925.2	6.4	3.9
Fe II (46)	5991.38	5992.5	6.0	4.3
Fe II (46)	6084.11	6084.4	6.4	2.2
He I	5875.62	5874.9	4.3	4.8
He I	7065.19	7065.7	5.5	2.4
O I	7771.94	7770.5	7.8	-
[O I]	6363.78	6363.9	1.2	0.3
[O I]	6300.3	6300.4	1.4	0.9
Na I	5889.9	5889.5	0.25	-
Na I	5895.9	5895.5	0.24	-

Table 12: Line identification performed on the UVES spectrum taken on 2008 July 02, 46 days after maximum. Na I, O I and Ca II H&K lines are observed in absorption The spectrum was redshift corrected with the z value of NGC 300, as reported in Section [4.3].

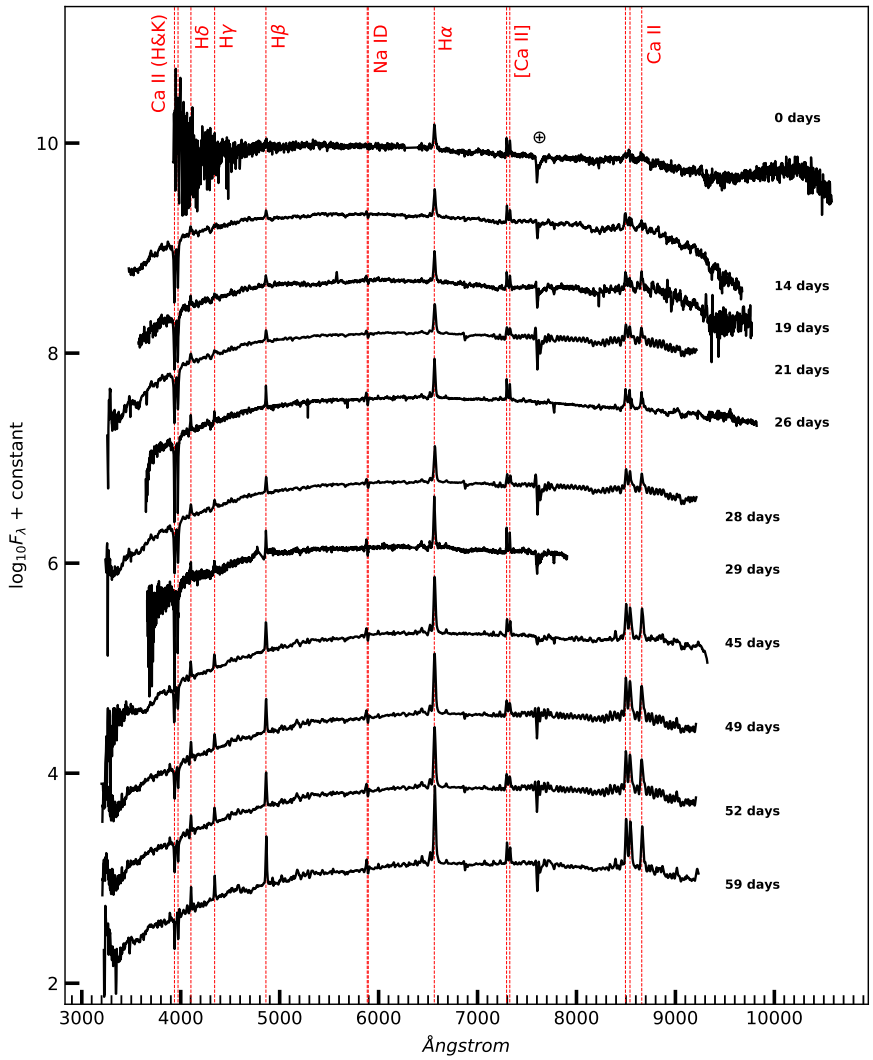

Figure 42: Early spectral sequence of NGC300OT. Main emission and absorption features are marked with vertical dashed lines. The ⊕ symbol indicates the position of a strong telluric band. All spectra have been corrected for the redshift of NGC300OT. Phases from maximum luminosity are indicated on the right.

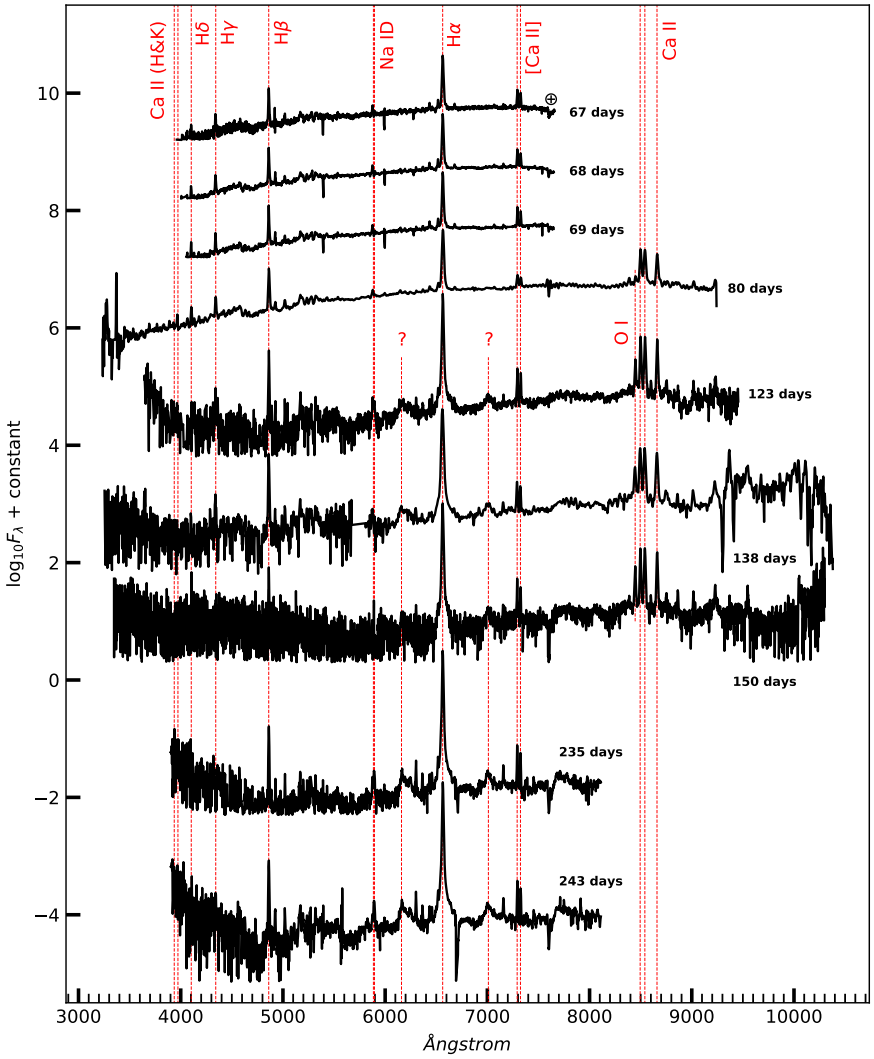

Figure 43: Late spectral sequence of NGC300OT. We use the same conventions adopted in Figure [42].

is $3x10^{37}$ erg s^{-1}, and quickly increases up to $6.3x10^{37}$ erg s^{-1} at around 90 days after maximum. Later, the luminosity decreases steadily to the initial value at around 160 days after maximum. The following decline is slower, and the Hα luminosity fades to 1.5 $x10^{37}$ erg s^{-1} on 2009 January 20. The Hα luminosity evolution of NGC300OT is compared with those of SN 2008S (Botticella et al. 2009) and AT 2017be (Cai et al. 2018) in Figure [45]. The Hα luminosity of NGC300OT evolves quite differently from that of SN 2008S: in that case, the Hα peak luminosity is coincident with the transient maximum light, and then it steadily declines. On the other hand, AT 2017be displays a rebrightening in the Hα luminosity similar to NGC300OT. Cai et al. (2018) tentatively attribute this feature to the strengthening of the interaction between ejecta and CSM. It is interesting to note that both AT 2017be and NGC300OT show a pseudo-plateau, which is not observed in SN 2008S: further studies are required to understand if the rebrightening of Hα luminosity can be a diagnostic feature to separate two groups of objects (IIP-like and IIL-like) inside the ILRT class.

- The **Hβ** line shows a behaviour similar to that of the Hα. The FWHM velocities inferred are slightly lower, varying between 700 and 220 km s^{-1}, with the high-resolution spectrum yielding a velocity of 370 km s^{-1}. The luminosity of the line during the maximum light of the transient is $5.8x10^{36}$ erg s^{-1}, rising to $1.2x10^{37}$ erg s^{-1} at $\sim$ 80 days. The following decline appears to be steeper than the decline of the Hα luminosity. This is evident in the Balmer decrement evolution (the ratio $L_{H\alpha}$ / $L_{H\beta}$) shown in the lower panel of Figure [45]. During the first $\sim$ 80 days the ratio remains roughly constant, with a mean value of 5.4. After the Hβ peak, the Balmer decrement quickly increases, up to 26 in January 2009. Since the Balmer decrement can be used to estimate the line of sight reddening, such increment suggests dust formation. This is consistent with the case of SN 2008S, where dust started forming after $\sim$ 120 days (Botticella et al. 2009).

- The **Ca II NIR triplet**, differently from [Ca II] and Hα features, is only barely detectable in the spectrum at maximum light (Figure [44]). The position of the peaks do not show a clear evolution with time. The triplet displays slightly different velocities for the three different peaks. In June, the Magellan+LDSS3 spectrum yields v_{FWHM} of 600, 610 and 730 km s^{-1} respectively for the λ8498, λ8542 and λ8662 Å components. This was the highest resolution spectra available (4 Å) for this multiplet. On 2008 October 14 the measured velocities are 260, 330 and 300 km s^{-1}, displaying a substantial decrease with respect to June. The integrated luminosity of the three lines displays an increase even sharper than the Hα luminosity, rising from $3.3x10^{37}$ erg s^{-1} to $9.5x10^{37}$ erg s^{-1} by day 75 (Figure [45]). Also the

Date	F (Hα)	FWHM (Hα)	v (Hα)	F (Hβ)	FWHM (Hβ)	v (Hβ)
2008-05-16	8.7	17.1	760	1.8	–	–
2008-05-30	9.4	17.0	690	1.6	13.4	660
2008-06-04	9.5	15.6	610	2.2	13.9	700
2008-06-06	11.0	18.7	510	1.9	12.4	350
2008-06-11	12.0	14.0	610	2.1	7.2	370
2008-06-13	13.3	17.5	410	2.2	10.5	–
2008-06-15	13.6	17.3	390	2.5	10.8	–
2008-06-16	15.7	13.7	600	2.1	6.6	340
2008-07-01	17.8	15.9	520	2.2	10.7	–
2008-07-02	16.8	11.8	540	2.8	6.0	370
2008-07-05	18.0	16.6	–	3.1	10.7	–
2008-07-08	17.8	15.0	470	2.9	11.1	–
2008-07-15	19.1	14.3	–	3.3	9.4	–
2008-07-23	20.1	12.4	520	3.0	7.7	360
2008-07-24	19.3	11.8	490	2.9	7.8	370
2008-07-25	19.7	11.7	480	2.9	7.3	330
2008-08-05	17.6	15.6	–	2.2	9.8	–
2008-09-17	10.5	10.6	400	0.8	7.3	260
2008-10-02	8.6	15.7	–	0.7	8.2	–
2008-10-14	8.8	10.4	390	0.4	6.0	280
2009-01-07	5.0	9.5	340	0.2	7.0	220
2009-01-20	4.8	9.9	360	0.2	8.0	330

Table 13: Hα and Hβ measurements. Fluxes are in units of 10^{-14} erg s^{-1} cm^{-2}, FWHM are in Å, and corresponding velocities are in km/s. For the first epoch, it is only possible to obtain the flux from the Hβ line by integrating the counts over the continuum at the position of the line centre. Other FWHM velocities are missing due to the line being unresolved.

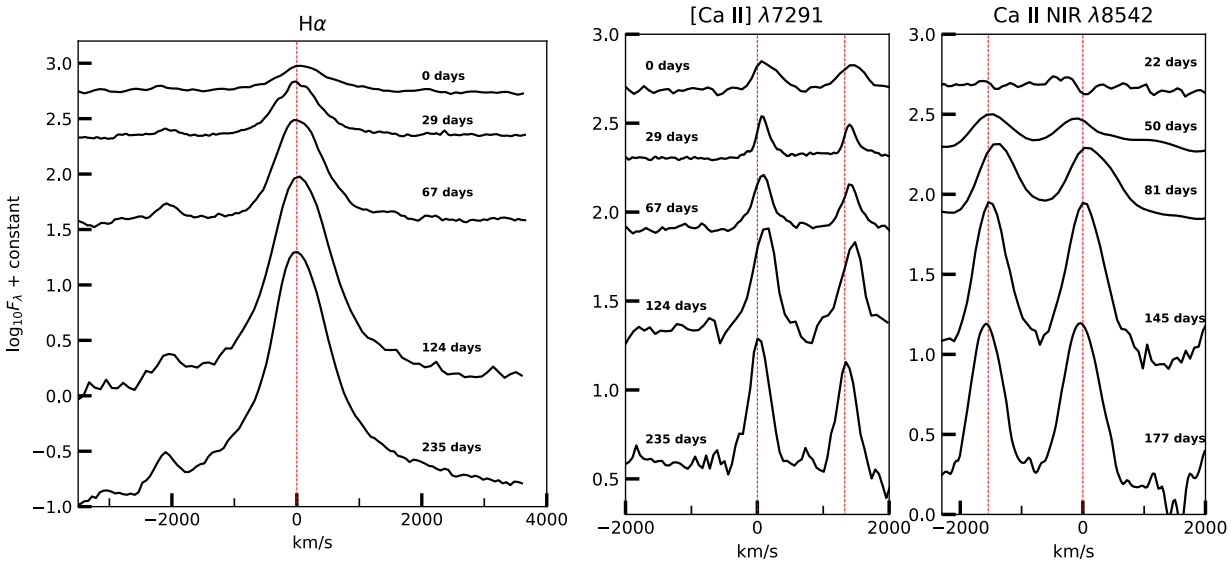

Figure 44: Left panel: evolution of the Hα line in the velocity space. The rest wavelength position is marked with a red dashed line. Right panels: evolution of [Ca II] λ7291 and Ca II λ8542. In the same panels it is possible to see also [Ca II] λ7323 and Ca II λ8498.

subsequent decline is faster than the Hα decline, although we lack a spectral coverage of the triplet at very late phases.

- The **[Ca II] doublet** is the only feature among the ones considered so far that is consistently redshifted by $\sim$ 80 km s^{-1} (Figure [44]). This could be interpreted as a sign of inflowing gas. The FWHM velocity for both lines, as measured from the VLT+UVES spectrum, is 100 and 110 km s^{-1} respectively, lower than the FWHM velocities mentioned so far. The luminosity evolution of these lines is clearly separated from the ones presented so far: the [Ca II] luminosity does not display a rebrightening, but decline monotonically from 1.8x10^{37} to 4x10^{35} erg s^{-1}.

The moderate velocities (> 400 km s^{-1}) and the delayed luminosity peak are characteristics shared by the Hα, Hβ and Ca II NIR triplet: this suggests that these lines form in the same environment, likely in the shocked interface bewteen ejecta and unshocked CSM. Conversely, the low velocity and monotonic evolution of the [Ca II] doublet separates it from the other lines: this forbidden feature is probably formed in the slowly expanding CSM, where the density of the gas is sufficiently low to avoid the collisional de-excitation that would suppress this emission. We notice that, at late phases, two broad emission feature arise around 7010 Å and 6170Å. The inferred v_{FWHM} is of the order of 3000 km s^{-1}. Since we are not able

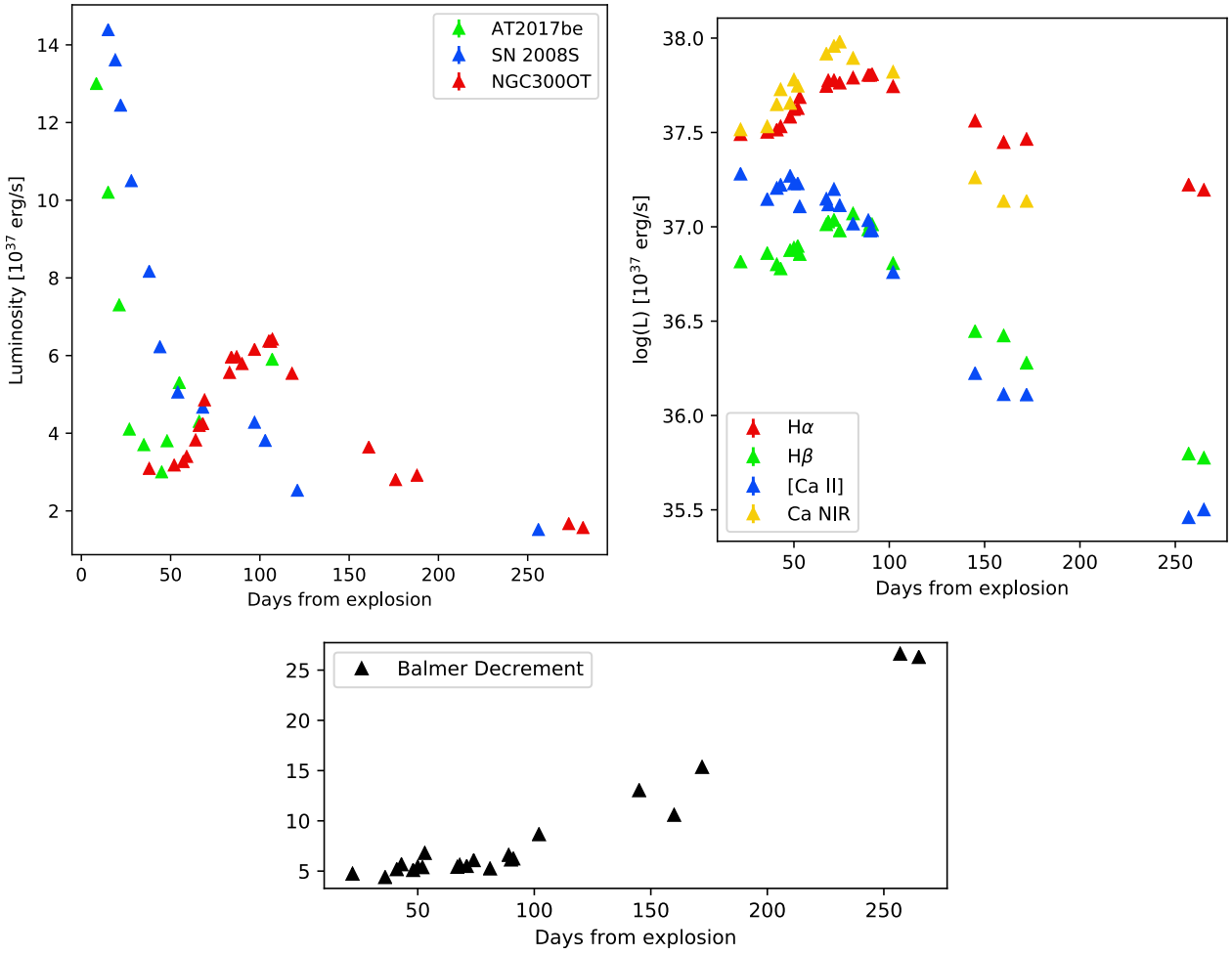

Figure 45: Left panel: Hα luminosity evolution of NGC300OT, AT 2017be and SN 2008S. The reference epoch is the explosion date. Right panel: evolution of Hα, Hβ, [Ca II] and Ca NIR triplet luminosity. For the [Ca II] doublet and Ca II triplet we integrated the contribution from all the lines belonging to the multiplet. Lower panel: evolution of the Balmer decrement.

	ph (days)	$^{56}Ni_{87A}$	$^{56}Ni_{Hamuy}$
NGC300OT OAPD	200-620	**2.9 ± 0.7**	**8.9 ± 3.4**
NGC300OT Humphreys	140-620	**4.6 ± 1**	**6.2 ± 2**
SN 2008S	145-310	14 ± 3	11 ± 2

Table 14: ^{56}Ni mass (x10^{-4} $M_{\odot}$) ejected by NGC300OT calculated adopting MJD 54564 ± 5 as best estimate for the explosion epoch. The results for SN 2008S are reported for comparison

to identify a transition responsible for this emission, we tentatively try to explain such feature as a blend of metallic lines.

6.3 Constraining the Explosion Epoch

Given the similarity between the Hα luminosity evolution of NGC300OT and AT 2017be (Figure [45]), we try to constrain with more precision the explosion epoch of NGC300OT, exploiting the best constrained explosion epoch of AT 2017be. Therefore, we shift in time the observations of NGC300OT until the first minimum of the Hα luminosity of NGC300OT overlaps the first minimum of AT 2017be. With this method we infer that the explosion of NGC300OT likely took place 16 (± 5) days before discovery (MJD 54564 ± 5). In light of this better estimate for the explosion epoch, we fine tune the ^{56}Ni mass ejected by NGC300OT, as detailed in Section [5.1] (Table [14]).

6.4 High-Resolution Spectrum

The VLT+UVES spectrum taken on 2008 July 02 already has already proven to be extremely useful in identifying and accurately estimating the FWHM velocities of several emission lines (Table [12]). Some of these lines, observed at high-resolution, show complex profiles: both Hα and Hβ show absorption features close to the line centre (Figure [46]). We determine the position of these absorption features with respect to the Na ID interstellar absorption. We find these components redshifted by +15 km s^{-1}. The Hα absorption component has a width of 30 km s^{-1}, while the Hβ component has a width of 50 km s^{-1}. The Hα line displays an additional absorption feature, with width close to spectral resolution, blueshifted by -140 km s^{-1}. These observed features suggest the presence of com-

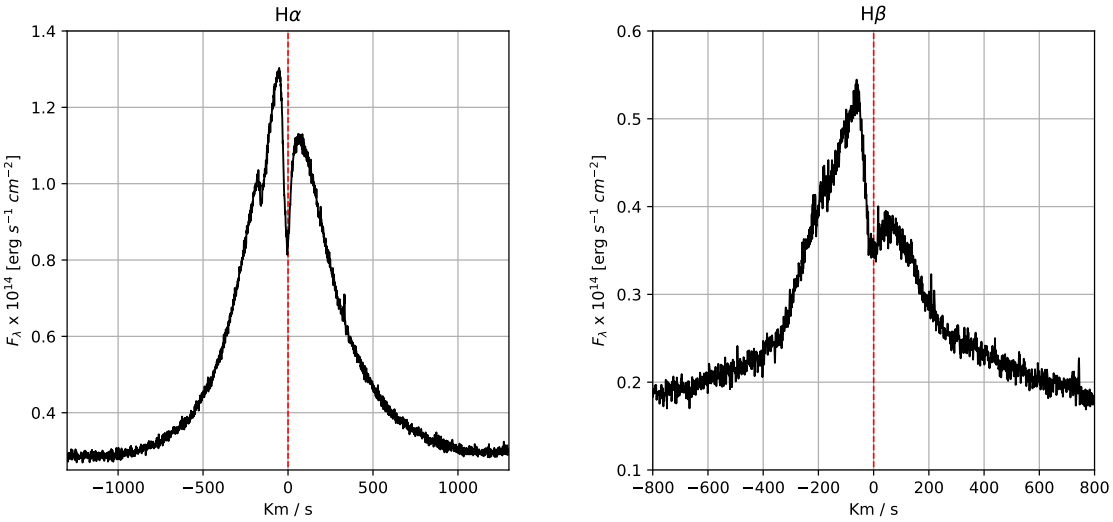

Figure 46: Left panel: Hα high-resolution profile in the velocity space from the spectrum taken on 2008 July 02. The rest wavelength position is marked with a red dashed line. Right panel: Hβ high-resolution profile at the same epoch.

plex CSM environment, possibly with inflowing and outflowing hydrogen winds. The [Ca II] forbidden doublet at high-resolution show a prominent red wing, extending up to +200 km s^{-1}, and a completely depleted blue wing, blueshifted by only -40 km s^{-1} (Figure [47], upper panels). This feature is not compatible with a P-Cygni profile, since there is no sign of absorption at the blue side of the emission line. Humphreys et al. 2011 explain the shape of this profile through electron scattering with optical depth $\sim$ 1. Other spectral features like Fe II λ6516 or He I λ5876 show a more symmetric profile, with widths of 220 and 260 km s^{-1}, respectively (Figure [47], lower panels). The narrow, unresolved Na ID components are of interstellar origin, as proved by the fact that they remain unresolved and maintain the same profile over time (Berger et al. (2009)). These unresolved Na ID lines are superimposed to broader absorption features with FWHM velocity of about 75 km s^{-1} due to expanding gas of the transient.

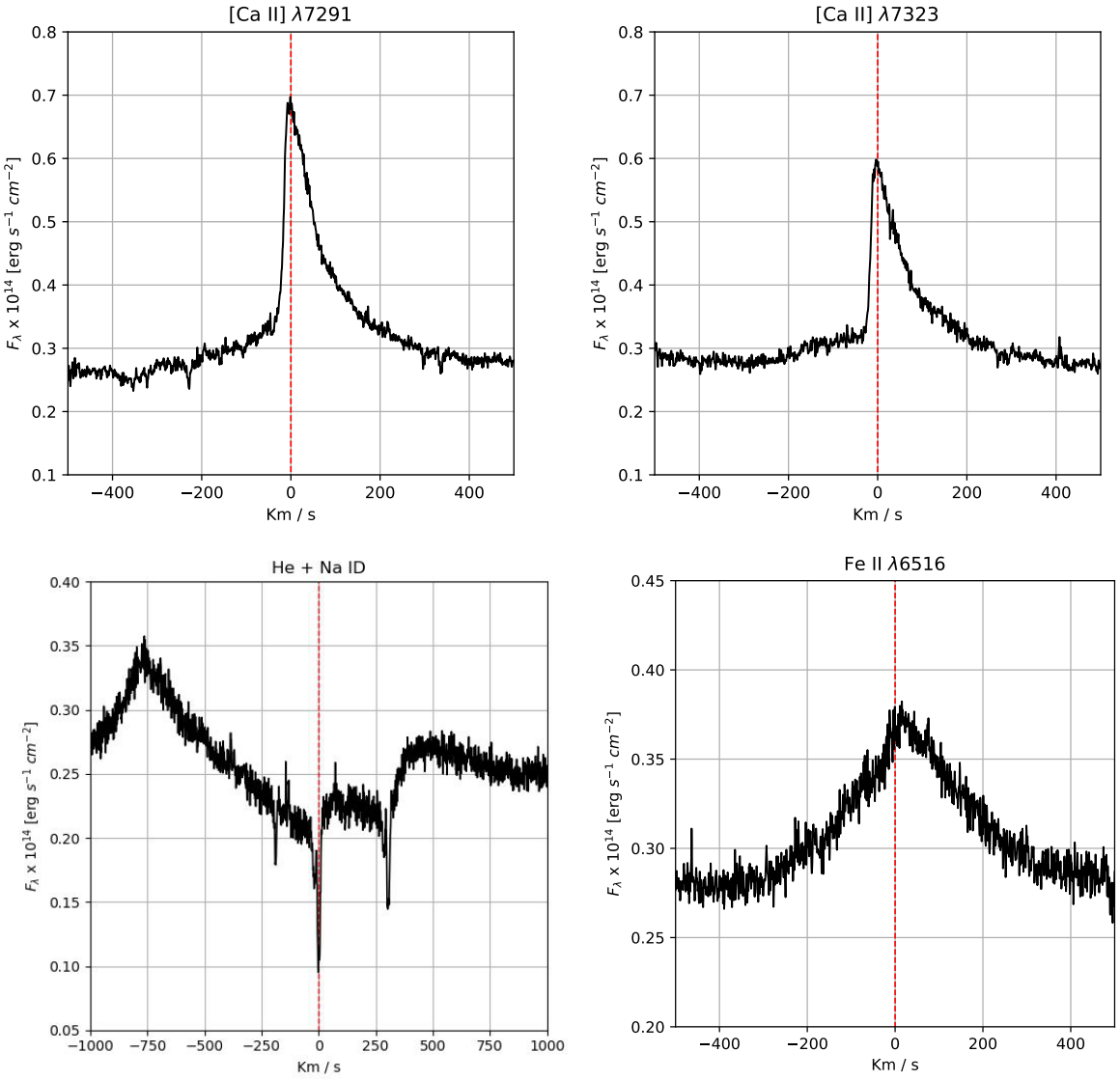

Figure 47: Forbidden [Ca II] doublet, Na ID absorption feature and the most prominent Fe II line (multiplet 40) shown in the velocity space. On the lower left panel, along with Na ID lines, it is possible to see the He I λ5876 line. The rest wavelength position is marked with a red dashed line

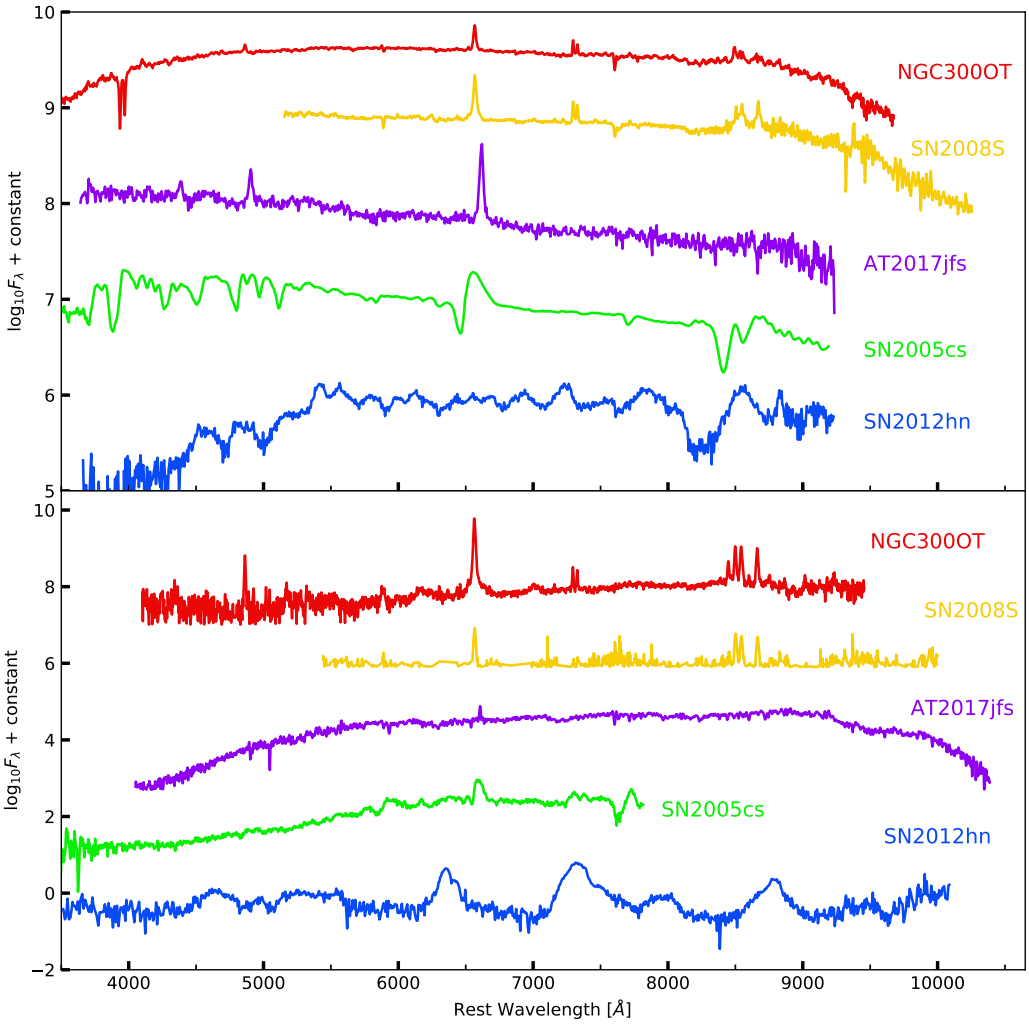

Figure 48: Comparison between the spectra of NGC300OT, SN 2008S, AT 2017jfs, SN 2012hn and SN 2005cs. Upper panel: spectra taken close to peak luminosity ($\sim$ 10 days after maximum). Lower panel: late spectra, taken $\sim$ 160 days after peak luminosity. For AT 2017jfs we refer to the first peak, while for SN 2005cs we refer to the start of the plateau.

6.5 Comparison with Other Transients

In Figure [48] we compare two spectra of NGC300OT, taken during the photospheric phase (14 days after peak) and during the nebular phase (150 days after peak), with spectra of other transients and supernovae at similar epochs. Both at early and late phases, the analogy with SN 2008S is clear: Hα and Ca II features are clearly recognizable at all epochs. The LRN AT 2017jfs displays similar narrow Balmer lines, while at late phases the hydrogen lines are less prominent. Ca II NIR triplet is detected at early phases, but there is no sign of the [Ca II] doublet. The faint type IIP SN 2005cs is clearly different due to the broad lines and prominent P-Cygni profiles. Finally, in the spectra of the calcium rich type I SN 2012hn, along with the lack of H lines, we note the calcium features to be significantly broader than the Ca lines present in ILRT spectra.

7 Conclusions and future perspectives

We reduced and discussed unpublished photometric and spectroscopic data of the ILRT NGC300OT. While a few papers are available in the literature with extensive data sets and discussing the nature of NGC300OT, we present optical and NIR observations extended until very late phases, high cadence spectroscopic sampling as well as two NIR spectra, a domain not covered with spectroscopic observations so far. In light of the study performed by Adams et al. (2016), we noticed the increase in probability of a terminal event rather than an LBV-like outburst. Hence we, estimated the ^{56}Ni mass ejected by the explosion, obtaining an upper limit that ranges from $\sim$ 2.5 to 8 x10^{-4} $M_{\odot}$ (depending on the method and data set used). We also compared the properties of NGC300OT with those of other ILRT, in particular SN 2008S and AT 2017be. We found that NGC300OT and AT 2017be, characterized by a pseudo-plateau in their light curves, displayed a delayed peak in Hα luminosity, which is not observed in SN 2008S. If this is indicative of the existence of two subclasses of ILRTs, similarly to what is observed for SN IIP and IIL, has to be investigated.

Despite the extensive analysis performed for this object, much work needs be done to understand the ILRT class. First of all, continuous monitoring of the progenitor sites of NGC300OT and SN 2008S will unequivocally disclose whether the events were actual explosions or non-terminal eruptions. Furthermore, a statistical study of the properties of ILRTs (ejected ^{56}Ni mass, rise time, spectral features) will be used to compare ILRTs characteristics with expected EC-SN properties (Cai et al, in preparation). In addition, a systematic study of the galaxies hosting these transients has not been performed yet: since the progenitor stars are not always identified, this can be an useful tool to constrain the formation channels of these events.
Explosion rates are still to be estimated, given the poor and incomplete sample of objects available, but forthcoming wide-field surveys like LSST (Stubbs, Heitmann 2019) and WFIRST (Spergel et al. 2015) will provide a greater number of ILRTs detections than ever before. WFIRST will prove particularly useful for the study of ILRTs, since it will be able to detect the IR-luminous progenitor stars of these transients, which are not observable in the optical domain, due to substantial absorption of the surrounding dust. A detailed analysis of the variability of the progenitor star may provide crucial information on its age and evolutive phase.
The abundance of discoveries granted by LSST and WFIRST will be supported by follow-up campaigns like the one organized for AT 2019abn (Jencson et al. 2019), which will sample the evolution of the transient, in particular the early rise, with unprecedented cadence. Finally, although X-rays counterparts were not observed for these objects (Berger et al. 2009), late time studies on the infrared and radio

domains are essential to investigate the evolution of the dust years after the event, as well as the geometry and stratification of the CSM.
Such detailed characterization of these transients will enable us to understand the nature of the elusive ILRTs, either confirming or posing new challenges to our current understanding of stellar evolution.

References

Adams S. M., Kochanek C. S., Prieto J. L., Dai X., Shappee B. J., Stanek K. Z. Almost gone: SN 2008S and NGC 300 2008OT-1 are fainter than their progenitors // Monthly Notices of the Royal Astronomical Society. Aug 2016. 460, 2. 1645–1657.

Arbour R., Boles T. Supernova 2008S in NGC 6946 // Central Bureau Electronic Telegrams. Feb 2008. 1234. 1.

Berger E., Soderberg A. M., Chevalier R. A., Fransson C., Foley R. J., Leonard D. C., Debes J. H., Diamond-Stanic A. M., Dupree A. K., Ivans I. I. An Intermediate Luminosity Transient in NGC 300: The Eruption of a Dust-Enshrouded Massive Star // The Astrophysical Journal. Jul 2009. 699, 2. 1850–1865.

Bond Howard E., Bedin Luigi R., Bonanos Alceste Z., Humphreys Roberta M., Monard L. A. G. Berto, Prieto José L., Walter Frederick M. The 2008 Luminous Optical Transient in the Nearby Galaxy NGC 300 // The Astrophysical Journal. Apr 2009. 695, 2. L154–L158.

Botticella M. T., Pastorello A., Smartt S. J., Meikle W. P. S., Benetti S., Kotak R., Cappellaro E., Crockett R. M., Mattila S., Sereno M., Patat F., Tsvetkov D., van Loon J. Th., Abraham D., Agnoletto I., Arbour R., Benn C., di Rico G., Elias-Rosa N., Gorshanov D. L., Harutyunyan A., Hunter D., Lorenzi V., Keenan F. P., Maguire K., Mendez J., Mobberley M., Navasardyan H., Ries C., Stanishev V., Taubenberger S., Trundle C., Turatto M., Volkov I. M. SN 2008S: an electron-capture SN from a super-AGB progenitor? // Monthly Notices of the Royal Astronomical Society. Sep 2009. 398, 3. 1041–1068.

Botticella Maria Teresa, Kotak Rubina, Meikle Peter, Smartt Stephen, Pastorello Andrea, Benetti Stefano. Follow-up observations of SN 2010dn. Jun 2010. 550.

Branch D., Wheeler J. C. Supernova Explosions. 2017a. 1. 17.

Branch D., Wheeler J. C. Supernova Explosions. 2017b. 1. 80–85.

Branch D., Wheeler J. C. Supernova Explosions. 2017c. 1. 319.

Branch D., Wheeler J. C. Supernova Explosions. 2017d. 1. 159–160.

Branch D., Wheeler J. C. Supernova Explosions. 2017e. 1. 185–190.

Branch David, Livio Mario, Yungelson L. R., Boffi Francesca R., Baron E. In Search of the Progenitors of Type IA Supernovae // Publications of the Astronomical Society of the Pacific. Nov 1995. 107. 1019.

Cai Y. Z., Pastorello A., Fraser M., Botticella M. T., Gall C., Arcavi I., Benetti S., Cappellaro E., Elias-Rosa N., Harmanen J., Hosseinzadeh G., Howell D. A., Isern J., Kangas T., Kankare E., Kuncarayakti H., Lundqvist P., Mattila S., McCully C., Reynolds T. M., Somero A., Stritzinger M. D., Terreran G. AT 2017be - a new member of the class of intermediate-luminosity red transients // Monthly Notices of the Royal Astronomical Society. Nov 2018. 480, 3. 3424–3445.

Cappellaro E. SNOoPy: a package for SN photometry // http://sngroup.oapd.inaf.it/snoopy.html. 2014.

Cardelli Jason A., Clayton Geoffrey C., Mathis John S. The Relationship between Infrared, Optical, and Ultraviolet Extinction // The Astrophysical Journal. Oct 1989. 345. 245.

Chiu H.Y. Neutrino emission processes, stellar evolution, and supernova. Part II // Annals of Physics. 1961. 16, 3. 321 – 345.

Dessart L. Wolf-Rayet stars as supernova progenitors // Wolf-Rayet Stars: Proceedings of an International Workshop held in Potsdam. Jan 2015. 245–250.

Dessart Luc, Hillier D. John, Gezari Suvi, Basa Stephane, Matheson Tom. SN 1994W: an interacting supernova or two interacting shells? // Monthly Notices of the Royal Astronomical Society. Mar 2009. 394, 1. 21–37.

Doherty Carolyn L., Gil-Pons Pilar, Siess Lionel, Lattanzio John C. Super-AGB Stars and their Role as Electron Capture Supernova Progenitors // Publications of the Astronomical Society of Australia. Nov 2017. 34. e056.

Drout Maria R., Soderberg Alicia M., Gal-Yam Avishay, Cenko S. Bradley, Fox Derek B., Leonard Douglas C., Sand David J., Moon Dae-Sik, Arcavi Iair, Green Yoav. The First Systematic Study of Type Ibc Supernova Multi-band Light Curves // Astrophysical Journal. Nov 2011. 741, 2. 97.

Filippenko A. V. Optical Spectra of Supernovae // Annual Review of Astronomy and Astrophysics. 1997. 35. 309–355.

Gieren Wolfgang, Pietrzyński Grzegorz, Soszyński Igor, Bresolin Fabio, Kudritzki Rolf-Peter, Minniti Dante, Storm Jesper. The Araucaria Project: Near-Infrared Photometry of Cepheid Variables in the Sculptor Galaxy NGC 300 // The Astrophysical Journal. Aug 2005. 628, 2. 695–703.

Gogarten Stephanie M., Dalcanton Julianne J., Murphy Jeremiah W., Williams Benjamin F., Gilbert Karoline, Dolphin Andrew. The NGC 300 Transient:

An Alternative Method for Measuring Progenitor Masses // The Astrophysical Journal. Sep 2009. 703, 1. 300–310.

Graham Matthew J., Kulkarni S. R., Bellm Eric C., Adams Scott M., Barbarino Cristina, Blagorodnova Nadejda, Bodewits Dennis, Bolin Bryce, Brady Patrick R., Cenko S. Bradley, Chang Chan-Kao, Coughlin Michael W., De Kishalay, Eadie Gwendolyn, Farnham Tony L., Feindt Ulrich, Franckowiak Anna, Fremling Christoffer, Gezari Suvi, Ghosh Shaon, Goldstein Daniel A., Golkhou V. Zach, Goobar Ariel, Ho Anna Y. Q., Huppenkothen Daniela, Ivezić Željko, Jones R. Lynne, Juric Mario, Kaplan David L., Kasliwal Mansi M., Kelley Michael S. P., Kupfer Thomas, Lee Chien-De, Lin Hsing Wen, Lunnan Ragnhild, Mahabal Ashish A., Miller Adam A., Ngeow Chow-Choong, Nugent Peter, Ofek Eran O., Prince Thomas A., Rauch Ludwig, van Roestel Jan, Schulze Steve, Singer Leo P., Sollerman Jesper, Taddia Francesco, Yan Lin, Ye Quan-Zhi, Yu Po-Chieh, Barlow Tom, Bauer James, Beck Ron, Belicki Justin, Biswas Rahul, Brinnel Valery, Brooke Tim, Bue Brian, Bulla Mattia, Burruss Rick, Connolly Andrew, Cromer John, Cunningham Virginia, Dekany Richard, Delacroix Alex, Desai Vandana, Duev Dmitry A., Feeney Michael, Flynn David, Frederick Sara, Gal-Yam Avishay, Giomi Matteo, Groom Steven, Hacopians Eugean, Hale David, Helou George, Henning John, Hover David, Hillenbrand Lynne A., Howell Justin, Hung Tiara, Imel David, Ip Wing-Huen, Jackson Edward, Kaspi Shai, Kaye Stephen, Kowalski Marek, Kramer Emily, Kuhn Michael, Landry Walter, Laher Russ R., Mao Peter, Masci Frank J., Monkewitz Serge, Murphy Patrick, Nordin Jakob, Patterson Maria T., Penprase Bryan, Porter Michael, Rebbapragada Umaa, Reiley Dan, Riddle Reed, Rigault Mickael, Rodriguez Hector, Rusholme Ben, van Santen Jakob, Shupe David L., Smith Roger M., Soumagnac Maayane T., Stein Robert, Surace Jason, Szkody Paula, Terek Scott, Van Sistine Angela, van Velzen Sjoert, Vestrand W. Thomas, Walters Richard, Ward Charlotte, Zhang Chaoran, Zolkower Jeffry. The Zwicky Transient Facility: Science Objectives // Publications of the Astronomical Society of the Pacific. Jul 2019. 131, 1001. 078001.

Hamuy Mario. Observed and Physical Properties of Core-Collapse Supernovae // The Astrophysical Journal. Jan 2003. 582, 2. 905–914.

Humphreys R. M., Davidson K., Smith N. η Carinae's Second Eruption and the Light Curves of the η Carinae Variables // The Publications of the Astronomical Society of the Pacific. IX 1999. 111. 1124–1131.

Humphreys Roberta M., Bond Howard E., Bedin Luigi R., Bonanos Alceste Z., Davidson Kris, Berto Monard L. A. G., Prieto José L., Walter Frederick M. The

Photometric and Spectral Evolution of the 2008 Luminous Optical Transient in NGC 300 // The Astrophysical Journal. Dec 2011. 743, 2. 118.

Janka H. Th. Conditions for shock revival by neutrino heating in core-collapse supernovae // Astronomy and Astrophysics. Mar 2001. 368. 527–560.

Janka H. Th., Langanke K., Marek A., Martínez-Pinedo G., Müller B. Theory of core-collapse supernovae // Physics Reports. Apr 2007. 442, 1-6. 38–74.

Jencson Jacob E., Adams Scott M., Bond Howard E., van Dyk Schuyler D., Kasliwal Mansi M., Bally John, Blagorodnova Nadejda, De Kishalay, Fremling Christoffer, Yao Yuhan, Fruchter Andrew, Rubin David, Barbarino Cristina, Sollerman Jesper, Miller Adam A., Hicks Erin K. S., Malkan Matthew A., Andreoni Igor, Bellm Eric C., Buchheim Robert, Dekany Richard, Feeney Michael, Frederick Sara, Gal-Yam Avishay, Gehrz Robert D., Giomi Matteo, Graham Matthew J., Green Wayne, Hale David, Hankins Matthew J., Hanson Mark, Helou George, Ho Anna Y. Q., Hung T., Jurić Mario, Kendurkar Malhar R., Kulkarni S. R., Lau Ryan M., Masci Frank J., Neill James D., Quin Kevin, Riddle Reed L., Rusholme Ben, Sims Forrest, Smith Nathan, Smith Roger M., Soumagnac Maayane T., Tachibana Yutaro, Tinyanont Samaporn, Walters Richard, Watson Stanley, Williams Robert E. Discovery of an Intermediate-luminosity Red Transient in M51 and Its Likely Dust-obscured, Infrared-variable Progenitor // The Astrophysical Journal Letters. Aug 2019. 880, 2. L20.

Kaiser N., Burgett W., Chambers K., Denneau L., Heasley J., Jedicke R., Magnier E., Morgan J., Onaka P., Tonry J. The Pan-STARRS wide-field optical/NIR imaging survey // Ground-based and Airborne Telescopes III. 7733. VII 2010. 77330E.

Kasen D., Woosley S. E., Heger A. Pair Instability Supernovae: Light Curves, Spectra, and Shock Breakout // Astrophysical Journal. VI 2011. 734. 102.

Kasliwal M. M. Systematically Bridging the Gap Between Novae and Supernovae // Publications of the Astronomical Society of Australia. VII 2012. 29. 482–488.

Keller S. C., Schmidt B. P., Bessell M. S., Conroy P. G., Francis P., Granlund A., Kowald E., Oates A. P., Martin-Jones T., Preston T., Tisserand P., Vaccarella A., Waterson M. F. The SkyMapper Telescope and The Southern Sky Survey // Publications of the Astronomical Society of Australia. V 2007. 24. 1–12.

Kochanek C. S. Dusty Explosions from Dusty Progenitors: The Physics of SN 2008S and the 2008 NGC 300-OT // The Astrophysical Journal. Nov 2011. 741, 1. 37.

Kochanek C. S., Adams Scott M., Belczynski Krzysztof. Stellar mergers are common // Monthly Notices of the Royal Astronomical Society. Sep 2014. 443, 2. 1319–1328.

Law N. M., Kulkarni S., Ofek E., Quimby R., Kasliwal M., Palomar Transient Factory Collaboration . The Palomar Transient Factory (PTF): Overview // American Astronomical Society Meeting Abstracts #213. 41. I 2009. 418. (Bulletin of the American Astronomical Society).

Leibundgut Bruno. Type Ia Supernovae // The Astronomy and Astrophysics Review. Jan 2000. 10, 3. 179–209.

Leung Shing-Chi, Nomoto Ken'ichi, Suzuki Tomoharu. Electron Capture Supernovae of Super-AGB Stars: Dependence on Central Density and Flame Physics // arXiv e-prints. Jan 2019. arXiv:1901.11438.

Li W., Leaman J., Chornock R., Filippenko A. V., Poznanski D., Ganeshalingam M., Wang X., Modjaz M., Jha S., Foley R. J., Smith N. Nearby supernova rates from the Lick Observatory Supernova Search - II. The observed luminosity functions and fractions of supernovae in a complete sample // Monthly Notices of the Royal Astronomical Society. IV 2011a. 412. 1441–1472.

Li Weidong, Chornock Ryan, Leaman Jesse, Filippenko Alexei V., Poznanski Dovi, Wang Xiaofeng, Ganeshalingam Mohan, Mannucci Filippo. Nearby supernova rates from the Lick Observatory Supernova Search - III. The rate-size relation, and the rates as a function of galaxy Hubble type and colour // Monthly Notices of the Royal Astronomical Society. Apr 2011b. 412, 3. 1473–1507.

Maeda Keiichi, Terada Yukikatsu. Progenitors of type Ia supernovae // International Journal of Modern Physics D. Jul 2016. 25, 10. 1630024.

Mason E., Diaz M., Williams R. E., Preston G., Bensby T. The peculiar nova V1309 Scorpii/nova Scorpii 2008. A candidate twin of V838 Monocerotis // Astronomy and Astrophysics. Jun 2010. 516. A108.

Metzger B. D., Pejcha O. Shock-powered light curves of luminous red novae as signatures of pre-dynamical mass-loss in stellar mergers // Monthly Notices of the Royal Astronomical Society. XI 2017. 471. 3200–3211.

Miquel Ramon. Cosmology with type-Ia supernovae // Journal of Physics A Mathematical General. Jun 2007. 40, 25. 6743–6755.

Monard L. A. G. Luminous Transient in NGC 300 // International Astronomical Union Circular. May 2008. 8946. 1.

Moriya Takashi J., Maeda Keiichi, Taddia Francesco, Sollerman Jesper, Blinnikov Sergei I., Sorokina Elena I. Mass-loss histories of Type IIn supernova progenitors within decades before their explosion // Monthly Notices of the Royal Astronomical Society. Apr 2014. 439, 3. 2917–2926.

Myra Eric S., Bludman Sidney A. Neutrino Transport and the Prompt Mechanism for Type II Supernovae // The Astrophysical Journal. May 1989. 340. 384.

Owocki S. P., Gayley K. G., Shaviv N. J. A Porosity-Length Formalism for Photon-Tiring-limited Mass Loss from Stars above the Eddington Limit // The Astrophysical Journal. XI 2004. 616. 525–541.

Pastorello & Fraser . Supernova impostors and other gap transients // Nature Astronomy. August 2019. 3.

Pastorello A., Botticella M. T., Trundle C., Taubenberger S., Mattila S., Kankare E., Elias-Rosa N., Benetti S., Duszanowicz G., Hermansson L., Beckman J. E., Bufano F., Fraser M., Harutyunyan A., Navasardyan H., Smartt S. J., van Dyk S. D., Vink J. S., Wagner R. M. Multiple major outbursts from a restless luminous blue variable in NGC 3432 // Monthly Notices of the Royal Astronomical Society. Oct 2010a. 408, 1. 181–198.

Pastorello A., Botticella M. T., Trundle C., Taubenberger S., Mattila S., Kankare E., Elias-Rosa N., Benetti S., Duszanowicz G., Hermansson L., Beckman J. E., Bufano F., Fraser M., Harutyunyan A., Navasardyan H., Smartt S. J., van Dyk S. D., Vink J. S., Wagner R. M. Multiple major outbursts from a restless luminous blue variable in NGC 3432 // Monthly Notices of the Royal Astronomical Society. Oct 2010b. 408, 1. 181–198.

Pastorello A., Chen T. W., Cai Y. Z., Morales-Garoffolo A., Cano Z., Mason E., Barsukova E. A., Benetti S., Berton M., Bose S., Bufano F., Callis E., Cannizzaro G., Cartier R., Chen Ping, Dong Subo, Dyrbye S., Elias-Rosa N., Flörs A., Fraser M., Geier S., Goranskij V. P., Kann D. A., Kuncarayakti H., Onori F., Reguitti A., Reynolds T., Losada I. R., Sagués Carracedo A., Schweyer T., Smartt S. J., Tatarnikov A. M., Valeev A. F., Vogl C., Wevers T., de Ugarte Postigo A., Izzo L., Inserra C., Kankare E., Maguire K., Smith K. W., Stalder B., Tartaglia L., Thöne C. C., Valerin G., Young D. R. The evolution of luminous red nova AT 2017jfs in NGC 4470 // Astronomy and Astrophysics. May 2019. 625. L8.

Pastorello A., Della Valle M., Smartt S. J., Zampieri L., Benetti S., Cappellaro E., Mazzali P. A., Patat F., Spiro S., Turatto M., Valenti S. A very faint core-collapse supernova in M85 // Nature. Oct 2007a. 449, 7164. 1–2.

Pastorello A., Smartt S. J., Mattila S., Eldridge J. J., Young D., Itagaki K., Yamaoka H., Navasardyan H., Valenti S., Patat F., Agnoletto I., Augusteijn T., Benetti S., Cappellaro E., Boles T., Bonnet-Bidaud J. M., Botticella M. T., Bufano F., Cao C., Deng J., Dennefeld M., Elias-Rosa N., Harutyunyan A., Keenan F. P., Iijima T., Lorenzi V., Mazzali P. A., Meng X., Nakano S., Nielsen T. B., Smoker J. V., Stanishev V., Turatto M., Xu D., Zampieri L. A giant outburst two years before the core-collapse of a massive star // Nature. Jun 2007b. 447, 7146. 829–832.

Pastorello A., Valenti S., Zampieri L., Navasardyan H., Taubenberger S., Smartt S. J., Arkharov A. A., Bärnbantner O., Barwig H., Benetti S., Birtwhistle P., Botticella M. T., Cappellaro E., Del Principe M., di Mille F., di Rico G., Dolci M., Elias-Rosa N., Efimova N. V., Fiedler M., Harutyunyan A., Höflich P. A., Kloehr W., Larionov V. M., Lorenzi V., Maund J. R., Napoleone N., Ragni M., Richmond M., Ries C., Spiro S., Temporin S., Turatto M., Wheeler J. C. SN 2005cs in M51 - II. Complete evolution in the optical and the near-infrared // Monthly Notices of the Royal Astronomical Society. Apr 2009. 394, 4. 2266–2282.

Pastorello A., Zampieri L., Turatto M., Cappellaro E., Meikle W. P. S., Benetti S., Branch D., Baron E., Patat F., Armstrong M., Altavilla G., Salvo M., Riello M. Low-luminosity Type II supernovae: spectroscopic and photometric evolution // Monthly Notices of the Royal Astronomical Society. Jan 2004. 347, 1. 74–94.

Patat F., Maund J. R., Benetti S., Botticella M. T., Cappellaro E., Harutyunyan A., Turatto M. VLT spectropolarimetry of the optical transient in NGC 300. Evidence of asymmetry in the circumstellar dust // Astronomy and Astrophysics. Feb 2010. 510. A108.

Perets H. B., Gal-Yam A., Mazzali P. A., Arnett D., Kagan D., Filippenko A. V., Li W., Arcavi I., Cenko S. B., Fox D. B., Leonard D. C., Moon D. S., Sand D. J., Soderberg A. M., Anderson J. P., James P. A., Foley R. J., Ganeshalingam M., Ofek E. O., Bildsten L., Nelemans G., Shen K. J., Weinberg N. N., Metzger B. D., Piro A. L., Quataert E., Kiewe M., Poznanski D. A faint type of supernova from a white dwarf with a helium-rich companion // Nature. May 2010. 465, 7296. 322–325.

Phillips M. M. The Absolute Magnitues of Type IA Supernovae // The Astrophysical Journal. Aug 1993. 413. L105.

Poelarends A. J. T., Herwig F., Langer N., Heger A. The Supernova Channel of Super-AGB Stars // The Astrophysical Journal. III 2008. 675. 614–625.

Prieto J. L. Bright Infrared Progenitor of Luminous Transient in NGC300 implies Explosion of a Massive Star // The Astronomer's Telegram. V 2008. 1550.

Prieto Jose L., Kistler Matthew D., Thompson Todd A., Yüksel Hasan, Kochanek Christopher S., Stanek Krzysztof Z., Beacom John F., Martini Paul, Pasquali Anna, Bechtold Jill. Discovery of the Dust-Enshrouded Progenitor of SN 2008S with Spitzer // The Astrophysical Journal. jun 2008. 681, 1. L9–L12.

Prieto José L., Sellgren Kris, Thompson Todd A., Kochanek Christopher S. A Spitzer/IRS Spectrum of the 2008 Luminous Transient in NGC 300: Connection to Proto-Planetary Nebulae // The Astrophysical Journal. Nov 2009. 705, 2. 1425–1432.

Pumo M. L. SN2008S and SN2008ha: is there a role for the super-asymptotic giant branch stars? // Memorie della Societa Astronomica Italiana Supplementi. Jan 2010. 14. 115.

Pumo M. L., Turatto M., Botticella M. T., Pastorello A., Valenti S., Zampieri L., Benetti S., Cappellaro E., Patat F. EC-SNe from Super-Asymptotic Giant Branch Progenitors: Theoretical Models Versus Observations // The Astrophysical Journal, Letters. Nov 2009. 705, 2. L138–L142.

Rau A., Kulkarni S. R., Law N. M., Bloom J. S., Ciardi D., Djorgovski G. S., Fox D. B., Gal-Yam A., Grillmair C. C., Kasliwal M. M., Nugent P. E., Ofek E. O., Quimby R. M., Reach W. T., Shara M., Bildsten L., Cenko S. B., Drake A. J., Filippenko A. V., Helfand D. J., Helou G., Howell D. A., Poznanski D., Sullivan M. Exploring the Optical Transient Sky with the Palomar Transient Factory // Publications of the Astronomical Society of the Pacific. XII 2009. 121. 1334.

Ritossa C., García-Berro E., Iben I. Jr. On the evolution of super AGB stars with ONe degenerate cores: the case of a 10 M_{sun} model // Memorie della Società Astronomia Italiana. 1996. 67. 675.

Rivera Sandoval L. E., Maccarone T. J., Corsi A., Brown P. J., Pooley D., Wheeler J. C. X-ray Swift observations of SN 2018cow // Monthly Notices of the Royal Astronomical Society. X 2018. 480. L146–L150.

Sahu D. K., Anupama G. C., Srividya S., Muneer S. Photometric and spectroscopic evolution of the Type IIP supernova SN 2004et // Monthly Notices of the Royal Astronomical Society. Nov 2006. 372, 3. 1315–1324.

Schlafly & Finkbeiner Douglas P. Measuring Reddening with Sloan Digital Sky Survey Stellar Spectra and Recalibrating SFD // The Astrophysical Journal. Aug 2011. 737, 2. 103.

Schlegel E. M. A new subclass of Type II supernovae? // Monthly Notices of the Royal Astronomical Society. V 1990. 244. 269–271.

Shappee Benjamin, Prieto J., Stanek K. Z., Kochanek C. S., Holoien T., Jencson J., Basu U., Beacom J. F., Szczygiel D., Pojmanski G., Brimacombe J., Dubberley M., Elphick M., Foale S., Hawkins E., Mullins D., Rosing W., Ross R., Walker Z. All Sky Automated Survey for SuperNovae (ASAS-SN or "Assassin") // American Astronomical Society Meeting Abstracts 223. 223. Jan 2014. 236.03. (American Astronomical Society Meeting Abstracts).

Siess L. Evolution of massive AGB stars. II. model properties at non-solar metallicity and the fate of Super-AGB stars // Astronomy and Astrophysics. Dec 2007. 476, 2. 893–909.

Smartt S. J. Progenitors of Core-Collapse Supernovae // Annual Review of Astronomy and Astrophysics. IX 2009. 47. 63–106.

Smartt S. J., Valenti S., Fraser M., Inserra C., Young D. R., Sullivan M., Pastorello A., Benetti S., Gal-Yam A., Knapic C., Molinaro M., Smareglia R., Smith K. W., Taubenberger S., Yaron O., Anderson J. P., Ashall C., Balland C., Baltay C., Barbarino C., Bauer F. E., Baumont S., Bersier D., Blagorodnova N., Bongard S., Botticella M. T., Bufano F., Bulla M., Cappellaro E., Campbell H., Cellier-Holzem F., Chen T.-W., Childress M. J., Clocchiatti A., Contreras C., Dall'Ora M., Danziger J., de Jaeger T., De Cia A., Della Valle M., Dennefeld M., Elias-Rosa N., Elman N., Feindt U., Fleury M., Gall E., Gonzalez-Gaitan S., Galbany L., Morales Garoffolo A., Greggio L., Guillou L. L., Hachinger S., Hadjiyska E., Hage P. E., Hillebrandt W., Hodgkin S., Hsiao E. Y., James P. A., Jerkstrand A., Kangas T., Kankare E., Kotak R., Kromer M., Kuncarayakti H., Leloudas G., Lundqvist P., Lyman J. D., Hook I. M., Maguire K., Manulis I., Margheim S. J., Mattila S., Maund J. R., Mazzali P. A., McCrum M., McKinnon R., Moreno-Raya M. E., Nicholl M., Nugent P., Pain R., Pignata G., Phillips M. M., Polshaw J., Pumo M. L., Rabinowitz D., Reilly E., Romero-Cañizales C., Scalzo R., Schmidt B., Schulze S., Sim S., Sollerman J., Taddia F., Tartaglia L., Terreran G., Tomasella L., Turatto M., Walker E., Walton N. A., Wyrzykowski L., Yuan F., Zampieri L. PESSTO: survey description and products from the first data release by the Public ESO Spectroscopic Survey of Transient Objects // Astronomy and Astrophysics. VII 2015. 579. A40.

Smith N., Ganeshalingam M., Chornock R., Filippenko A. V., Li W., Silverman J. M., Steele T. N., Griffith C. V., Joubert N., Lee N. Y., Lowe T. B., Mobberley M. P., Winslow D. M. SN 2008S: A Cool Super-Eddington Wind in a Supernova Impostor // The Astrophysical Journal. V 2009. 697. L49–L53.

Spergel D., Gehrels N., Baltay C., Bennett D., Breckinridge J., Donahue M., Dressler A., Gaudi B. S., Greene T., Guyon O., Hirata C., Kalirai J., Kasdin N. J., Macintosh B., Moos W., Perlmutter S., Postman M., Rauscher B., Rhodes J., Wang Y., Weinberg D., Benford D., Hudson M., Jeong W. S., Mellier Y., Traub W., Yamada T., Capak P., Colbert J., Masters D., Penny M., Savransky D., Stern D., Zimmerman N., Barry R., Bartusek L., Carpenter K., Cheng E., Content D., Dekens F., Demers R., Grady K., Jackson C., Kuan G., Kruk J., Melton M., Nemati B., Parvin B., Poberezhskiy I., Peddie C., Ruffa J., Wallace J. K., Whipple A., Wollack E., Zhao F. Wide-Field InfrarRed Survey Telescope-Astrophysics Focused Telescope Assets WFIRST-AFTA 2015 Report // arXiv e-prints. Mar 2015. arXiv:1503.03757.

Stubbs Christopher W., Heitmann Katrin. Report on LSST Next-generation Instrumentation Workshop, April 11, 12 2019 // arXiv e-prints. May 2019. arXiv:1905.04669.

Szalai Tamás, Zsíros Szanna, Fox Ori D., Pejcha Ondřej, Müller Tomás. A Comprehensive Analysis of Spitzer Supernovae // The Astrophysical Journal Supplement Series. Apr 2019. 241, 2. 38.

Takahashi Koh, Sumiyoshi Kohsuke, Yamada Shoichi, Umeda Hideyuki, Yoshida Takashi. The Evolution toward Electron Capture Supernovae: The Flame Propagation and the Pre-bounce Electron-Neutrino Radiation // The Astrophysical Journal. Feb 2019. 871, 2. 153.

Tartaglia L. Interacting supernovae and supernova impostors. 2015.

Taubenberger Stefan. The Extremes of Thermonuclear Supernovae // Handbook of Supernovae, ISBN 978-3-319-21845-8. Springer International Publishing AG, 2017, p. 317. 2017. 317.

Thompson Todd A., Prieto José L., Stanek K. Z., Kistler Matthew D., Beacom John F., Kochanek Christopher S. A New Class of Luminous Transients and a First Census of their Massive Stellar Progenitors // The Astrophysical Journal. Nov 2009. 705, 2. 1364–1384.

Tonry J. L., Denneau L., Heinze A. N., Stalder B., Smith K. W., Smartt S. J., Stubbs C. W., Weiland H. J., Rest A. ATLAS: A High-cadence All-sky Survey System // Publications of the Astronomical Society of the Pacific. Jun 2018. 130, 988. 064505.

Turatto M. Classification of Supernovae. 598. 2003. 21–36.

Tylenda R., Hajduk M., Kamiński T., Udalski A., Soszyński I., Szymański M. K., Kubiak M., Pietrzyński G., Poleski R., Wyrzykowski Ł., Ulaczyk K. V1309 Scorpii: merger of a contact binary // Astronomy and Astrophysics. IV 2011. 528. A114.

Valenti S., Pastorello A., Cappellaro E., Benetti S., Mazzali P. A., Manteca J., Taubenberger S., Elias-Rosa N., Ferrando R., Harutyunyan A., Hentunen V. P., Nissinen M., Pian E., Turatto M., Zampieri L., Smartt S. J. A low-energy core-collapse supernova without a hydrogen envelope // Nature. Jun 2009. 459, 7247. 674–677.

Valenti S., Yuan F., Taubenberger S., Maguire K., Pastorello A., Benetti S., Smartt S. J., Cappellaro E., Howell D. A., Bildsten L., Moore K., Stritzinger M., Anderson J. P., Benitez-Herrera S., Bufano F., Gonzalez-Gaitan S., McCrum M. G., Pignata G., Fraser M., Gal-Yam A., Le Guillou L., Inserra C., Reichart D. E., Scalzo R., Sullivan M., Yaron O., Young D. R. PESSTO monitoring of SN 2012hn: further heterogeneity among faint Type I supernovae // Monthly Notices of the Royal Astronomical Society. Jan 2014. 437, 2. 1519–1533.

Van Dyk S. D., Peng C. Y., King J. Y., Filippenko A. V., Treffers R. R., Li W., Richmond M. W. SN 1997bs in M66: Another Extragalactic η Carinae Analog? // The Publications of the Astronomical Society of the Pacific. XII 2000. 112. 1532–1541.

Wanajo S., Nomoto K., Janka H. T., Kitaura F. S., Müller B. Nucleosynthesis in Electron Capture Supernovae of Asymptotic Giant Branch Stars // The Astrophysical Journal. Apr 2009. 695, 1. 208–220.

Williams S. C., Darnley M. J., Bode M. F., Steele I. A. A Luminous Red Nova in M31 and its Progenitor System // The Astrophysical Journal Letters. Jun 2015. 805, 2. L18.

Yoon S. C., Woosley S. E., Langer N. Type Ib/c Supernovae in Binary Systems. I. Evolution and Properties of the Progenitor Stars // Astrophysical Journal. Dec 2010. 725, 1. 940–954.

Zha Shuai, Leung Shing-Chi, Suzuki Toshio, Nomoto Ken'ichi. Evolution of ONeMg Core in Super-AGB Stars towards Electron-Capture Supernovae: Effects of Updated Electron-Capture Rate // arXiv e-prints. Jul 2019. arXiv:1907.04184.

de Vaucouleurs Gerard, de Vaucouleurs Antoinette, Corwin Jr. Herold G., Buta Ronald J., Paturel Georges, Fouque Pascal. Third Reference Catalogue of Bright Galaxies. 1991.